University of Alberta

Understanding the Role of Surface Microgeometries on Wetting: Designing Robust Superhydrophobic Surfaces

by

Guoping Fang

A thesis submitted to the Faculty of Graduate Studies and Research
in partial fulfillment of the requirements for the degree of

Master of Science

Department of Mechanical Engineering

Spring 2014
Edmonton, Alberta

Abstract

This thesis is concerned with effects of surface microgeometries on wetting, aiming at providing instructions for reproducing controllable wettability on artificial surfaces and designing robust superhydrophobic surfaces.

First, the origin of edge effect is understood by a thermodynamic approach for the analysis of energetic state of drops on a single pillar. A wetting map in terms of edge angle and intrinsic contact angle is provided for designing microstructures to prevent drop collapse/spilling over the pillar. Secondly, wetting transitions on various microstructured surfaces (i.e., arrays of pillars) has been understood by a first-principle thermodynamic model. Effects of surface parameters, i.e., intrinsic CA, edge angle and length scale factor, on wetting stability has been revealed. Finally, an experimental study on the application of superhydrophobic surfaces in low-temperature conditions is carried out by using differential scanning calorimetry and a thermoelectric cooler. Effects of various factors responsible for drop freezing have been systematically investigated.

Acknowledgements

I am heartily thankful to Prof. Alidad Amirfazli, for his strong support and great effort in guidance during the development of this thesis. I am very grateful to Prof. Brian Fleck, for his kind availability in assisting me with my research life during my hard time. I also would like to extend my appreciations to the members of my Supervisory Committee: Prof. Tian Tang and Prof. Morris Flynn for their examination and advices in my research program.

Special thanks are given to my friends for their help and support during my research. They are Xiaohua Kong, Wen Li, Andrew J. B. Milne, Farshid Chini, Huanchen Chen, Mengcheng Shen, and Feng Yu.

Finally, I also gratefully acknowledge the financial support from Alberta Ingenuity Graduate Recruitment Scholarship in Nanotechnology (G. F.), Natural Sciences and Engineering Research Council of Canada (NSERC), and Canada Research Chair Program (A. A.).

Table of Contents

List of Tables

List of Figures

List of Symbols, Nomenclature and Abbreviations

FE	Free energy
FEB	Free energy barrier
CA	Contact angle
CAH	Contact angle hysteresis
θ_a	Advancing contact angle
θ_r	Receding contact angle
θ_Y	Intrinsic contact angle
θ_C	Cassie's contact angle
θ_W	Wenzel's contact angle
com	Composite state, i.e., the drop is suspended by the microstructures with the air pockets trapped under the drop
non	Noncomposite state, i.e., complete penetration of liquid into the troughs of surface microstructures with only solid-liquid interface under the drop
TPCL	Three phase contact line
SHS	Superhydrophobic surfaces

f_a	Cassie's area fraction of the liquid in contact with the solid
r	Surface roughness
a, b, h	Pillar width, pillar spacing and pillar height, respectively
γ^{la}, γ^{sa} and γ^{ls}	Free surface energy (surface tension) at liquid-air, solid-air and liquid-solid interfaces, respectively
θ_A, θ_B and θ_C	CA of drop at instantaneous positions A, B and C, respectively
L_A, L_B and L_C	Drop base radius at instantaneous positions A, B and C, respectively
H_A and H_B	Penetration heights for drops at the positions A and B, respectively

Chapter 1 - Introduction and Objectives

1.1 Introduction

Surface wetting behavior, which depends on surface chemistry and roughness, is usually described by contact angle (CA, the angle at which a liquid/vapor interface meets a solid surface) and CA hysteresis (CAH, the difference between advancing and receding CAs). Wetting behavior is also an area of intense interest for both academic research and industrial applications in the past decades.[1, 2] Partly due to the limitations of surface chemical modification, e.g., the choice of chemical species and their biochemical compatibility, the effect of surface roughness or microgeometries on wetting has received much attention.[3-7] In particular, researchers have noticed that nature has smartly taken advantage of the flexibility in manipulation of surface micro/nano-geometries to develop various special wetting properties. For example, superhydrophobic surfaces (with high CA and small CAH) are widely observed in some plants (e.g., lotus leaves[8]) and animals (e.g., butterfly wings[9]). Such surfaces imply potential engineering applications in self-cleaning, anti-icing, and drag-reduction fields. However, to date, artificial superhydrophobic surfaces are still hardly comparable with natural ones, due to the instability of superhydrophobicity. To reproduce robust superhydrophobicity on artificial surfaces, a comprehensive understanding of the role of surface microgeometries on wetting behaviors is important.

Relationships between CA and surface roughness (r) or solid-liquid contact area fraction (f_a) has been well established more than 60 years ago, i.e., the classical Wenzel's and Cassie's equations.[10, 11] However, these equations are inadequate to comprehend the role of surface microgeometries on wettability, since r or f_a represents a composite measure of all surface microgeometrical parameters. For example, the same r or f_a could be obtained for different rough surfaces. Also, for geometrical textures, the classical Wenzel's and Cassie's equations do not necessarily provide any information about CAH, as they only, strictly speaking, apply to equilibrium CA. Therefore, a complete understanding of the role of surface microgeometries on the wetting behavior (especially on superhydrophobic wetting behavior) still requires future investigations.

To understand the role of surface microgeometries on wetting, the study of edge effect for liquid drop on one single pillar would be preferred for a start. This is because when there are surface microgeometries, solid edges will necessarily exist (depending on the scale at which an edge is examined, it may appear as sharp or round). Also, edge is known to be the reason that the drop is hindered from further spreading and spilling over the sides of a pillar.[12-14] Though many studies have investigated the edge effect,[15-18] few of them have advanced the understanding beyond Gibbs'[19] inequality condition analysis for drop contact line at a solid edge. As a result, there is still a lack of framework to describe the mechanism responsible for the edge effect and instructions for designing microstructures preventing drop collapse/spilling over the sides of the pillar. This

is an important issue when studying wetting of textured surfaces made of micropillar for its texture.

Although the study of edge effect of single pillar on its wetting provides insights into fundamentals of wetting behaviors for textured surfaces, for a more applied/realistic understanding, investigation of drop wetting on arrays of single microstructure is needed. This is so to further understand the role of surface microgeometries on wetting. Particularly, factors responsible for drop wetting transition between composite (the drop is suspended by the microstructures with the air pockets trapped under the drop) and noncomposite (complete penetration of liquid into the troughs of surface microstructures with only solid-liquid interface under the drop) states is key to the design of robust superhydrophobic surfaces. Former studies[20-25] have addressed the importance of the transition energy barrier responsible for the wetting transition from composite to noncomposite states. Such transition energy barrier could allow drops to stay stably/metastably in superhydrophobic/superoleophobic states even for hydrophilic materials or low-surface-tension liquids,[26-29] which depends strongly on the configuration of the microstructures. However, to date, still there is not a first-principle thermodynamic model to investigate the factors affecting the wetting transition (from composite to noncomposite states) systematically. In addition, the theoretical discussion of wetting transition from noncomposite to composite states has been ignored in the past, though it has been observed experimentally.[30-35] The transition energy barrier from noncomposite to composite

states is expected to be important in the recovery of composite state when the drop is initially in noncomposite state (e.g., water condenses into the troughs of the microstructures), which needs a further investigation.

On the application side for superhydrophobic surfaces, they show a very promising use in low-temperature conditions such as resisting frost, ice, snow formation, and water drop freezing.[36-39] However, some observations bring into question the advantage of using superhydrophobic surfaces.[40, 41] Attempts to resolve such discrepancy of findings in the literature and understanding the anti-icing properties of superhydrophobic surfaces to date are usually done on a one factor at a time basis, while various factors are involved, e.g., surface chemistry, roughness and environmental condition. Therefore, it is still unclear what is the mechanism behind the phenomena and could be used to explain the contradictory results. Systematic investigation of the factors affecting the anti-icing properties of superhydrophobic surfaces is therefore needed.

1.2 Objectives

The aim of this research work is to carry out a comprehensive study on understanding the role of surface microgeometries on wetting, giving instructions for designing robust superhydrophobic surfaces and its application in the anti-icing field. Three main objectives are set:

The first objective is to develop a thermodynamic model to understand the wetting phenomena at an edge, and give a general guide (i.e., a wetting map) for

designing microstructures for preventing drop collapse/spilling over the sides of the pillar.

The second objective is to establish a robust 3-D thermodynamic model to understand the wetting transitions of drops on various microstructured surfaces, and provide a framework to design robust superhydrophobic surfaces.

The third objective is to evaluate the potential for application of superhydrophobic surfaces in low-temperature conditions. The roles of surface chemistry, roughness and environmental condition (i.e., frosting) on the performance of superhydrophobic surfaces in low-temperature applications are needed to be provided.

1.3 Organization of this Thesis

This thesis comprises of five chapters. Chapter 1 is the introduction and Chapter 2, 3 and 4 include three manuscripts based on papers published or submitted for publication; the last chapter is the conclusions and possible future works. There are also appendices, with Appendix A somewhat related work to the topic of this thesis; i.e., an experimental work on wetting behavior on patterned surfaces with different microgeometries. The idea of including of Appendix A is to capture the entire work accomplished during the course of this graduate studies, whether or not tightly linked with the main subject of this thesis.

Chapter 2 presents a thermodynamic approach for investigating the energetic state of drops on a single pillar, in order to understand the wetting phenomena at

the edge. A framework describing the mechanism for the edge effect and instructions for designing microstructures preventing drop collapse/spilling over the sides for the pillar are provided. The results have expanded the current understanding of Gibbs' inequality condition. This work has been published in the journal Langmuir (DOI: 10.1021/la301623h).

Chapter 3 describes a first-principle thermodynamic modeling for understanding the role of surface microgeometries on wetting of patterned surfaces with various microgeometries, i.e., arrays of pillars and arrays of two typical re-entrant microstructures (microstructures of convex and concave side wall). Transition energy barriers from composite to noncomposite states, as well as from noncomposite to composite states have been both studied. Various factors, i.e., intrinsic CA, edge angle and length scale factor, responsible for drop wetting transition are systematically investigated. This work is to be submitted for publication shortly.

Chapter 4 evaluates the potential of application of superhydrophobic surfaces in low-temperature conditions. Effects of various factors, i.e., surface chemistry, roughness and environmental condition (frosting), on drop freezing have been investigated systematically. The experimental and analytical study has resolved the discrepancy of findings in the literature and the mechanism responsible for the anti-icing properties of superhydrophobic surfaces is revealed. This work has been accepted by the journal Surface Innovations (DOI: 10.1680/si.13.00046).

Chapter 5 presents the conclusions drawn from this work. This is followed by suggestions and recommendations for possible future work.

1.4 Contributions of Authors

All papers are co-authored; however it is mutual understanding of the authors that Guoping Fang, as the first author, is the primary investigator of the research work. The contributions of other authors are limited to an advisory and editorial capacity and they are acknowledged.

References

(1) Herminghaus, S.; Brinkmann, M.; Seemann, R. *Ann. Rev. Mater. Res.* **2008,** *38*, 101-121.

(2) Bonn, D.; Eggers, J.; Indekeu, J.; Meunier, J.; Rolley, E. *Rev. Mod. Phys.* **2009,** *81*, 739-805.

(3) Zhao, Y.; Lu, Q.; Li, M.; Li, X. *Langmuir* **2007,** *23*, 6212-6217.

(4) Zhu, L.; Feng, Y.; Ye, X.; Zhou, Z. *Sens. Actuators, A* **2006,** *A130-A131*, 595-600.

(5) Shastry, A.; Case, M. J.; Boehringer, K. F. *Langmuir* **2006,** *22*, 6161-6167.

(6) Su, Y.; Ji, B.; Zhang, K.; Gao, H.; Huang, Y.; Hwang, K. *Langmuir* **2010,** *26*, 4984-4989.

(7) Cheng, Z.; Gao, J.; Jiang, L. *Langmuir* **2010,** *26*, 8233-8.

(8) Koch, K.; Bohn, H. F.; Barthlott, W. *Langmuir* **2009,** *25*, 14116-20.

(9) Zheng, Y.; Gao, X.; Jiang, L. *Soft Matter* **2007,** *3*, 178-182.

(10) Wenzel, R. N. *J. Ind. Eng. Chem.* **1936,** *28*, 988-994.

(11) Cassie, A. B. D.; Baxter, S. *Trans. Faraday Soc.* **1944,** *40*, 546-551.

(12) Oliver, J. F.; Huh, C.; Mason, S. G. *J. Colloid Interface Sci.* **1977,** *59*, 568-81.

(13) Extrand, C. W. *Langmuir* **2005,** *21*, 10370-10374.

(14) Tóth, T.; Ferraro, D.; Chiarello, E.; Pierno, M.; Mistura, G.; Bissacco, G.; Semprebon, C. *Langmuir* **2011,** *27*, 4742-4748.

(15) Zhang, J.; Gao, X.; Jiang, L. *Langmuir* **2007,** *23*, 3230-3235.

(16) Berthier, J.; Loe-Mie, F.; Tran, V. M.; Schoumacker, S.; Mittler, F.; Marchand, G.; Sarrut, N. *J. Colloid Interface Sci.* **2009,** *338*, 296-303.

(17) Kalinin, Y. V.; Berejnov, V.; Thorne, R. E. *Langmuir* **2009,** *25*, 5391-5397.

(18) Sheng, X.; Zhang, J.; Jiang, L. *Langmuir* **2009,** *25*, 9903-9907.

(19) Gibbs, J. W. *"Scientific Papers"* **1906**, 326.

(20) Patankar, N. A. *Langmuir* **2003,** *19*, 1249-1253.

(21) Patankar, N. A. *Langmuir* **2004,** *20*, 7097-7102.

(22) Marmur, A. *Langmuir* **2003,** *19*, 8343-8348.

(23) Marmur, A. *Langmuir* **2004,** *20*, 3517-3519.

(24) Whyman, G.; Bormashenko, E. *Langmuir* **2011,** *27*, 8171-6.

(25) Bormashenko, E.; Musin, A.; Whyman, G.; Zinigrad, M. *Langmuir* **2012,** *28*, 3460-3464.

(26) Tuteja, A.; Choi, W.; Ma, M.; Mabry, J. M.; Mazzella, S. A.; Rutledge, G. C.; McKinley, G. H.; Cohen, R. E. *Science* **2007,** *318*, 1618-1622.

(27) Ahuja, A.; Taylor, J. A.; Lifton, V.; Sidorenko, A. A.; Salamon, T. R.; Lobaton, E. J.; Kolodner, P.; Krupenkin, T. N. *Langmuir* **2008,** *24*, 9-14.

(28) Wang, J. D.; Liu, F. B.; Chen, H. S.; Chen, D. R. *Appl. Phys. Lett.* **2009,** *95*, 084104.

(29) Im, M.; Im, H.; Lee, J. H.; Yoon, J. B.; Choi, Y. K. *Soft Matter* **2010,** *6*, 1401-1404.

(30) Dorrer, C.; Ruhe, J. *Langmuir* **2007,** *23*, 3820-3824.

(31) Krupenkin, T. N.; Taylor, J. A.; Wang, E. N.; Kolodner, P.; Hodes, M.; Salamon, T. R. *Langmuir* **2007,** *23*, 9128-9133.

(32) Boreyko, J. B.; Chen, C. H. *Phys. Rev. Lett.* **2009,** *103*.

(33) Dorrer, C.; Ruehe, J. *Soft Matter* **2009,** *5*, 51-61.

(34) Koishi, T.; Yasuoka, K.; Fujikawa, S.; Ebisuzaki, T.; Zeng, X. C. *Proc. Natl. Acad. Sci. U. S. A.* **2009,** *106*, 8435-8440.

(35) Verho, T.; Korhonen, J. T.; Sainiemi, L.; Jokinen, V.; Bower, C.; Franze, K.; Franssila, S.; Andrew, P.; Ikkala, O.; Ras, R. H. A. *Proc. Natl. Acad. Sci. U. S. A.* **2012,** *109*, 10210-10213.

(36) Liu, Z.; Gou, Y.; Wang, J.; Cheng, S. *Int. J. Heat Mass Transfer* **2008,** *51*, 5975-5982.

(37) Tourkine, P.; Le Merrer, M.; Quere, D. *Langmuir* **2009,** *25*, 7214-7216.

(38) Mishchenko, L.; Hatton, B.; Bahadur, V.; Taylor, J. A.; Krupenkin, T.; Aizenberg, J. *ACS Nano* **2010,** *4*, 7699-7707.

(39) Cao, L.; Jones, A. K.; Sikka, V. K.; Wu, J.; Gao, D. *Langmuir* **2009,** *25*, 12444-12448.

(40) Jung, S.; Dorrestijn, M.; Raps, D.; Das, A.; Megaridis, C. M.; Poulikakos, D. *Langmuir* **2011,** *27*, 3059-3066.

(41) Wilson, P. W.; Lu, W.; Xu, H.; Kim, P.; Kreder, M. J.; Alvarenga, J.; Aizenberg, J. *Physical Chemistry Chemical Physics* **2013,** *15*, 581-585.

Chapter 2 - Understanding the Edge Effect in Wetting: A Thermodynamic Approach[1]

2.1 Introduction

A drop placed on top of a pedestal/pillar (e.g., cylindrical, upright frustum, or inverted frustum) away from edges will take its equilibrium contact angle. However, growing such a drop causes the contact line to arrive at the edge of a pillar. The edge is known to hinder the drop from further spreading and spilling over the sides of the pillar even if the apparent contact angle would exceed the advancing contact angle value.[1-3] Such an effect is called the edge effect in wetting (or pinning effect at the solid edge). It plays an important role in many wetting phenomena in practical applications: for example, the preference of attaching at edges for frothing bubbles in the mineral floatation and the propensity for water to resist overflowing at the edge of a container.[4, 5] As is known, solid edges will necessarily exist when there is surface roughness (depending on the scale at which an edge is examined, it may appear as sharp or round). Accordingly, the edge effect can play an important role in the wetting behavior on roughened surfaces with various microgeometries.

[1] This work has been published as Fang, G.; Amirfazli, A. *Langmuir* 2012, 28, 9421-9430.

Much effort has been devoted to the investigation of the effect of surface roughness or microgeometry on surface wettability. As an example, superhydrophobicity[6-8] is one of the most attractive roughness-induced wetting properties studied in recent years. On superhydrophobic surfaces (SHS), a water drop beads up because it remains suspended on top of the microgeometries and air is entrapped at the interface between liquid and solid (so-called composite state). With a large static contact angle (CA) and low contact angle hysteresis (CAH, i.e., the difference between advancing or maximum and receding or minimum contact angles[9]), natural SHS shows interesting surface properties, e.g., the self-cleaning property of some plant's leaves[10] and animal's wings,[11] the superfloating ability of water-strider,[12] and the antifogging property of mosquito compound eyes.[13] Motivated by many applications of SHS, researchers are trying to gain a comprehensive understanding of superhydrophobicity and find robust SHS.

Studies[14-17] have shown that the edge effect would play an important role in the pinning and depinning behaviors of three-phase contact line (TPCL) of drops on SHS, and thus affect the advancing and receding CAs, particularly for SHS consisting of pillar structures. For instance, on parallel grooved or wrinkled surfaces, the drop contact line shows a larger pinning effect or CAH in the orthogonal direction to the grooves, where the contact line meets the solid edge, than in the parallel direction to the grooves, where the contact line meets no solid edge.[18-20] On the other hand, drops on SHS may experience a transition from composite state to noncomposite state[21-23] (i.e., the TPCL may cross over the

solid edges of the microstructure and let liquid penetrate into the troughs of a rough surface), resulting in a loss of superhydrophobicity; see Figure 2-1. It is argued that a re-entrant design[24-27] for microgeometries of SHS would inhibit the TPCL of a liquid drop from crossing the solid edges and ensure a drop suspension even for low-surface-tension liquid. Understanding the edge effect is significant for designing such robust superhydrophobic or superoleophobic surfaces.

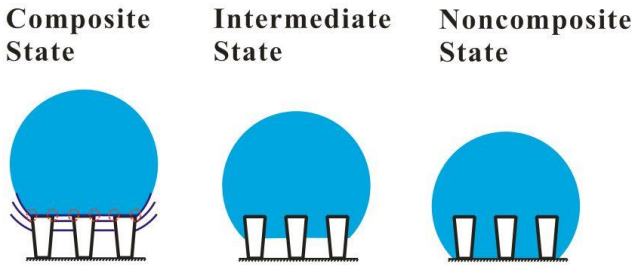

Figure 2-1. Schematic showing the transition of drop from composite state to noncomposite state. Note that the edges of the pillars play an important role for inhibiting the transition.

There are many studies (mostly by Mason et al.)[1, 28-37] dealing with the edge effect on wetting, but few of them have advanced the understanding beyond Gibbs'[38] inequality condition analysis for drop contact line at a solid edge. Oliver et al.[1] first examined Gibbs' results by studying water drop spreading behavior on pedestals with different sharp edges (defined by an angle subtended by the two surfaces forming the solid edge – "edge angle") theoretically and experimentally. They indicated that Gibbs' conclusion is mainly a geometrical consequence unaffected by the intrinsic nature of the edge (e.g., the selective adsorption of impurities on the edge). Later, Dyson[33] suggested that Gibbs' inequalities lack universal applicability and more specific qualifiers should be added for the

inequalities to apply. Nevertheless, his modified inequalities have already been known and attributed to Gibbs by other researchers (e.g., Oliver et al.[1]).

Gibbs' principle has been widely employed to explain the wetting phenomena taking place on microstructured surfaces,[35, 39-41] e.g., the origin of CAH on rough surfaces.[36, 42] Recently, with the increasing interest in SHS, researchers have realized the fundamental influence of edge effect in superhydrophobicity, especially in the stability of the composite state for a drop on SHS. The results in [14] indicated a remarkable deviation of measured CAs from the expected theoretical values on SHS. Hence, they suggested that the pinning effect of wetting at the solid edges of the microgeometries (or edge effect) should be taken into consideration as an important mechanism for SHS, but their explanation was somewhat tentative. By pressing a conical frustum into a liquid, Sheng et al.[37] observed that, depending on edge geometry and intrinsic CA, spreading of water around the edges of the frustum can be significantly hindered. Inspired by this, they made superhydrophobic surfaces with textures having microedges from material with low hydrophobicity.

As the study of an interface in contact with multiple edges (seen in SHS[16, 17]) is complex, first, a drop on a single pillar needs to be studied to gain a fundamental understanding of the edge effect.[2, 3, 43] In particular, most of the studies are focused on discussing the water drop suspension ability caused by the pinning effect of the pillar's edge. Study of a single-pillar model is also of practical interest for condensation on SHS, since a water drop may grow from a

small-sized drop sitting atop a single pillar.[44, 45] Extrand[2] proposed a model to predict the critical suspension volume of a drop on a single pillar based on Gibbs' inequality condition. The model accounts for both capillary forces and gravity and is only valid where the liquid surface tension at the contact line is directed upward. Du et al.[43] investigated the profiles of liquid drops at the tip of a cylindrical fiber after drop collapse. A spherical cap on the fiber tip and a full, symmetrical bell shape on the fiber body adjacent to the fiber tip were shown theoretically and experimentally. Tóth et al.[3] reported the suspension of water drops deposited on vertical single pillar with both circular and square cross sections by experimental and numerical studies. They have attributed the observed drop shapes to the geometric pinning of the contact line to the pillar's edge and found good consistency with Gibbs' inequality condition. Also, it is noted that Myshkis et al.[46] have provided a discussion for liquid in contact with an edge in the wall of a vessel (e.g., section 2.2.1.5 of the book). However, the analysis takes the form of high-level discussion, necessitating a detailed study as presented here. It is worth pointing out that, though authors[2, 3, 43] have also addressed the significance of the single-pillar model for understanding wetting on multipillar surfaces, the correlation between wetting on individual pillar structure and on multipillar structure (e.g., SHS) has not been demonstrated.

Despite the above studies, there is still a lack of an overarching framework to describe the thermodynamic mechanisms responsible for the edge effect. Particularly, each of the current papers[1-3, 32, 43] have examined a particular aspect

of the phenomenon. Different from the previous studies, in this work, we have provided a comprehensive and systematic investigation of the edge effect in a general form. A 3-D free energy model for water drop on top of a pedestal/pillar (cylindrical, upright frustum, and inverted frustum geometries) has been constructed. By providing the detailed free energy analysis around the edge, the thermodynamic origin of the edge effect can be understood. In the end, a universal wetting map can be generated, which brings about a general guide for understanding the wetting phenomena at the edge.

2.2 Theoretical Development

2.2.1 Edge Effect Theories

Edge effect is usually described by the model[1-3] given schematically in Figure 2-2a. Note that the drops described in Figure 2-2a are in equilibrium state (or the most stable state) as the drop volume is increased. By changing the edge angle, Φ, the model pillar with circular cross section varies from an upright frustum to an inverted frustum shape (see Figure 2-2b). For a drop placed on top of the pillar away from the pillar's edge (i.e., when the radius of drop contact circle, r, is less than that of the pillar's top, R), the equilibrium CA will be seen. If the pillar surface (top and side surfaces) is rigid, smooth, and homogeneous, the Young's angle (θ_Y) is the intrinsic CA which can be predicted by Young's equation

$$\gamma^{la}\cos\theta_Y = \gamma^{sa} - \gamma^{ls} \qquad (2\text{-}1)$$

where γ^{la}, γ^{sa}, and γ^{ls} are interfacial tension at liquid-air, solid-air and liquid-solid interfaces, respectively. As the drop volume is increased, TPCL is advancing and finally pinned at the pillar's edge ($r = R$); that is, the position of the contact line remains unchanged at the edge, but the apparent CA increases from θ_Y to a critical maximum value, θ_C, i.e., $\theta_C = \theta_Y + (180° - \Phi)$, which is attributed to Gibbs inequality condition. Oliver et al.[1] illustrated that three wetting states may take place after the contact line reaches the pillar's edge (in the absence of gravity), depending on the relationship between θ_Y and Φ:

(1) When $\Phi <= \theta_Y$: as the drop volume increases, the TPCL will be always pinned at the edge while the drop apparent CA approaches but never reaches θ_C ($\geq 180°$). This will be called case A.

(2) When $\Phi > \theta_Y$ and $\Phi > \theta_Y + 2\tan^{-1}(0.5 \cot \theta_Y)$: as the drop volume increases, the TPCL will first be pinned at the edge and the drop apparent CA approaches θ_C; after the drop apparent CA reaches θ_C, further increase of the drop volume will allow the TPCL to steadily move over the edge. This will be called case B.

(3) When $\theta_Y < \Phi < \theta_Y + 2\tan^{-1}(0.5 \cot \theta_Y)$: as the drop volume increases, the wetting behavior is the same as case B, before the drop CA reaches θ_C; however, unlike case B, after it reaches θ_C, the TPCL jumps suddenly and spread spontaneously down the side of the pillar. This will be called case C. Case C has been studied by Du et al.[43] experimentally and theoretically (e.g., $\theta_Y = 17°$ and

Φ=90°), showing a spherical cap on the fiber tip and a symmetrical bell-shaped meniscus on the fiber body adjacent to the fiber tip (after the drop collapse). However, it is still difficult to get a full physical picture for such wetting behavior. A clear explanation will be given in our thermodynamic analysis (see Section 2.3.3).

It is worth pointing out that the conclusions of Oliver et al.[1] are based on a volume restriction analysis. Thus, although it gives a description for the wetting behavior of drop TPCL at the edge with increasing volume, the wetting state of the drop on a single pillar with a constant volume is still unclear. For instance, if a drop with the same volume is deposited on top of a single pillar varying from upright frustum to inverted frustum geometries (see Figure 2-2b), it is difficult to use Oliver et al.'s results to explain the difference between them.

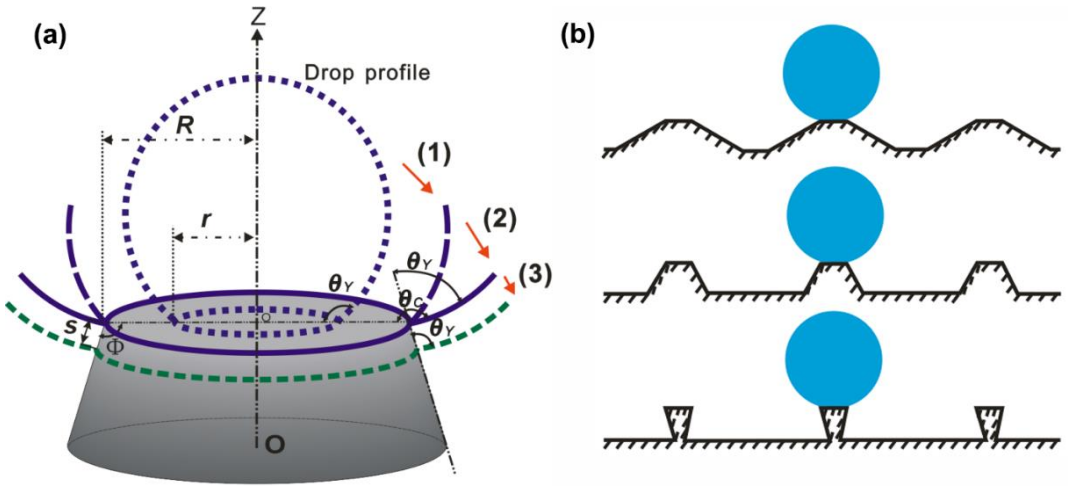

Figure 2-2. (a) Schematic depiction of the motion of the TPCL on a single pillar by increasing the volume: the TPCL is approaching the pillar's edge (1), pinned at the pillar's edge (2), and after crossing over the pillar's edge (3). Note that the drop profiles represent the drops in equilibrium state as the drop volume is increased. (b) Schematic showing drops with constant volume sitting on a single pillar from upright frustum to inverted frustum geometries. Note that the single pillar can be one of the periodically aligned pillars for a model SHS.

2.2.2 Thermodynamic Model

A 3-D free energy model is proposed to obtain a detailed knowledge of free energy (FE) states for an axisymmetric drop placed on top of a single pillar; see Figure 2-3. The following assumptions are made: (1) the gravity and line tension are ignored in order to simplify the model and focus on discussing the basic factors (edge angle, intrinsic CA and drop volume) affecting the edge effect; (2) the drop profile is assumed to be spherical when displaced beyond the edge for s << R (see Figure 2-2a); (3) the solid surface is rigid, isotropic, and homogeneous.

To probe energy states in the vicinity of an edge, we can consider receding of TPCL from edge A (see Figure 2-3) to an arbitrary position B and TPCL advancing to C from A. It is worth pointing that the drop profiles shown in Figure 2-3a or 2-3b are the drops with the same volume, which means the TPCL will be at different positions; as such, the states shown are not necessarily representing an equilibrium state. Some of the profiles shown may not exist in reality and are just defined/shown for the purpose of comparing the free energy states, to determine the minimum energy state. Considering first the receding case, when TPCL moves from A to B, CA will change from θ_A to θ_B (note that the apparent CA, θ_A or θ_B, is not necessarily equal to an equilibrium CA, as the drops may not be in an equilibrium state); also, the system FE will change from F_A to F_B due to the change of liquid-air, solid-air and liquid-solid interfacial areas. The system FE for the drop at A and B can be represented as

$$F_A = \gamma^{la} A_A^{la} + \gamma^{sa} A_A^{sa} + \gamma^{ls} A_A^{ls} + K \qquad (2\text{-}2)$$

$$F_B = \gamma^{la} A_B^{la} + \gamma^{sa} A_B^{sa} + \gamma^{ls} A_B^{ls} + K \qquad (2\text{-}3)$$

where A^{la}, $A^{sa}$and A^{ls} are the liquid-air, solid-air and liquid-solid interfacial area, respectively. K denotes the FE of the portion of the system that remains unchanged, e.g., from bulk phases. Thus, the corresponding change of FE for a drop receding from position A to B can be expressed by eq 2-4 (note that $\cos\theta_Y$ has been used as a proxy for the magnitude of the term "$(\gamma^{sa} - \gamma^{ls})/\gamma^{la}$" in the eq 2-4)

$$\Delta F_{\mathrm{A}\to\mathrm{B}}/\gamma^{\mathrm{la}} = (F_{\mathrm{B}} - F_{\mathrm{A}})/\gamma^{\mathrm{la}} = \frac{2\pi L_{\mathrm{B}}^2(1-\cos\theta_{\mathrm{B}})}{\sin^2\theta_{\mathrm{B}}} - \frac{2\pi L_{\mathrm{A}}^2(1-\cos\theta_{\mathrm{A}})}{\sin^2\theta_{\mathrm{A}}} + \pi(L_{\mathrm{A}}^2 - L_{\mathrm{B}}^2)\cos\theta_{\mathrm{Y}} \quad (2\text{-}4)$$

where L_A and L_B are the drop base radius (see Figure 2-3a) at positions A and B, respectively; note that the unit of energy (J/m^2) has been normalized with respect to γ (J/m^2). In addition, for a drop of constant volume (V), eq 2-5 is derived from geometrical analysis

$$V_{\mathrm{A}} = V_{\mathrm{B}} = \frac{\pi L_{\mathrm{B}}^3(1-\cos\theta_{\mathrm{B}})^2(2+\cos\theta_{\mathrm{B}})}{3\sin^3\theta_{\mathrm{B}}} = \frac{\pi L_{\mathrm{A}}^3(1-\cos\theta_{\mathrm{A}})^2(2+\cos\theta_{\mathrm{A}})}{3\sin^3\theta_{\mathrm{A}}} \quad (2\text{-}5)$$

where V_{A} and V_{B} are the drop volume at positions A and B, respectively.

Here, the FE state for the drop at position A, which is right at the pillar's edge, is selected to be the reference FE state and assigned an arbitrary value of zero, i.e., $F_{\mathrm{A}} = 0$. As a result, the normalized FE for the drop at any arbitrary position B (see Figure 2-3a) can be determined by solving eqs 2-4 and 2-5 via successive approximations. Note that the drop volume (V) at the reference position A (V_{A}) and the value of L_{A} (drop base radius; see Figure 2-3) should be given to define an initial state of the system. As a result, θ_{A} can be determined geometrically from eq 2-5.

Similarly, for TPCL advancing case (see Figure 2-3b), the FE equations and constant volume condition can be derived as follows:

$$\Delta F_{A\to C}/\gamma^{la} = (F_C - F_A)/\gamma^{la} = \frac{2\pi L_C^2(1-\cos\theta_C)}{\sin^2\theta_C} - \frac{2\pi L_A^2(1-\cos\theta_A)}{\sin^2\theta_A} - \pi(L_A + L_C)\frac{L_A - L_C}{\cos\Phi}\cos\theta_Y \qquad (2\text{-}6)$$

$$V_A = V_C = \frac{\pi L_C^3(1-\cos\theta_C)^2(2+\cos\theta_C)}{3\sin^3\theta_C} - \frac{1}{3}\pi L_{AC}\,(L_A^2 + L_A L_C + L_C^2)\sin\Phi \qquad (2\text{-}7)$$

where the parameters are illustrated in Figure 2-3b; V_C is the drop volume at position C. Note that the apparent CA for the drop at the arbitrary position C (θ_C) is defined as the angle between the tangent to the drop at the three-phase contact line and the horizon (see Figure 2-3b). Again, solving eqs 2-6 and 2-7, via successive approximation, the normalized FE at any position C can be found.

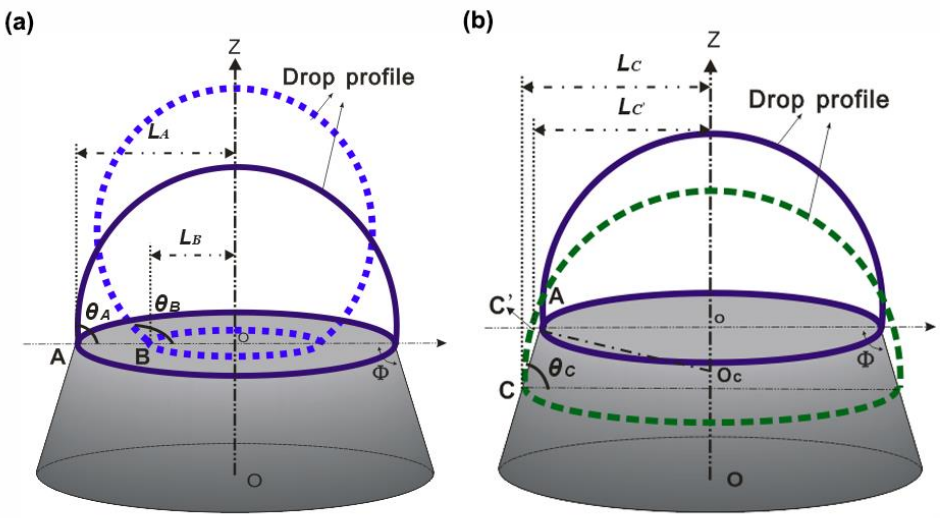

Figure 2-3. Illustration of FE analysis for a drop on a single pillar. (a) A drop sitting at the reference position A and an arbitrary position, B, before crossing over the edge. (b) A drop sitting at the reference point A and an arbitrary position, C, after crossing over the edge. Note that the apparent CA is defined as the angle between the tangent to the drop at the three-phase contact line and the horizon. If Φ = 180 °, the model represents a flat surface; if Φ < 90 °, the model pillar becomes an inverted trapezoid or a so called re-entrant structure.

Attention should be paid to the limitation for the existence for a spherical drop cap when the TPCL passes over the pillar's edge; if the edge angle is too small or the displacement of TPCL over the edge is too large, the pillar's edge may touch the drop cap. A criterion (eq 2-8) can be written as follows to avoid the analysis for a nonphysical situation described above:

$$L_{C'} = \sqrt{\frac{L_C^2}{\sin^2\theta_C} - \left(\frac{L_C}{\tan\theta_C} + L_{AC}\sin\Phi\right)^2} > L_A \qquad (2\text{-}8)$$

As it is seen in Figure 2-3b, if $L_{C'} > L_A$, a spherical drop profile can be satisfied; if $L_{C'} \leq L_A$, eq 2-8 is violated, indicating that the pillar's edge will touch the outline of the drop, and then the drop must split into two parts .

If gravity is present, the spherical cap shape may not hold for large volumes of drop. For the geometrical analysis, Young-Laplace equation should be applied to calculate the shape of the drop. Accordingly, the interfacial area term " A^{la}" in eqs 2-2 and 2-3 should be replaced with the solution for Young-Laplace equation. In addition, for the energy analysis, gravitational potential energy change should be considered. While the methodology will remain the same, the mathematical treatment of the problem will be more involved when gravity is considered. Moreover, for very small drops, the line tension may play a role in the edge effect. In particular, a positive line tension operating on a small drop resting on the pillar tends to reduce the length of the TPCL[47] and thus enhance the ability of a drop to remain suspended on a single pillar.

2.3 Results and Discussion

2.3.1 Model Verification Using Flat Surface Case

Before proceeding with the model analysis, we test the suitability of our model with analyzing the case of Φ = 180 º, i.e., a flat surface (see the inset of Figure 2-4). Figure 2-4 shows a typical FE curve for a drop (V = 2.8×10^{-4} μl) deposited on a flat surface (with θ_Y = 60 º, L_A = 4.6×10^{-5}m, θ_A = 100 º). One can see that a bowl-shaped FE curve contains a solid line part representing the drop

FE states at position C (an arbitrary position for drop after crossing over the reference position A) and a dotted line part representing the drop FE states at position B (an arbitrary position for drop before crossing the reference position A). In this case, one global minimum FE state is observed which is on the solid line part, with the corresponding CA of 60°. In other words, when a drop ($V = 2.8 \times 10^{-4}$ μl) is deposited on the flat surface, it will spread to a position C to reach an equilibrium drop state and exhibit an equilibrium CA (= 60°), as it should. This confirms the validity of the constructed model, since the minimum energy state CA coincides with the assumed intrinsic CA ($\theta_Y = 60°$) to conduct the calculation. The result shows good agreement with findings from a precious model[48] for the thermodynamic analysis of smooth, homogeneous solid surfaces. To further demonstrate the validation of the model, the results are also compared with the findings of the study by Oliver et al.[1] (see the Appendix B).

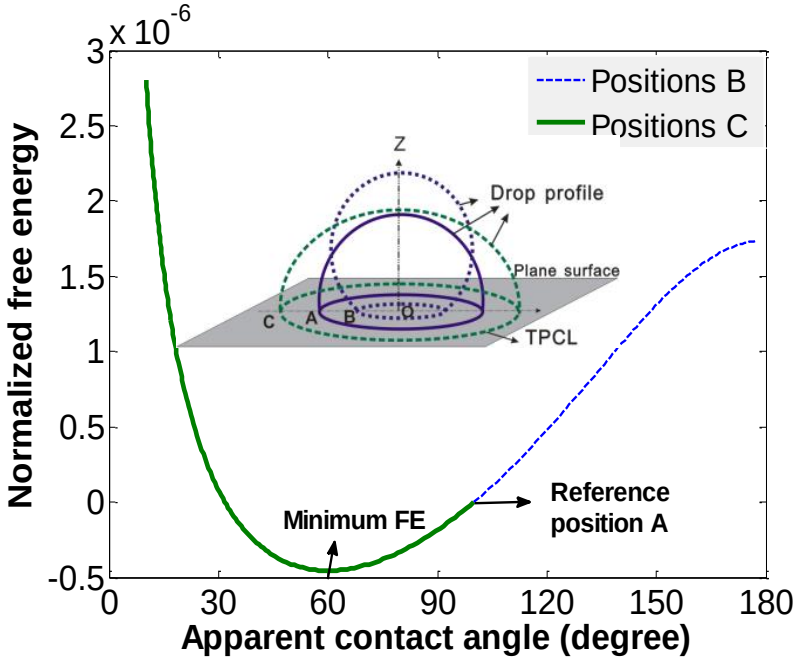

Figure 2-4. Normalized free energy as a function of the apparent CA on a flat surface (θ_Y = 60 º; $L_A = 4.6\times10^{-5}$m, Φ = 180 º; $V = 2.8\times10^{-4}$μl).

2.3.2 The Edge Effect on Apparent CA

In order to understand the edge effect, the thermodynamic model described above is applied to obtain the FE curves for drops ($V = 2.8\times10^{-4}$μl) placed on model surfaces (θ_Y = 60 º, $L_A = 4.6\times10^{-5}$m, θ_A = 100 º) with different edge angle Φ (e.g., 150 º and 120 º); see Figure 2-5. As illustrated in Figure 2-5b, the dotted line parts (the drop FE states at positions B) of the FE curves for the three model surfaces overlap with each other; that is, the FE states for drop TPCL at positions B are insensitive to the edge angle Φ (as they should be). In contrast, the solid line parts (the drop FE states at positions C) of the FE curves for the three model surfaces

(see Figure 2-5a) show an obvious difference. Compared to the FE curve for the drop on the flat surface (Φ = 180 º), the minimum FE state rises (from -45×10^{-8} to -4×10^{-8}) and the corresponding apparent CA shifts up to 90 º for the drop on the model surface with a smaller edge angle (Φ = 150 º). Meanwhile, the most stable drop TPCL on the model surface with Φ = 150 º is located at a position closer to the reference position A than that with Φ = 180 º (see the schematic illustration in Figure 2-5a, bottom view); as such, one can understand that the difference of FE states and wetting behavior for the two models is caused by the edge effect. This is the first time that a detailed explanation of thermodynamic origin of edge effect has been given. Moreover, further decrease of the edge angle will finally increase the minimum energy state CA to 100 º (note that θ_A = 100 º in this case) and thus the most stable TPCL is just at the edge (the reference position A); see Figure 2-5. In summary, it can be seen that an edge angle small enough can make the most stable drop TPCL be the position at the edge, without risking a drop collapse onto the sidewall of the pillar; i.e., the decrease of edge angle will increase the drop suspension ability for a pillar. This explains the reason that re-entrant micropillars[24-27] (Φ < 90 º) are preferred to construct robust-SHS or superoleophobic surfaces.

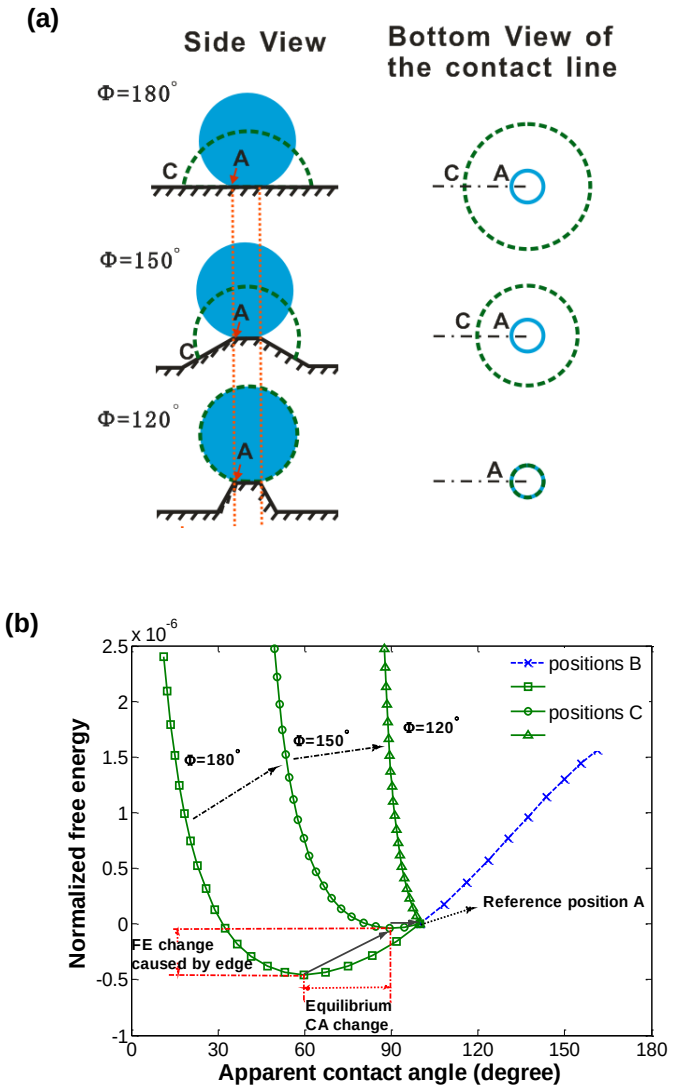

Figure 2-5. (a) Schematic showing drops placed on model surfaces with different edge angle, Φ (180 º, 150 º and 120 º). (b) Normalized FE curves as a function of the apparent CA for the cases shown in (a) (θ_Y = 60 º, L_A = 4.6×10^{-5}m, Φ = 120 º, 150 º and 180 º, V = 2.8×10^{-4} µl).

2.3.3 Four Typical Drop Wetting States

On the basis of the above discussion, the drop FE states at positions B (before crossing the edge) will not be affected by the edge angle Φ. Hence, in the

following discussion, only the drop FE states at positions C (after crossing over the edge) will be shown in the FE graphs and discussed. In order to find the effect of edge angle, Φ, on the drop wetting behavior, the normalized FE as a function of apparent CA and edge angle Φ are obtained for a drop (V = 0.01 μl) on single pillar (θ_Y = 60°, L_A = 4.6×10^{-5}m); see Figure 2-6. Note that, for a fixed edge angle, a slice of the FE curve can be obtained similar to Figure 2-5. One can see that, with increasing the edge angle from 20° to 130°, the FE curve is gradually dropping down and finally flipping over (i.e., the apparent CA will no longer increase with increasing displacement beyond the edge, *s*, see Figure 2-2a). Consequently, there must be a critical point (it is marked as the collapse point Φ_T in Figure 2-6a, e.g., Φ_T = 80° in this case) that before which, the drop minimum FE states will be at the reference position A; but after which, the drop minimum FE states will no longer be at the reference position A. The detail will be further discussed below.

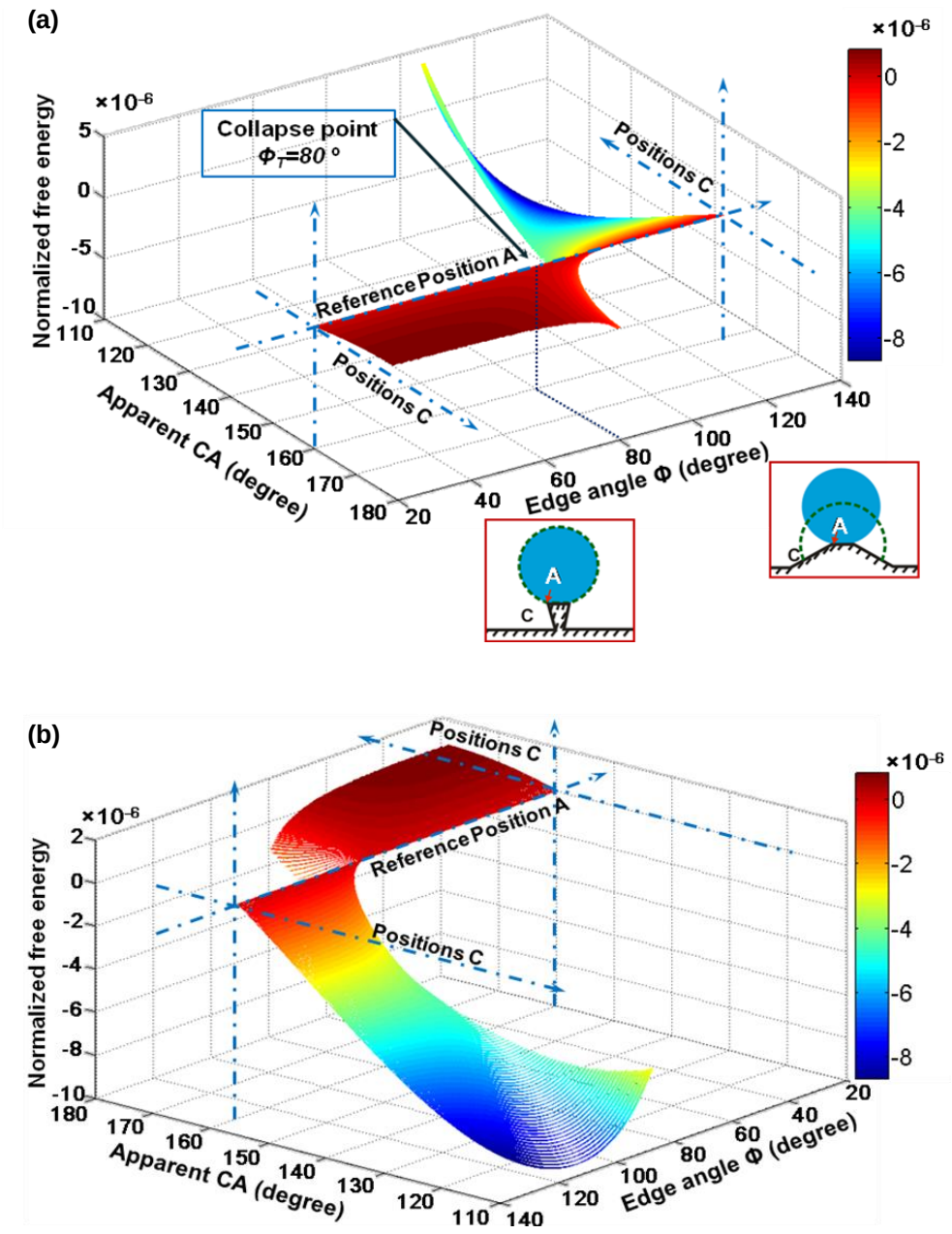

Figure 2-6. (a) Normalized FE of a drop sitting on single pillar as a function of apparent CA and edge angle Φ (θ_Y = 60 º, L_A = 4.6×10^{-5}m, V = 0.01 μl). (b) The same FE graph as (a), but enlarged and shown from a different perspective. Note that the reference position A refers to the edge of the pillar (see Figure 2-3).

In Figure 2-6a, four specific wetting cases (case 1, case 2, case 3, and case 4) are noted. These cases will be discussed in detail by analyzing the FE graphs shown in Figures 2-7, 2-8, and 2-9. Figure 2-7 shows the part of the FE graph for edge angle ranging from 40 ° to 60 °. In addition to the 3-D FE graph shown in Figure 2-7a, a family of 2-D FE curves is given in Figure 2-7b. One can see that the FE increases monotonously with an increasing apparent CA (which is approaching 180 °); see Figure 2-7b. This means that the most energetically favorable position for TPCL is at the edge. Meanwhile, the apparent CA most energetically favorable will be 160 ° for edge angle between 40 ° and 60 °, and the drop will not collapse to the side walls. Such drop wetting behavior is referred to as wetting case 1.

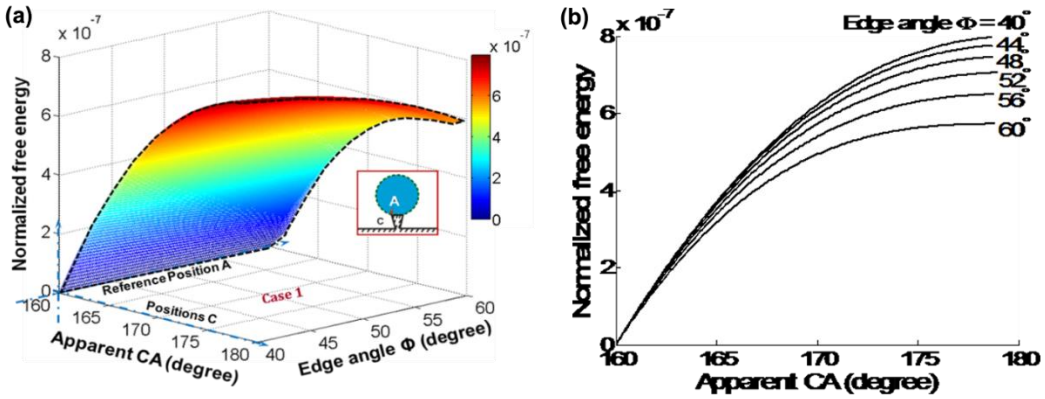

Figure 2-7. (a) Part of FE graph (Figure 2-6) for edge angle, Φ, ranging from 40° to 60 °, which is defined as wetting case 1. (b) FE curves in a two-dimensional graph. Note that the reference position A refers to the edge of the pillar; see Figure 2-3. The figure indicates that the apparent CA most energetically favorable is 160 °, and TPCL will remain at the edge (θ_Y = 60 °, $L_A = 4.6 \times 10^{-5}$m, V = 0.01 μl).

Figure 2-8 presents the part of FE graph for edge angle ranging from 60 ° to 95 °. In addition to the 3-D FE graph shown in Figure 2-8a and 8b, a family of 2-D FE curves is given in Figure 2-8c. Two wetting states can be determined. For the FE states of drops on single pillar with edge angle Φ = 60 °~80 °, the FE curve for a given edge angle, Φ, shows a convex shape; in other words, a free energy barrier (FEB) can be seen (see the enlargement in Figure 2-8b). This is also demonstrated in the 2-D FE chart when Φ is between 60 ° and 80 °, see Figure 2-8c. One can see that there is a minimum FE state at the reference position A when the apparent CA equals 160 °, indicating that the drop can be suspended stably on top of the pillar. However, unlike the 2-D FE curves in Figure 2-7b, the FE curves (Φ is between 60 ° and 80 °) shown in Figure 2-8c are not increasing monotonously with an increasing apparent CA. The normalized FE will finally drop down after reaching an energy peak (or FEB) with apparent CA approaching 180 °, and then stop at a position where the criterion (eq 2-8) for forming a spherical drop cap is violated. Thus, the drop state suspended on top of the pillar is metastable, because the FEB can be overcome if there is external energy provided, e.g., mechanical vibration. Namely, when the drop collapses down, the pillar's edge will finally touch the drop cap, at which point the drop must split into two parts as stated by Du et al.[43] (see Section 2.2.1 and Figure B-3 in Appendix B). Thus, the FEB is important for drop suspension on top of microstructures of SHS, preventing the transition from composite (Cassie) state to noncomposite (Wenzel) state. We refer to this wetting state as case 2. For the part of FE graph with edge angle Φ =

80 °~95 °, the drop FE states at the reference position A are no longer the minimum energy states (see Figure 2-8a and 8c). The normalized FE decreases monotonously with apparent CA approaching 180 °. As a result, a drop on pillars with edge angle $\Phi > 80°$ can no longer be suspended stably on the top, which is referred to as wetting case 3. As mentioned above, such critical edge angle, Φ_T (= 80 ° in this case), is considered the collapse point, after which the drop collapse onto sidewall takes place. Interestingly, it is found that the collapse point, Φ_T, corresponds to a relationship $\Phi_T = 180° - \theta_A + \theta_Y$, allowing us to find it more easily. Moreover, in case 3, the monotonously decreased FE curves will finally stop at a position where the criterion (eq 2-8) for forming a spherical drop cap is violated; i.e., the pillar's edge will touch the drop cap, and then the drop must split into two parts. Unlike case 1 and case 2, there is no stable or metastable drop state for case 3, i.e., any drop deposited on top of the pillar which is in case 3 will collapse down and split into two parts immediately.

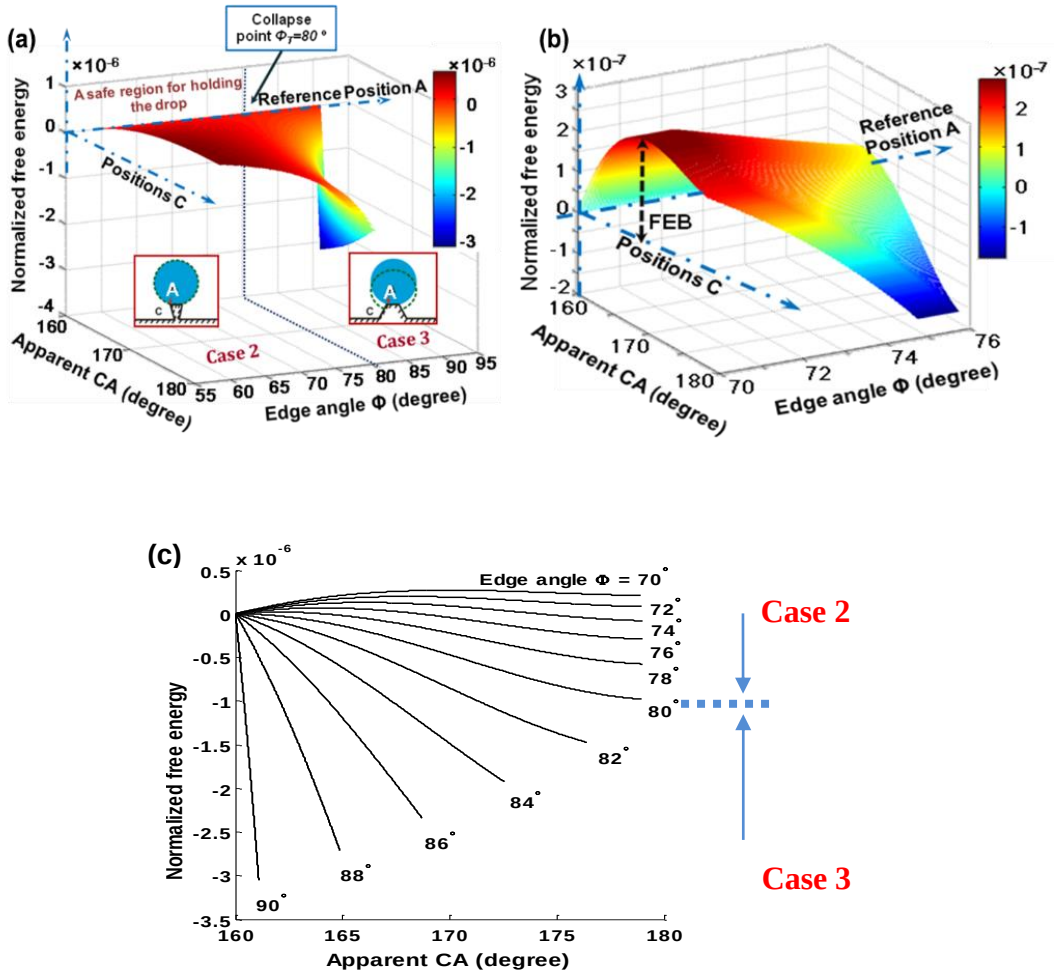

Figure 2-8. (a) Part of FE graph (Figure 2-6) for edge angle, Φ, ranging from 60° to 95°, which is defined as wetting case 2 (Φ = 60°~80°), and case 3 (Φ = 80°~95°). (b) Enlargement for edge angle, Φ, ranging from 70° to 75°, showing that TPCL is more energetically favorable to stay at the edge with θA = 160º. (c) FE curves in a two-dimensional graph for edge angle, Φ, ranging from 70° to 90° (θY = 60º, LA = 4.6×10-5m, V = 0.01㎕). For Φ > 80°, the TPCL will pass the edge. Note that the reference position A refers to the edge of the pillar; see Figure 2-3.

Figure 2-9 presents the part of FE graph for edge angle ranging from 100 ° to 150 °. In addition to the 3-D FE graph shown in Figure 2-9a, a family of 2-D FE

curves is given in Figure 2-9b. One can see that, different from the cases mentioned 1-3, bowl-shaped FE curves for each fixed edge angle can be observed; see Figure 2-9b. In particular, with increasing the edge angle, the minimum FE states will fall away from the reference position A. This indicates that TPCL is not energetically favorable to stay at the edge, and it will cross the edge. However, unlike case 2 and case 3, there is a position on the sidewall of the pillar where the drop TPCL can stay steadily. It is noted that the energetically favorable apparent angle (θ) corresponds to a relationship $\theta=180^{\circ}-\Phi+\theta_Y$, which refers to Oliver et al.'s critical (upper) value of CA at the edge.[1] Such a wetting state is referred to as case 4.

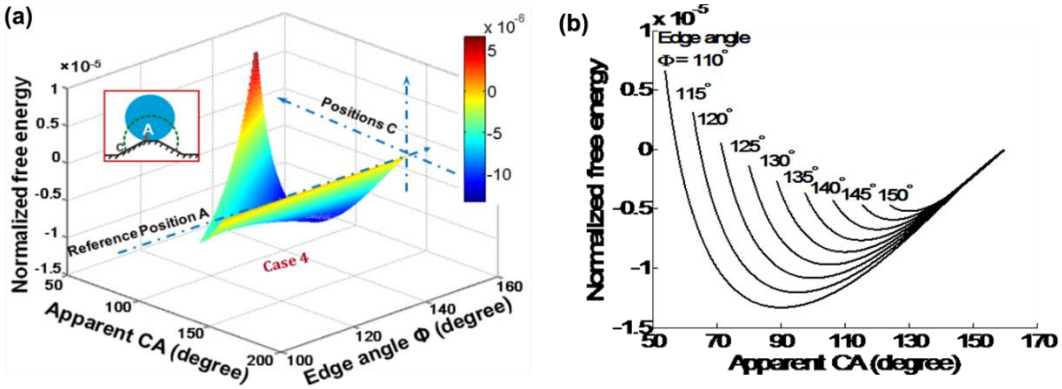

Figure 2-9. (a) Part of FE graph (Figure 2-6) for edge angle, Φ, ranging from 100 to 150°, which is defined as wetting case 4 (θ_Y = 60°, L_A = 4.6×10^{-5}m, V = 0.01μl). (b) FE curves in a two-dimensional graph for edge angle, Φ, ranging from 110° to 150°. Note that the reference position A refers to the edge of the pillar, see Figure 2-3. TPCL is not energetically favorable to stay at the edge, and it will move to the sidewall forming an apparent CA conforming to the criterion: $\theta=180^{\circ}-\Phi+\theta_Y$.

2.3.4 Wetting Map for Drops on a Single Pillar

On the basis of the above analysis, four different wetting cases (case 1, case 2, case 3, and case 4) have been shown. Note that this detailed thermodynamic model extends what has been known from Gibbs' criterion, as more possibilities for wetting configurations are revealed, e.g., case 2. Also, by defining various characteristics of change in FE, the boudaries for the four wetting cases can be found. Accordingly, a wetting map for describing the four wetting cases can be obtained in terms of edge angle (Φ) and intrinsic CA (θ_Y). With the case ($\theta_Y = 60^\circ$, $L_A = 4.6 \times 10^{-5}$m, $V = 0.01\,\mu$l) illustrated in Section 2.3.3, for example, three critical edge angles (60°, 80°, and 100°, see symbols marked by arrows in Figure 2-10) can be found to determine the boundaries among the four wetting cases. Note that $\Phi = 80^\circ$ is on the collapse transition line $\Phi_T = 180^\circ - \theta_A + \theta_Y$. Similarly, the other critical edge angles for separating the four wetting cases can also be determined with various intrinsic CA (see symbols in Figure 2-10). As a result, the wetting map for defining the four wetting regions of a drop ($V = 0.01\,\mu$l) placed on top of a pillar ($L_A = 4.6 \times 10^{-5}$m) is obtained (see Figure 2-10). Note that the collapse transition line is dependent on the drop volume.

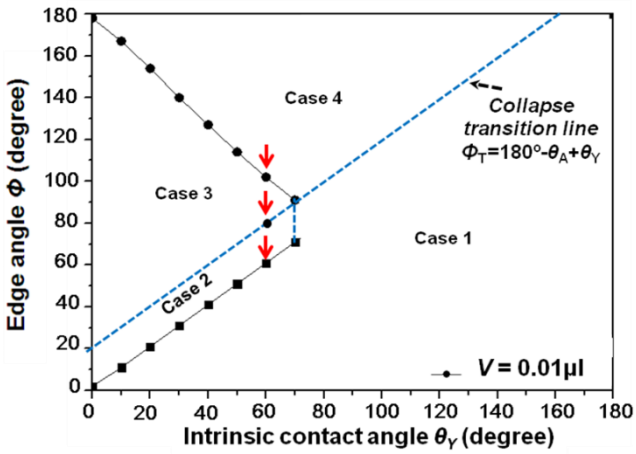

Figure 2-10. Wetting map for drop with fixed volume (L_A = 4.6×10^{-5}m, V = 0.01 μl) on single pillars in terms of edge angle (Φ) and intrinsic CA (θ_Y). Note that the collapse transition line is dependent on the drop volume (in this case, when V = 0.01 μl, θ_A=160 ° and Φ_T = 180 º-θ_A+θ_Y =20 º + θ_Y). Solid lines are to guide the eyes.

In a similar way, the wetting map for drops with various volumes can also be determined; see Figure 2-11a. One can see that, as the drop volume decreases from an infinitely large value to a small value (θ_A decreases from 180 ºto a small value), the collapse transition line (Φ_T = 180 º-θ_A+θ_Y) defining the boundaries between case 2 and case 3, and case 1 and case 4 is shifting up; the boundaries for case 3 and case 4, and case 2 and case 1 are also changing; see Figure 2-11a. Moreover, if the drop volume is nondimensionalised with the cube of pillar radius (V/L_A^3 = $[\pi(1-\cos\theta_A)^2(2+\cos\theta_A)/\,3\sin^3\theta_A]$), the comprehensive effect of drop volume and pillar radius on the wetting map can be combined and represented only by the parameter, θ_A (see Figure 2-11b); in other words, if the drop volume V increases proportionally with L_A^3, the parameter θ_A as well as the

wetting map will remain unchanged. As a result, Figure 2-11b showing the effect of θ_A on the wetting map includes the combined effect of drop volume and pillar radius. Interestingly, for pillar with a fixed pillar radius, it is noted that the area of wetting in case 3 and case 4 will decrease with decreasing drop volume. This is understandable, because a decrease of drop volume will cause a decrease in the possibility of drop collapse for drop deposited on top of a single pillar. This wetting map provides a framework for choosing the parameters of the pillar, in order to gain maximum drop suspension ability.

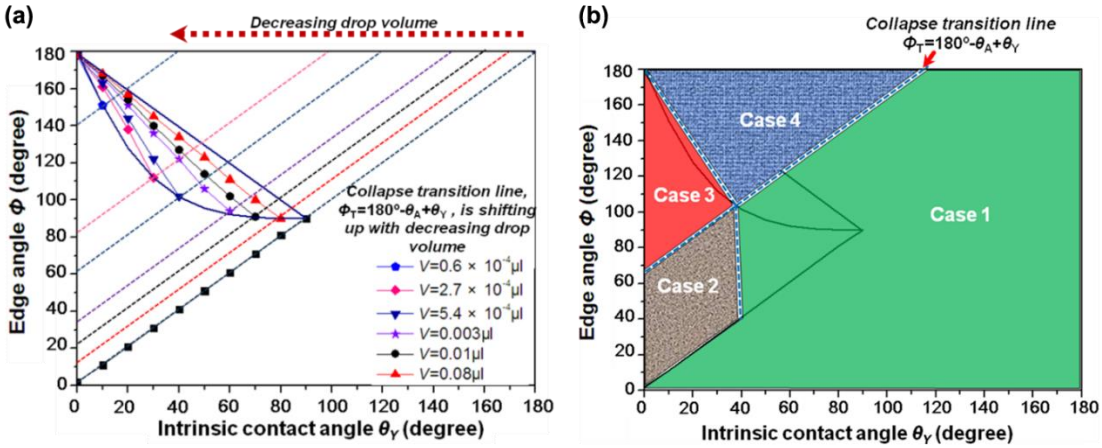

Figure 2-11. (a) Wetting map for drops on single pillars with varying drop volume in terms of edge angle (Φ) and intrinsic CA (θ_Y). lines are to guide the eyes. (b) The same wetting map as shown in (a), taking θ_A = 115 °as an example.

2.4 Conclusions

A 3-D free energy analysis method to investigate the energetic states of drops on a single pillar with various edge angles and intrinsic CAs is presented. A clear thermodynamic depiction of the origin of the edge effect has been given by the

analysis of drop FE levels before and after crossing the edge. Results show good consistency with previous literature and expand the current understanding in Gibbs' inequality condition. In particular, four wetting cases for drops on single pillars have been observed: case 1, a stable drop state on top of the pillar without risking the drop collapse onto the pillar sidewall; case 2, a metastable drop state on top of the pillar, which may experience a complete drop collapse and split (into two parts, i.e., a spherical cap on the fiber tip and a full, symmetrical bell on sidewall) if the FEB is overcome with the help of external FE provided from extra sources; case 3, an immediate drop collapse by spilling over the edge completely and split into two parts; case 4, a drop collapse by spilling over the edge while the TPCL can stay steadily at the position of sidewall. Finally, a wetting map for describing the four wetting regions is obtained in terms of edge angle (Φ) and intrinsic CA (θ_Y). The results have provided fundamental rules to follow for designing pillars with maximum drop suspension ability by controlling the edge effect.

References

(1) Oliver, J. F.; Huh, C.; Mason, S. G. *J. Colloid Interface Sci.* **1977,** *59*, 568-81.

(2) Extrand, C. W. *Langmuir* **2005,** *21*, 10370-10374.

(3) Tóth, T.; Ferraro, D.; Chiarello, E.; Pierno, M.; Mistura, G.; Bissacco, G.; Semprebon, C. *Langmuir* **2011,** *27*, 4742-4748.

(4) Pan, Q.; Wang, M. *ACS Appl. Mater. Interfaces* **2009,** *1*, 420-423.

(5) Zhang, J. H.; Wang, J. M.; Zhao, Y.; Xu, L.; Gao, X. F.; Zheng, Y. M.; Jiang, L. *Soft Matter* **2008,** *4*, 2232-2237.

(6) Quere, D. *Ann. Rev. Mater. Res.* **2008,** *38*, 71-99.

(7) Li, W.; Amirfazli, A. *J. Colloid Interface Sci.* **2005,** *292*, 195-201.

(8) Shirtcliffe, N. J.; McHale, G.; Atherton, S.; Newton, M. I. *Adv. Colloid Interface Sci.* **2010,** *161*, 124-138.

(9) Pierce, E.; Carmona, F. J.; Amirfazli, A. *Colloids Surfaces, A* **2008,** *323*, 73-82.

(10) Koch, K.; Bhushan, B.; Jung, Y. C.; Barthlott, W. *Soft Matter* **2009,** *5*, 1386-1393.

(11) Zheng, Y.; Gao, X.; Jiang, L. *Soft Matter* **2007,** *3*, 178-182.

(12) Gao, X.; Jiang, L. *Nature* **2004,** *432*, 36.

(13) Gao, X.; Yan, X.; Yao, X.; Xu, L.; Zhang, K.; Zhang, J.; Yang, B.; Jiang, L. *Adv. Mater. (Weinheim, Ger.)* **2007,** *19*, 2213-2217.

(14) Kurogi, K.; Yan, H.; Tsujii, K. *Colloids Surfaces, A* **2008,** *317*, 592-597.

(15) Herminghaus, S.; Brinkmann, M.; Seemann, R. *Ann. Rev. Mater. Res.* **2008,** *38*, 101-121.

(16) Dorrer, C.; Ruehe, J. *Langmuir* **2006,** *22*, 7652-7657.

(17) Dorrer, C.; Ruehe, J. *Langmuir* **2007,** *23*, 3179-3183.

(18) Yoshimitsu, Z.; Nakajima, A.; Watanabe, T.; Hashimoto, K. *Langmuir* **2002,** *18*, 5818-5822.

(19) Li, W.; Fang, G.; Li, Y.; Qiao, G. *J. Phys. Chem. B* **2008,** *112*, 7234-7243.

(20) Semprebon, C.; Mistura, G.; Orlandini, E.; Bissacco, G.; Segato, A.; Yeomans, J. M. *Langmuir* **2009,** *25*, 5619-5625.

(21) Patankar, N. A. *Langmuir* **2004,** *20*, 7097-7102.

(22) Sbragaglia, M.; Peters, A. M.; Pirat, C.; Borkent, B. M.; Lammertink, R. G. H.; Wessling, M.; Lohse, D. *Phys. Rev. Lett.* **2007,** *99*.

(23) Li, W.; Amirfazli, A. *Adv. Colloid Interface Sci.* **2007,** *132*, 51-68.

(24) Tuteja, A.; Choi, W.; Ma, M.; Mabry, J. M.; Mazzella, S. A.; Rutledge, G. C.; McKinley, G. H.; Cohen, R. E. *Science* **2007,** *318*, 1618-1622.

(25) Marmur, A. *Langmuir* **2008,** *24*, 7573-7579.

(26) Im, M.; Im, H.; Lee, J. H.; Yoon, J. B.; Choi, Y. K. *Soft Matter* **2010,** *6*, 1401-1404.

(27) Karlsson, M.; Forsberg, P.; Nikolajeff, F. *Langmuir* **2009,** *26*, 889-893.

(28) Oliver, J. F.; Huh, C.; Mason, S. G. *J. Adhesion* **1977,** *8*, 223-234.

(29) Oliver, J. F.; Mason, S. G. *J. Colloid Interface Sci.* **1977,** *60*, 480-487.

(30) Oliver, J. F.; Huh, C.; Mason, S. G. *Colloids Surfaces* **1980,** *1*, 79-104.

(31) Bayramli, E.; Mason, S. G. *J. Colloid Interface Sci.* **1978,** *66*, 200-202.

(32) Mori, Y. H.; Van de Ven, T. G. M.; Mason, S. G. *Colloids Surfaces* **1982,** *4*, 1-15.

(33) Dyson, D. C. *Phys. Fluids* **1988,** *31*, 229-32.

(34) Zhang, J.; Gao, X.; Jiang, L. *Langmuir* **2007,** *23*, 3230-3235.

(35) Berthier, J.; Loe-Mie, F.; Tran, V. M.; Schoumacker, S.; Mittler, F.; Marchand, G.; Sarrut, N. *J. Colloid Interface Sci.* **2009,** *338*, 296-303.

(36) Kalinin, Y. V.; Berejnov, V.; Thorne, R. E. *Langmuir* **2009,** *25*, 5391-5397.

(37) Sheng, X.; Zhang, J.; Jiang, L. *Langmuir* **2009,** *25*, 9903-9907.

(38) Gibbs, J. W. *"Scientific Papers"* **1906**, 326.

(39) Wang, J.; Chen, D. *Langmuir* **2008,** *24*, 10174-10180.

(40) Ondarcuhu, T.; Piednoir, A. *Nano Lett.* **2005,** *5*, 1744-1750.

(41) Extrand, C. W.; Moon, S. I. *Langmuir* **2008,** *24*, 9470-9473.

(42) Kalinin, Y.; Berejnov, V.; Thorne, R. E. *Microfluid. Nanofluid.* **2008,** *5*, 449-454.

(43) Du, J.; Michielsen, S.; Lee, H. J. *Langmuir* **2010,** *26*, 16000-16004.

(44) Nosonovsky, M.; Bhushan, B. *Nano Letters* **2007,** *7*, 2633-2637.

(45) Varanasi, K. K.; Hsu, M.; Bhate, N.; Yang, W. S.; Deng, T. *Appl. Phys. Lett.* **2009,** *95*.

(46) Myshkis, A. D.; Babskii, V. G.; Kopachevskii, N. D.; Slobozhanin, L. A.; Tyuptsov, A. D., *Low-gravity fluid mechanics, mathematical theory of capillary phenomena*. Springer-Verlag Berlin Heidelberg: 1987.

(47) Amirfazli, A.; Neumann, A. W. *Adv. Colloid Interface Sci.* **2004,** *110*, 121-141.

(48) Li, D.; Neumann, A. W., *Applied surface thermodynamics*. Marcel Dekker, Inc.: New York, 1996.

Chapter 3 - Wetting Transition on Microstructured Surfaces: A Thermodynamic Approach[2]

3.1 Introduction

Surface wettability can be tuned by designing surface chemistry and roughness (or microstructures). Depending on the surface microstructure patterns, two typical wetting states, i.e., the noncomposite (complete penetration of liquid into the troughs of surface microstructures with only solid-liquid interface under the drop), and the composite (the drop is suspended by the microstructures with the air pockets trapped under the drop) can be achieved on rough surfaces. Researchers are particularly interested in the composite wetting states, also known as superhydrophobicity[1] (water-repellent) and superoleophobicity[2] (oil-repellent), for its potential applications in fields of self-cleaning, friction reduction, anti-icing, etc. Two key issues related to superhydrophobic surfaces (SHS) have been widely studied in the past: a), the issue of contact angle hysteresis which is related to the drop wetting (advancing or receding) in the horizontal direction of the microstructured surface; b) the issue of the robustness of superhydrophobicity which is related to the drop penetrating in the vertical direction into the microstructured surface (i.e., drop wetting transition from initial composite to

[2] This work is to be submitted for publication shortly

noncomposite states or vice versa).

A wetting diagram,[3, 4] relating the apparent contact angle (CA), θ', and the Young's CA, θ_Y (i.e., the intrinsic CA of the material), is usually used to determine the wetting states on rough surfaces, see Figure 3-1. As the Young's CA decreases in the hydrophobic/oleophobic region ($\theta_Y > 90°$), eqs 3-1 (Cassie-Baxter equation[5]) and 3-2 (Wenzel's equation[6]) are successively obeyed for composite (solid line) and noncomposite (dashed line) states,

$$\cos\theta' = f\cos\theta_Y - (1 - f) \qquad (3\text{-}1)$$

$$\cos\theta' = r\cos\theta_Y \qquad (3\text{-}2)$$

where f is the Cassie's area fraction of the liquid in contact with the solid; r is the Wenzel's roughness factor as the ratio between the actual area and geometric projected area for a wetting surface. Note that eq 3-1 is a simplified form of Cassie-Baxter equation, which is only valid for a drop sitting atop flat-top surface feature (e.g. cylindrical posts).[7] The critical value of Young's CA for dividing the two wetting states is corresponding to $\cos\theta_C = (f\text{-}1)/(r\text{-}f)$ for a flat-top surface feature. As the Young's CA further decreases to the hydrophilic/oleophilic region ($\theta_Y < 90°$), the wetting states would switch from the noncomposite state (dashed line) to a special hemi-wicking state (dotted line), and the critical value of Young's CA is corresponding to $\cos\theta_{C'} = (1\text{-}f)/(r\text{-}f)$.[8] Note that the apparent CA of the hemi-wicking state follows a modified Cassie-Baxter equation for a flat-top surface feature:[8]

$$\cos\theta' = f\cos\theta_Y + (1 - f) \qquad (3\text{-}3)$$

According to Figure 3-1, the composite state could exist only if the Young's CA (θ_Y) is larger than the critical value θ_C = acos((*f*-1)/(*r*-*f*)). Since the maximum Young's CA found for the material with the lowest surface free energy for water today is approximately 120°,[9] only the small hatched area in Figure 3-1 (-0.5 < cosθ_Y < (*f*-1)/(*r*-*f*)) is expected to show superhydrophobicity (i.e., composite state for water). However, experimental observations show that drops on rough surfaces made with materials of moderate hydrophobicity ((*f*-1)/(*r*-*f*) < cosθ_Y < 0) and even hydrophilicity[10-13] (cosθ_Y > 0) could also show composite states (see the dash-dotted line in Figure 3-1), depending on the design of microgeometrical shapes (e.g., re-entrant microstructures[14-16]). Such phenomena could not be simply explained by the wetting diagram shown in Figure 3-1, which provides no information for deciding the stability of the wetting states. To design superhydrophobic/superoleophobic surfaces on hydrophilic/oleophilic materials, a thermodynamic understanding of the factors responsible for the wetting stability is needed.

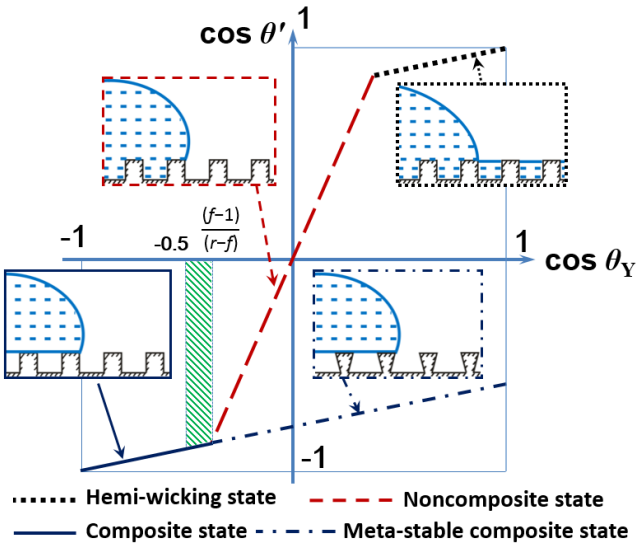

Figure 3-1. A wetting diagram schematic relating the apparent CA, θ', and the Young's CA, θ_Y, for rough surfaces. Note that the liquid is not limited to water; however, since the maximum Young's CA found for water today is approximately 120 °, only the small hatched area ($-0.5 < \cos\theta_Y < (f-1)/(r-f)$) is expected to show superhydrophobicity (i.e., composite state for water).

It should be pointed out that Bico et al.[8] have demonstrated that the composite state would be thermodynamically stable only if $\theta_Y > \theta_C$ (= acos $(f-1)/(r-f)$) by comparing the interfacial energy variation between composite and noncomposite states. Thus, the composite state (the dash-dotted line shown in Figure 3-1) in the moderate hydrophobic and hydrophilic regions for a drop should be in a local energy minima and separated by a transition FE barrier from the noncomposite state. Such FE barrier is significant for determining the stability of composite states of a drop on rough surfaces. Li et al.[17] have studied the energy difference between composite and noncomposite states for wetting on microstructured surfaces with pillars by a 2D thermodynamic model, which did

not consider the transition FE barriers.

Theoretical studies by Patankar[18, 19] and Marmur[20, 21] first addressed the importance of transition FE barrier in designing robust SHS. They found that even for the case that the noncomposite state was at a lower energy state, drop may still remain in composite state because of the transition FE barrier. However, their models have involved Wenzel's roughness and Cassie's fraction factors, which cannot provide the detailed information of geometrical effects. This is because different geometrical structures could result in the same Wenzel's roughness and Cassie's fraction. Later, Barbieri et al.[22] have modeled the transition FE barriers for cylindrical pillars with edge angle, Φ, fixed at 90°, and thus the effect of re-entrant structure in drop wetting transition was not considered. Bormashenko et al.[23, 24] have modeled the wetting transition on parallel grooves (i.e., a 2D model), which may not be so consistent with the practical case of 3D pillars. Also, drop wetting on parallel grooves would become anisotropic[25, 26] which led to making many simplifications. The 3D model for wetting transition on pillars with re-entrant structures (Φ was set to be smaller than 90°) that was considered in [23], also required many simplifications. For example, in the model of the inverted frustum geometries,[23] the transition FE barrier equation obtained could not be applied to upright frustum geometries and cylindrical pillars, since one parameter (i.e., the opening angle of the cone) in their equation only exists in the inverted frustum. Moreover, both Barbieri et al.[22] and Bormashenko et al.[23, 24] have ignored the volume change of liquid in the troughs of the microstructures during transition.

In addition, effects of re-entrant structures with concave and convex side walls in superhydrophobicity have been widely discussed in the past. Both of them are basic elements for constructing robust SHS, e.g., superhydrophobic animal feathers,[27] oleophobic fabrics,[28] and cuticle folding on plants.[29] Marmur[20] has analyzed the wetting on 2D concave and convex protrusions. Because Wenzel's roughness and Cassie's fraction have been involved in the model instead of some specific microgeometrical parameters, some very general conclusions was obtained. As a result, detailed transition FE barriers are still missing.

Whyman et al.[23] modeled a spherical cavity for calculating the transition FE barrier. However, wetting in one single spherical cavity is far from the practical superhydrophobic surfaces, which is usually composed of a number of microstructures. Whyman et al.[23] also modeled a microstructured surface built of ensembles of balls. The transition FE barrier equation they obtained is insensitive to the ball spacing, indicating a gross simplification which may not be consistent to practical cases. Again, the details of wetting transition FE barriers was missing.

Another point that we will study here is that the transition FE barriers discussed in literatures are all related to the transition from composite to noncomposite states. This is because transitions from noncomposite to composite states are extremely difficult to be observed experimentally and thus the corresponding transition energy (from noncomposite to composite) has usually been ignored. However, such transition does exist[30-35] and may be significantly

important for designing robust SHS. For example, during condensation, drops initially formed at noncomposite states (condensation may happen in the troughs of the microstructures) would experience a transition to composite states.[30] The relatively small transition FE barrier from noncomposite to composite may be responsible for such phenomena, which should be emphasized in designing robust SHS.

In the present study, a first-principle 3D thermodynamic model is proposed to investigate the wetting transition. Effects of various surface factors, including intrinsic CA, edge angle and length scale factor, on drop wetting transition are studied systematically. The roles of transition energy barriers from composite to noncomposite states, as well as from noncomposite to composite states are explained.

3.2 System Definition

In this study, wetting on microstructured surfaces made of pillars with straight side walls that are either upright or inverted frustum or cylindrical, see Figure 3-2a, 3-2b and 3-2c, will be modeled. A three-dimensional model is constructed from a first-principle thermodynamic view, to understand the fundamental effects of surface parameters, e.g., the intrinsic CA; pillar width, a; pillar spacing, b; and edge angle, Φ. Additionally, wetting on two typical re-entrant microstructures (arrays of microstructures with convex and concave side walls, which have symmetrical form in 3D, see Figure 3-2d) will be studied to

learn about details of the FE states for wetting transition.

To construct the model for the study of FE states, the following assumptions were made: (1) the gravity and line tension are ignored in order to simplify the model and focus on discussing the basic factors (intrinsic CA, edge angle and length scale) affecting the transition FEB; (2) the drop size is millimeter in scale and is much larger than the dimension of surface features; (3) drop profile is a spherical cap and the liquid-air interface under the drop is flat; (4) the solid surface is rigid, isotropic, and homogeneous.

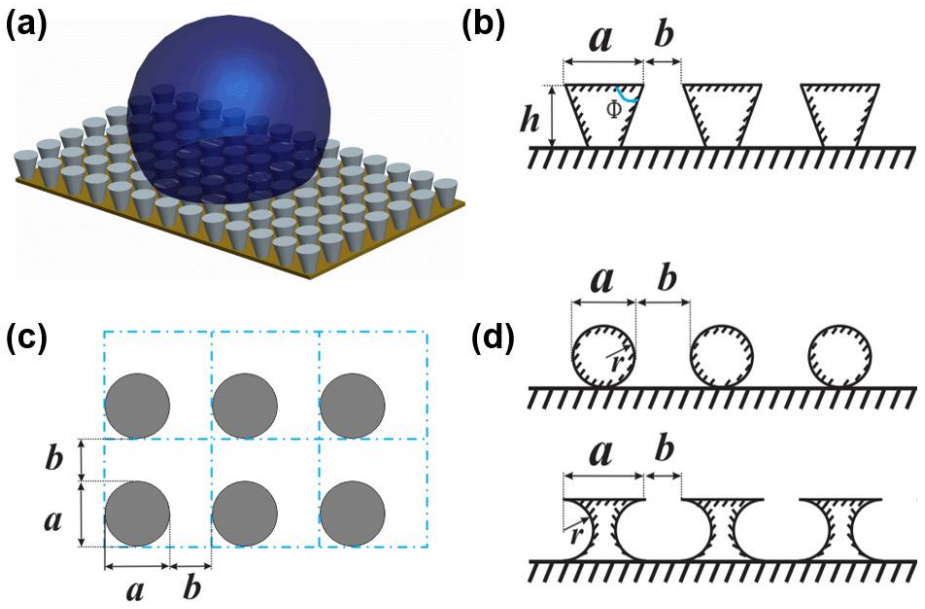

Figure 3-2. (a) A 3D schematic showing a drop sitting on the microstructured surface. (b) Side view of the microstructures made of pillars with straight side wall (inverted frustum); by changing edge angle Φ, upright or inverted frustum geometries can be obtained. (c) Top view of the microstructures shown in (a) or (b). (d) Side view of the two typical re-entrant microstructures with convex and concave side walls. Note that the microstructures have symmetrical form in 3D, and thus the top view of them are all appear as in (c).

3.3 Thermodynamic Analysis

First, the model of drop wetting on microstructured surfaces made of pillars with straight side wall is discussed. To probe energy states, we consider the drop with three-phase contact line (TPCL, beneath the drop) sitting at an arbitrary position A (an initial composite state, with the drop base radius variable) to be a reference drop state, see Figure 3-3a. Note that the drop profiles shown in Figure 3-3 are the drops with the same volume; as such, the states shown are not necessarily representing an equilibrium state. Some of the profiles shown are just defined for the purpose of comparing the free energy states to determine the minimum energy state. When TPCL penetrates into asperities from positions A to B (an intermediate composite state), see Figure 3-3a, CA changes from θ_A to θ_B (note that the apparent CA, θ_A or θ_B, is not necessarily equal to an equilibrium CA, as the drop may not be in an equilibrium state); also, the system FE will change from F_A to F_B due to the change of liquid-air, solid-air and liquid-solid interfacial areas. The system FE for the drop at positions A and B can be represented as:

$$F_{\mathrm{A}} = \gamma^{\mathrm{la}} A_{\mathrm{A}}^{\mathrm{la}} + \gamma^{\mathrm{sa}} A_{\mathrm{A}}^{\mathrm{sa}} + \gamma^{\mathrm{ls}} A_{\mathrm{A}}^{\mathrm{ls}} + K \qquad (3\text{-}4)$$

$$F_{\mathrm{B}} = \gamma^{\mathrm{la}} A_{\mathrm{B}}^{\mathrm{la}} + \gamma^{\mathrm{sa}} A_{\mathrm{B}}^{\mathrm{sa}} + \gamma^{\mathrm{ls}} A_{\mathrm{B}}^{\mathrm{ls}} + K \qquad (3\text{-}5)$$

where A^{la}, A^{sa} and A^{ls} are the liquid-air, solid-air and liquid-solid interfacial area, respectively. K denotes the FE of the portion of the system that remains unchanged, e.g., from bulk phases. Thus, the corresponding change of FE for a

drop at two states of A and B can be expressed by eq 3-6 (note that $\cos\theta_{\mathrm{Y}}$ has been used as a proxy for the magnitude of the term $(\gamma^{\mathrm{sa}}-\gamma^{\mathrm{ls}})/\gamma^{\mathrm{la}}$ in the eq 3-6):

$$\begin{aligned}\Delta F_{\mathrm{A}\to\mathrm{B}}/\gamma^{\mathrm{la}} &= (F_{\mathrm{B}}-F_{\mathrm{A}})/\gamma^{\mathrm{la}} \\ &= 2\pi L_0^2\left(\frac{1-\cos\theta_{\mathrm{B}}}{\sin^2\theta_{\mathrm{B}}}-\frac{1-\cos\theta_{\mathrm{A}}}{\sin^2\theta_{\mathrm{A}}}\right) \\ &+\frac{\pi^2L_0^2}{(a+b)^2}\left(\frac{a^2}{4}-\left(\frac{a}{2}-\frac{H_B}{\sin\Phi}\cos\Phi\right)^2\right)-\frac{H_B\pi^2L_0^2}{\sin\Phi(a+b)^2}(a \\ &-\frac{H_B}{\sin\Phi}\cos\Phi)\cos\theta_{\mathrm{Y}} \qquad (3\text{-}6)\end{aligned}$$

where F_{A} and F_{B} are the free energy states for drops at the positions A and B, respectively; L_0 is the drop base radius for drops both at positions A and B; H_{B} is the penetration height of the drop at position B; Φ is the edge angle of the cylindrical pillar; note that the unit of free energy ($\mathrm{J/m^2}$) has been normalized with respect to γ ($\mathrm{J/m^2}$). For a drop of constant volume (V), $V_{\mathrm{A}}=V_{\mathrm{B}}$. Note that the contact line of the drop is treated to be circular, and the number of the unit cell under the drop is expressed as $(\pi L_0^2)/(a+b)^2$.

Similarly, the FE difference of a drop between the initial composite and noncomposite states with the drop contact line at the same arbitrary position, see Figure 3-3b, can be expressed by eq 3-7:

$$\Delta F_{\mathrm{com}\to\mathrm{non}}/\gamma^{\mathrm{la}} = \frac{F_{\mathrm{non}} - F_{\mathrm{com}}}{\gamma^{\mathrm{la}}}$$

$$= 2\pi L_0^2 \left(\frac{1-\cos\theta_{\mathrm{non}}}{\sin^2\theta_{\mathrm{non}}} - \frac{1-\cos\theta_{\mathrm{com}}}{\sin^2\theta_{\mathrm{com}}}\right)$$

$$- \frac{\pi L_0^2}{(a+b)^2}\left((a+b)^2 - \frac{\pi a^2}{4}\right)$$

$$- \frac{\pi L_0^2}{(a+b)^2}\left(\frac{\pi h(a - h\cot\Phi)}{\sin\Phi} + (a+b)^2\right.$$

$$\left. - \pi\left(\frac{a}{2} - h\cot\Phi\right)^2\right)\cos\theta_{\mathrm{Y}} \qquad (3\text{-}7)$$

where F_{com} and F_{non} are the free energy states for drops in the initial composite and noncomposite states, respectively; L_0 is the drop base radius for drops both in the initial composite and noncomposite states; h is the pillar height; θ_{com} and θ_{non} are the apparent CAs for drops in the initial composite and noncomposite states, respectively. If the drop is receding from one initial composite state with contact line at the arbitrary position A to another initial composite state with contact line at the arbitrary position C, see Figure 3-3c, the FE difference can be expressed by eq 3-8:

$$\Delta F_{\mathrm{A}\to\mathrm{C}}/\gamma^{\mathrm{la}} = (F_{\mathrm{C}} - F_{\mathrm{A}})/\gamma^{\mathrm{la}}$$

$$= 2\pi\left(\frac{L_{\mathrm{C}}^2(1-\cos\theta_{\mathrm{C}})}{\sin^2\theta_{\mathrm{C}}} - \frac{L_{\mathrm{A}}^2(1-\cos\theta_{\mathrm{A}})}{\sin^2\theta_{\mathrm{A}}}\right)$$

$$+ \frac{\pi(L_{\mathrm{C}}^2 - L_{\mathrm{A}}^2)}{(a+b)^2}\left((a+b)^2 - \frac{\pi a^2}{4}\right) - \frac{\pi^2 a^2(L_{\mathrm{C}}^2 - L_{\mathrm{A}}^2)}{4(a+b)^2}\cos\theta_{\mathrm{Y}} \qquad (3\text{-}8)$$

where F_{A} and F_{C} are the free energy states for drops with the contact line at the

positions A and C, respectively; L_A and L_C are the drop base radius for drops with the contact line at the arbitrary positions A and C, respectively; θ_A and θ_C are the apparent CAs for drops with the contact line at the arbitrary positions A and C, respectively. If an arbitrary value of zero is given to the reference energy state (with drop base radius of the reference state 0), the energy states for all possible wetting cases on microstructured surfaces can be obtained.

Similarly, FE analysis could be applied to the drop wetting on microstructured surfaces constructed with two typical re-entrant microstructures, i.e., arrays of spherical microstructures with convex or concave side walls (Figure 3-3d). Free energy difference for drops with TPCL penetrating from an arbitrary positions A to B for microstructures with convex and concave side walls could be expressed by eqs 3-9 and 3-10, respectively:

$$\Delta F_{\mathrm{A}\to\mathrm{B}}/\gamma^{\mathrm{la}} = (F_{\mathrm{B}} - F_{\mathrm{A}})/\gamma^{\mathrm{la}} = 2\pi L_0^2\left(\frac{1-\cos\theta_{\mathrm{B}}}{\sin^2\theta_{\mathrm{B}}} - \frac{1-\cos\theta_{\mathrm{A}}}{\sin^2\theta_{\mathrm{A}}}\right) + \frac{\pi^2 L_0^2}{(a+b)^2}((r - H_B)^2 - (r - H_A)^2) - \frac{2(H_B-H_A)\pi^2 r L_0^2}{(a+b)^2}\cos\theta_{\mathrm{Y}} \qquad (3\text{-}9)$$

$$\Delta F_{\mathrm{A}\to\mathrm{B}}/\gamma^{\mathrm{la}} = (F_{\mathrm{B}} - F_{\mathrm{A}})/\gamma^{\mathrm{la}} = 2\pi L_0^2\left(\frac{1-\cos\theta_{\mathrm{B}}}{\sin^2\theta_{\mathrm{B}}} - \frac{1-\cos\theta_{\mathrm{A}}}{\sin^2\theta_{\mathrm{A}}}\right) + \frac{\pi^2 L_0^2}{(a+b)^2}\left[(\frac{a}{2} - \sqrt{r^2-(r-H_A)^2})^2 - (\frac{a}{2} - \sqrt{r^2-(r-H_B)^2})^2\right] - \frac{2\pi^2 L_0^2\cos\theta_{\mathrm{Y}}}{(a+b)^2}\int_{H_A}^{H_B}\left(\frac{a}{2} - \sqrt{r^2-(r-x)^2}\right)\sqrt{1+\frac{(r-x)^2}{r^2-(r-x)^2}}\,dx \qquad (3\text{-}10)$$

where F_A and F_B are the free energy states for drops at the positions A and B, respectively; H_A and H_B are the penetration heights for drops at the positions A

and B, respectively; L_0 is the drop base radius for drops both at positions A and B; θ_A and θ_B are the apparent CAs for the drops at the positions A and B, respectively; r is the curvature radius of the side wall for both typical re-entrant structures. Additionally, free energy difference for drops in initial composite and noncomposite states for both typical re-entrant structures could be expressed by eqs 3-11 and 3-12, respectively:

$$\Delta F_{\mathrm{com}\to\mathrm{non}}/\gamma^{\mathrm{la}} = \frac{F_{\mathrm{non}}-F_{\mathrm{com}}}{\gamma^{\mathrm{la}}} = 2\pi L_0^2\left(\frac{1-\cos\theta_{\mathrm{non}}}{\sin^2\theta_{\mathrm{non}}}-\frac{1-\cos\theta_{\mathrm{com}}}{\sin^2\theta_{\mathrm{com}}}\right)-\pi L_0^2-\left(\pi L_0^2+\frac{4\pi^2L_0^2r^2}{(a+b)^2}\right)\cos\theta_{\mathrm{Y}} \qquad (3\text{-}11)$$

$$\Delta F_{\mathrm{com}\to\mathrm{non}}/\gamma^{\mathrm{la}} = \frac{F_{\mathrm{non}}-F_{\mathrm{com}}}{\gamma^{\mathrm{la}}} = 2\pi L_0^2\left(\frac{1-\cos\theta_{\mathrm{non}}}{\sin^2\theta_{\mathrm{non}}}-\frac{1-\cos\theta_{\mathrm{com}}}{\sin^2\theta_{\mathrm{com}}}\right)-\frac{\pi L_0^2}{(a+b)^2}\left[(a+b)^2-\frac{\pi a^2}{4}\right]-\frac{2\pi^2L_0^2\cos\theta_{\mathrm{Y}}}{(a+b)^2}\int_0^h\left(\frac{a}{2}-\sqrt{r^2-(r-x)^2}\right)\sqrt{1+\frac{(r-x)^2}{r^2-(r-x)^2}}\,dx \qquad (3\text{-}12)$$

where h is the height of the microstructure, which equals to 2r.

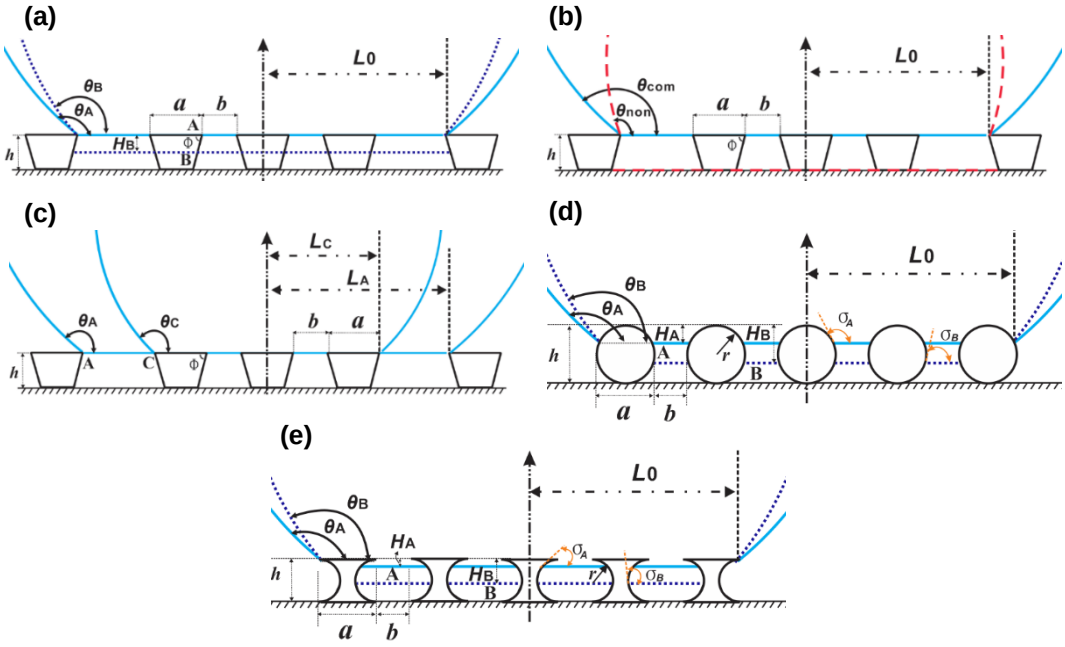

Figure 3-3. (a) Illustration of FE analysis for a drop at an arbitrary positions A and B, with liquid penetrating into the asperities. (b) Illustration of FE analysis for a drop at arbitrary initial composite and noncomposite states, with the drop contact line at the same place. (c) Illustration of FE analysis for a drop receding from one arbitrary initial composite state to another initial composite state. (d) and (e) Illustrations of FE analysis for drops penetrating from arbitrary positions A to B on arrays of microstructures with convex or concave side walls. Note that σ_A and σ_B represent the microscopic CA of water on the side wall of the microstructures when the drops are at positions A and B, respectively.

3.4 Results and Discussion

3.4.1 Free Energy Analysis for Straight-wall Microstructures

Figure 3-4 shows the normalized FE as a function of the apparent CA on straight-wall microstructures (edge angle, Φ, is 110° and 60° in Figure 3-4a and 3-

4b, respectively) for initial composite, noncomposite and intermediate composite states (the data is obtained from eqs 3-6, 3-7 and 3-8). All FE curves have an absolute minima. Contact angles corresponding to the minimum FE states (i.e., equilibrium CAs) for the initial composite and noncomposite states equal to the values calculated by eqs 3-1 and 3-2, respectively. One can also see that for both cases shown in Figure 3-4a ($\Phi = 110°$) and 3-4b ($\Phi = 60°$), the FE curve for the initial composite state is always above that of the noncomposite state at any apparent CA. For the case with edge angle $\Phi = 110°$ (Figure 3-4a), the FE curve for the intermediate composite state is higher than the noncomposite state but lower than the initial composite state. This implies that if a drop is placed on such microstructures ($\Phi = 110°$, $\theta_Y = 80°$), wetting transition from initial composite to noncomposite states will happen spontaneously. However, if the edge angle $\Phi = 60°$ (Figure 3-4b), the FE curve for the intermediate composite state will shift up to a position higher than that of both the initial composite and noncomposite states. Thus, an energy barrier is generated that prevents the wetting transition from initial composite to noncomposite states. In other words, initial composite state of the drop can exist metastably on such microstructures ($\Phi = 60°$, $\theta_Y = 80°$), even if the material constructed for the surface is hydrophilic ($\theta_Y = 80°$). This explains the experimental observations for the superhydrophobic wetting on rough surfaces constructed with hydrophilic materials.[10-13] Analysis on the transition FE barriers will be further discussed below.

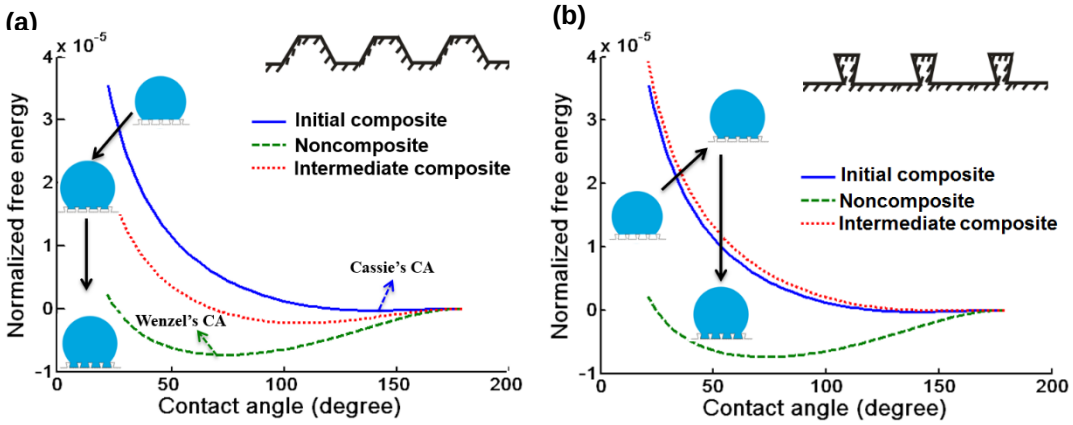

Figure 3-4. Normalized FE as a function of the apparent CA on straight-wall microstructures for initial composite, noncomposite, and intermediate composite states. (a) Edge angle Φ = 110°, Wenzel's CA = 74.2°, Cassie's CA = 140.3°. (b) Edge angle Φ = 60°, Wenzel's CA = 74.0°, Cassie's CA = 140.3°. Note that for both cases, $a=b=10\times10^{-6}$ m, $h=8\times10^{-6}$ m, drop volume=9.7×10^{-9} m^3, and θ_Y=80°.

3.4.2 Wetting Transition for Straight-wall Microstructures

Based on eqs 3-6 and 3-7, normalized FE as a function of the drop penetration depth (from the initial composite to noncomposite states) can be obtained for drops on straight-wall microstructures, see Figure 3-5. Three typical cases for wetting transition can be found. (1) For a hydrophobic material, e.g. θ_Y=100° and acute edge angle, Φ=60° (Figure 3-5a), the FE increases progressively when the liquid drop penetrates from the initial composite state to intermediate composite state. The FE will reach the maximum just before the drop touching the bottom of the microstructures and turning to noncomposite state. Note that the sudden drop of the FE state for forming the noncomposite state is

attributed to the formation of liquid-solid interface or to a result of disappearing the liquid-air and solid-air interfaces. Therefore, one can see that there is an energy barrier $FEB_{com\text{-}non}$ to be overcome for transition from composite to noncomposite states. For the opposite case of transition from noncomposite to composite states, an energy barrier $FEB_{non\text{-}com}$ exists; because $FEB_{non\text{-}com} > FEB_{com\text{-}non} > 0$, for this case, the initial composite state is a metastable wetting state.

(2) For a hydrophilic surface, e.g. θ_Y=80 ° and obtuse edge angle, e.g. Φ=100 ° (Figure 3-5b), the FE decreases progressively when the liquid drop penetrates from the initial composite state to intermediate composite state, and finally reaches the lowest energy state for noncomposite state. Since $FEB_{non\text{-}com} > 0 > FEB_{com\text{-}non}$, the energy barrier for transition from the initial composite to noncomposite states does not exist, and thus the transition would occur spontaneously.

(3) If the material is very hydrophobic, e.g. θ_Y=130 ° (note that liquid discussed here is not limited to water) and edge angle is acute, e.g. Φ=60 ° (Figure 3-5c), one can see that $FEB_{com\text{-}non} > FEB_{non\text{-}com} > 0$, and the composite state would become the most stable energy state for the liquid drop. Therefore, the transition from noncomposite to composite can happen with an external energy (e.g., mechanical vibration,[36] and thermal fluctuation[37]) even the drop is first in the noncomposite state (e.g., liquid condenses into the troughs of the microstructures).

Since superhydrophobicity refers to the composite state, $FEB_{com\text{-}non}$ is related to the stability of superhydrophobicity, and $FEB_{non\text{-}com}$ can be thought of the ability to recover superhydrophobicity. To obtain robust SHS, large $FEB_{com\text{-}non}$ and small $FEB_{non\text{-}com}$ are preferred.

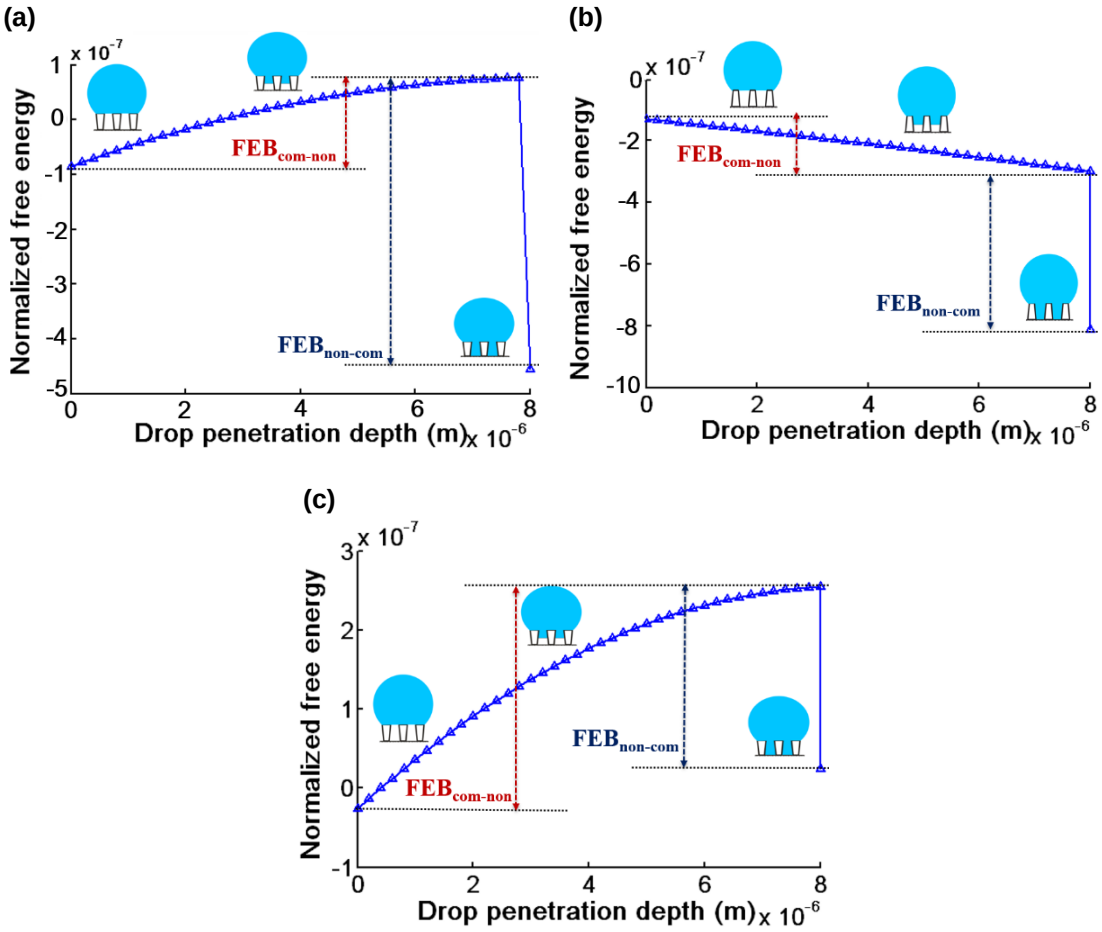

Figure 3-5. Normalized FE as a function of the drop penetration depth. Depending on the transition FE barriers, three types of possible wetting cases can been seen: (a) metastable composite case: θ_Y=100°, Φ=60°; (b) stable noncomposite case: θ_Y=80°, Φ=100°; (c) stable composite case: θ_Y=130°, Φ=60°. Note that $a=b=10\times10^{-6}$m, h=8×10^{-6}m, drop volume=9.7×10^{-9}m^3. Solid lines are to guide the eyes.

3.4.3 The Effect of Intrinsic CA

Figure 3-6a shows normalized FE as a function of the drop penetration depth with various intrinsic CAs ($a=b=10\times10^{-6}$m, $h=8\times10^{-6}$m, drop volume=9.7×10^{-9}m^3, and $\Phi=60°$). One can see that, as the intrinsic CA increases, the FE level for all the wetting states (i.e., initial composite, intermediate composite and noncomposite states) with different drop penetration depth would increase. Moreover, the normalized FE barrier curves (Figure 3-6b), shows that the $FEB_{com\text{-}non}$ increases while $FEB_{non\text{-}com}$ decreases as the intrinsic CA increases. Accordingly, large intrinsic CA is preferred for designing robust SHS, since it induces large $FEB_{com\text{-}non}$ and small $FEB_{non\text{-}com}$. It is worth pointing out that free energy barriers do not exist below the dashed line in Figure 3-6b, indicating FEB=0. Thus, transition energy barrier for preventing the drop transition from the initial composite to noncomposite states will exist only for cases with the intrinsic CA $\theta_Y > 60°$ (noted by the dotted line). Also, the curves of $FEB_{com\text{-}non}$ and $FEB_{non\text{-}com}$ intersect at the intrinsic CA of $125°$ (after which, $FEB_{com\text{-}non} > FEB_{non\text{-}com} > 0$), implying a stable composite state if $\theta_Y > 125°$. Since the maximum intrinsic CA of water on a solid material found today is around $120°$ (noted by the dash-dotted line), superhydrophobicity could be realized only in the region $60° < \theta_Y < 120°$ for the given case, see Figure 3-6b. However, plot in Figure 3-6b points to the immense benefits regarding the robustness of SHS that can be found with advance of material with water CA larger than $125°$.

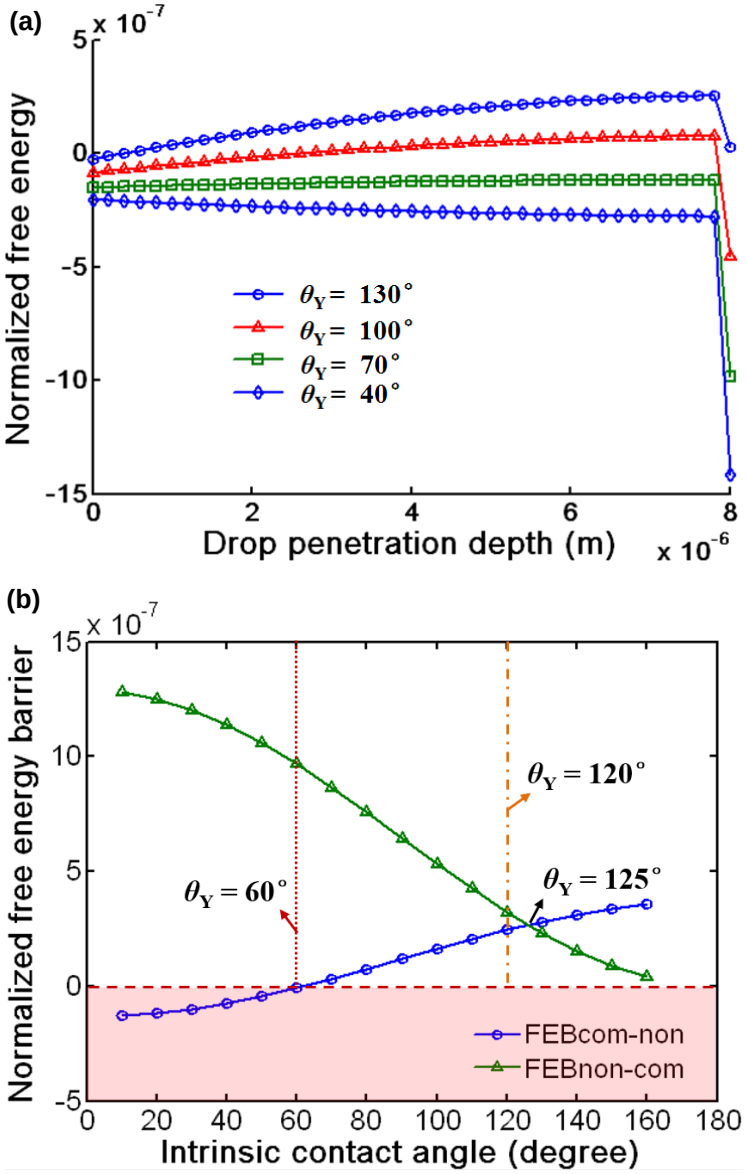

Figure 3-6. (a) Normalized FE as a function of the drop penetration depth with various intrinsic CAs. (b) Normalized FE barriers as a function of the intrinsic CA. Note that free energy barriers do not exist below the dashed line indicating FEB=0. $a=b=10\times10^{-6}$m; $h=8\times10^{-6}$m; drop volume=9.7×10^{-9}m^3; θ_Y=10° – 160 °; and Φ=60 °. Solid lines are to guide the eyes.

3.4.4 The Effect of Edge Angle

Figure 3-7a shows normalized FE as a function of the drop penetration depth with various edge angles ($a=b=10\times10^{-6}$m, $h=8\times10^{-6}$m, drop volume=9.7×10^{-9}m^3, and $\theta_Y=80°$). One can see that, as the edge angle decreases, the FE curves for the intermediate composite states with different drop penetration depth will shift up. However, the FE curve for the initial composite and noncomposite states will remain unchanged, leading to a constant value of energy difference between the two transition energy barriers (in this case, $FEB_{non\text{-}com}$ - $FEB_{com\text{-}non}$ = constant > 0, see Figure 3-7a). Figure 3-7b shows that the FE curve of $FEB_{non\text{-}com}$ is always above the FE curve of $FEB_{com\text{-}non}$ and they do not intersect. As a result, no stable composite state (i.e., $FEB_{com\text{-}non} > FEB_{non\text{-}com} > 0$) could exist for the case stated here, as $FEB_{com\text{-}non}$ is always smaller than $FEB_{non\text{-}com}$. Also, if the edge angle decreases, $FEB_{com\text{-}non}$ will change from a negative value (i.e., no energy barrier exists) to a positive value at edge angle of 80° (noted by the dotted line). This implies that metastable composite states could exist even for hydrophilic materials (e.g., $\theta_Y=80°$ for the microstructured surface presented here), when edge angle $\Phi < 80°$. On the other hand, small edge angle could lead to large $FEB_{non\text{-}com}$, indicating a more difficult process of wetting transition from noncomposite to composite states. As a result, though small edge angle is needed to achieve metastable composite states, drops would be difficult to recover from noncomposite to composite states once the drop transits into noncomposite state. This point is important for designing SHS.

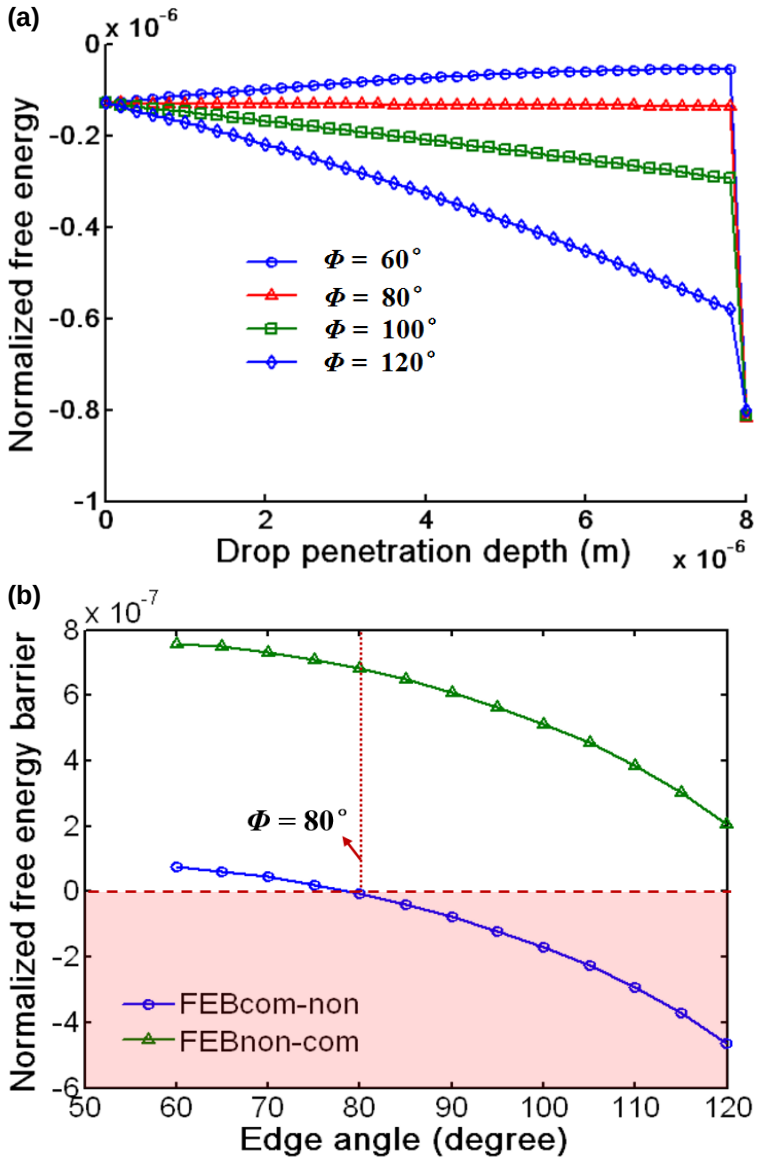

Figure 3-7. (a) Normalized FE as a function of the drop penetration depth with various edge angles Φ. (b) Normalized FE barriers as a function of the edge angle. Note that free energy barriers do not exist below the dashed line indicating FEB=0. $a=b=10\times10^{-6}$m, $h=8\times10^{-6}$m, drop volume=9.7×10^{-9}m^3, θ_Y=80 °, and Φ=60 °–120 °. Solid lines are to guide the eyes.

3.4.5 The Effect of Length Scale

It is known that the Cassie's fraction ($f = \pi a^2/(4\times(a+b)^2)$ for the pillar arrays, see Figure 3-2) determines the equilibrium CA of drops in the initial composite states. If the pillar spacing and width vary with the same length scale factor (here, the length scale factor is defined by $a=b=$*Length scale factor*$\times 10\times 10^{-6}$m), the Cassie's fraction as well as the equilibrium CA will remain unchanged. Thus, no influence of the length scale factor on wetting can be found just by looking at the classical wetting equations. However, our FE analysis shows that the wetting transition energy barriers will be significantly affected by the length scale factor.

Figure 3-8a shows the normalized FE as a function of the drop penetration depth with various length scale factors ($a=b=$*Length scale factor*$\times 10\times 10^{-6}$m, θ_Y=80°, and Φ=70°). One can see that as the length scale factor increases, the FE level of intermediate composite states decrease while the FE level of noncomposite state increases. This leads to the decrease of both $FEB_{com\text{-}non}$ and $FEB_{non\text{-}com}$ as the length scale factor increases. Figure 3-8b and 3-8c show the energy barrier curves of $FEB_{com\text{-}non}$ and $FEB_{non\text{-}com}$ (Φ=70°); the plots in this case show that the smaller the length scale factor, the more stable the drop will be in the initial composite states, and the more difficult for the drop to recover from the noncomposite to composite states once the drop transits into the noncomposite state. However, if the edge angle (Φ) changes, the trend of the energy curves of $FEB_{com\text{-}non}$ and $FEB_{non\text{-}com}$ will be different. For example, if the edge angle increases to a value larger than 80°, $FEB_{com\text{-}non}$ will become negative and thus the

energy barrier for preventing the transition from the initial composite to noncomposite states disappears; see Figure 3-8b for the shaded area below the dashed line indicating FEB=0. Moreover, one can see that the change of the energy barriers for both $FEB_{com\text{-}non}$ and $FEB_{non\text{-}com}$ will become more abrupt when the length scale factor is smaller than 3. This indicates that a more effective control of the transition energy barriers could be realized by designing the length scale factor at a value smaller than 3 (or pillar width and spacing < 30μm for the geometry studied here).

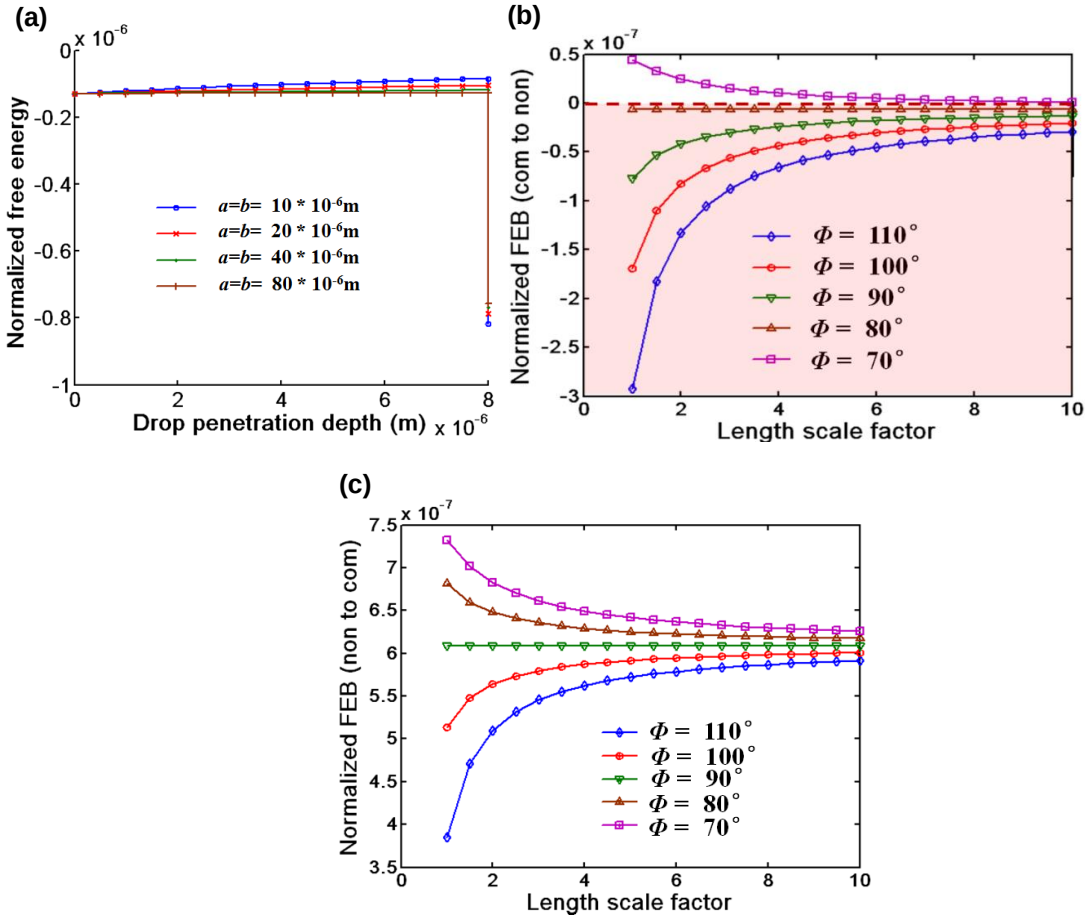

Figure 3-8. (a) Normalized FE as a function of the drop penetration depth with various length scale factor. *a=b=Length scale factor* × 10 × 10^{-6}m; h=8×10^{-6}m; drop volume=9.7×$10^{-9}$$m^3$; θ_Y=80°; and Φ=70°. (b) The FE curve of normalized $FEB_{com\text{-}non}$ as a function of the length scale factor. Note that free energy barriers do not exist below the dashed line indicating FEB=0. (c) The FE curve of normalized $FEB_{non\text{-}com}$ as a function of the length scale factor. *a=b=Length scale factor*×10×10^{-6}m; *h*=8×10^{-6}m; drop volume=9.7×$10^{-9}$$m^3$; θ_Y=80°; and Φ=70°–110°. Solid lines are to guide the eyes.

3.4.6 Wetting Map for Drops on Straight-wall Microstructures

On the basis of the above analysis, wetting maps for a drop on straight-wall microstructured surfaces can be obtained. Figure 3-9a gives the wetting map for a drop on microstructured surface with fixed pillar width and spacing ($a = b = 20\times10^{-6}$m). The dash-dotted line represents two extreme cases for the setting of edge angle ($\Phi_{max} = 141°$ and $\Phi_{min} = 39°$), due to the geometrical limitations (i.e. cross section size of the pillar). One can see that three wetting cases, i.e., noncomposite, metastable composite and stable composite states, can be found for microstructured surfaces with different combinations of edge angle and intrinsic CA. When the edge angle is set to be larger than the intrinsic CA, only noncomposite states can exist. When the edge angle is set to be smaller than the intrinsic CA, metastable composite state is mainly found at the range of $39° < \theta_Y < 130°$, while stable composite state is found at the range of $\theta_Y > 141°$. In the range of $130° < \theta_Y < 141°$, the decrease of edge angle leads to the change of wetting states from metastable to stable composite states. It is noted that the maximum intrinsic CA for water on solid material is found to be around 120° (noted by the dash-dotted line in Figure 3-9a), and thus stable composite state could hardly be reached for the given microstructured surfaces with fixed pillar width and spacing $a = b = 20\times10^{-6}$m.

Moreover, wetting map for a drop on straight-wall microstructured surface with various microgeometrical length scale factor is given in Figure 3-9b. Note that no matter how the microgeometrical length scale factor changes, the Cassie's

fraction *f* remains constant (= 0.2). One can see that for the edge angle larger than the intrinsic CA, only noncomposite state exists. For the edge angle smaller than the intrinsic CA, the boundary dividing the metastable and stable composite states will shift to the left (i.e., the range of smaller intrinsic CA) as the length scale factor decreases. Accordingly, stable composite state can be achieved with a smaller intrinsic CA if the length scale factor decreases. This is important because solid material with large intrinsic CA for water is below 120 °, as mentioned above. The wetting map provides a general understanding for choosing the microgeometrical parameters to obtain composite or superhydrophobic wetting states.

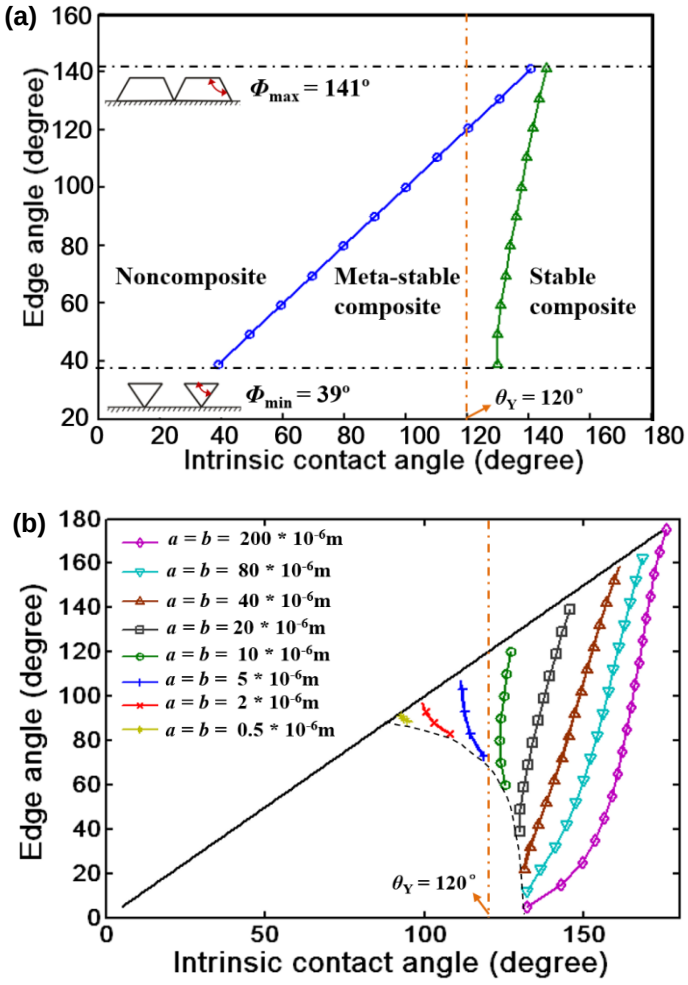

Figure 3-9. (a) Wetting map for drop on microstructured surface with fixed pillar width and spacing, f (Cassie's fraction) = 0.2; $a = b = 20\times10^{-6}$m; $h=8\times10^{-6}$m; and drop volume=9.7×10^{-9}m^3. Note that the d line represents the two extreme cases for the setting of edge angle (Φ_{max} = 141 °and Φ_{min} = 39 °), due to the geometrical limits. (b) Wetting map for drop on microstructured surface with various microgeometrical length scale factor, f (Cassie's fraction) = 0.2; $a = b$ = *Length scale factor* $\times10\times10^{-6}$m; $h = 8\times10^{-6}$m; and drop volume = 9.7×10^{-9}m^3. Solid lines are to guide the eyes.

3.4.7 FE Analysis on Microstructures with Convex Side Wall: Arrays of Spherical Microstructures

Figure 3-10a shows the normalized FE curve as a function of the drop penetration depth for the microstructures of convex side wall ($a = b = 10\times10^{-6}$m; $2r = 10\times10^{-6}$m; drop volume = 9.7×10^{-9}m^3; and $\theta_Y = 90°$). One can see that unlike the FE curves for the drop wetting on pillars with straight side wall (for which no minimum FE state is observed at the side wall of the pillar), the free energy shows a concave/bowl-shaped curve before TPCL touches the bottom of the microstructures. As a result, the drop first, in initial composite state, will penetrate into the microstructures spontaneously, and then stay metastably (relative to the most stable state for the noncomposite state, since $FEB_{non\text{-}com} > FEB_{com\text{-}non} > 0$) in an intermediate composite state at a certain penetration height. The penetration height of the drop corresponding to the metastable state is found to be 5 μm for the case illustrated, which is equal to the radius of the spherical microstructure. Thus, the microscopic CA (σ, see Figure 3-3) for the drop at the metastable state could be calculated to as 90°, which equals to the intrinsic CA $\theta_Y = 90°$. Similarly, if θ_Y is set to be 60°, the microscopic CA (σ) for the drop at the metastable state is calculated as 60°(see Appendix C for further details). It is found that the smaller the intrinsic CA, the larger the penetration height for the metastable intermediate composite state will be.

3.4.8 Transition Energy Barrier Analysis on Microstructures with Concave Side Wall

Figure 3-10b shows the normalized FE curve as a function of the drop penetration depth for the microstructures of concave side wall ($a = b = 10 \times 10^{-6}$ m; $2r = 5 \times 10^{-6}$ m; drop volume = 9.7×10^{-9} m^3; and $\theta_Y = 90$°). One can see that the FE curve shows convex shape and one maximum FE state appears at the intermediate composite state. This indicates that the initial composite state will be the metastable state, relative to the most stable state for the noncomposite state ($FEB_{non\text{-}com} > FEB_{com\text{-}non} > 0$). In particular, the penetration height of the drop corresponding to the maximum FE state is 2.5 μm, which equals to the radius of the concave curvature of the sidewall. Thus, the microscopic CA (σ) for the drop at the maximum FE state could be calculated to be 90 º (which equals to the intrinsic CA θ_Y=90°). Similarly, if θ_Y is set to be 60°, the penetration height corresponding to the maximum FE state is 1.25μm, and the microscopic CA (σ) is calculated as 60 º(see Appendix C for further details).

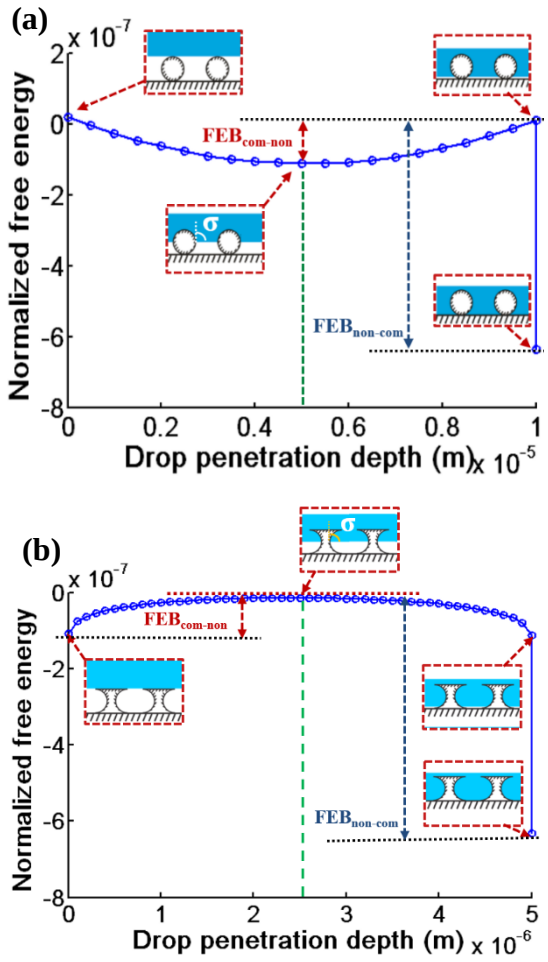

Figure 3-10. Normalized FE curves as a function of the drop penetration depth. (a) For the microstructures of convex side wall ($a = b = 10\times10^{-6}$m; $2r = 10\times10^{-6}$m; drop volume = 9.7×10^{-9}m^3; and $\theta_Y = 90°$); the microscopic CA (σ) for the drop at metastable state is 90 °, which equals to the intrinsic CA θ_Y=90 °. (b) For the microstructures of concave side wall ($a = b = 10\times10^{-6}$m; $2r = 5\times10^{-6}$m; drop volume = 9.7×10^{-9}m^3; and $\theta_Y = 90°$); the microscopic CA (σ) for the drop at the maximum FE state is 90 °, which equals to the intrinsic CA $\theta_Y = 90°$. Solid lines are to guide the eyes.

3.5 Conclusions

A 3-D thermodynamic FE model was developed to study the underlying mechanisms for stability, metastability or instability of noncomposite, initial composite and intermediate composite states. By comparing FE levels for drop wetting with different penetration height, fundamental effects responsible for the wetting transition was understood. Transition energy barriers $FEB_{com\text{-}non}$ and $FEB_{non\text{-}com}$ responsible for transitions from composite to noncomposite states and from noncomposite to composite states was found. Preferred wetting states was determined for a given microstructured surface by comparing the two transition energy barriers. Several important effects of surface parameters on the wetting property was discussed, i.e., the intrinsic CA, edge angle and length scale factor. For example, the increase of intrinsic CA could lead to the increase of $FEB_{com\text{-}non}$ and the decrease of $FEB_{non\text{-}com}$; the decrease of edge angle could lead to the increase of both $FEB_{com\text{-}non}$ and $FEB_{non\text{-}com}$. Moreover, the effect of length scale factor is dependent on the relationship of edge angle and intrinsic CA, and thus a wetting map is given in terms of the two parameters. From the wetting map, a safe region (stable or metastable composite states) can be decided for designing microstructures for keeping drops in superhydrophobic states. In addition, FE analysis for arrays of the two typical re-entrant structures (microstructures of convex and concave side wall) has revealed a minimum FE state at the intermediate composite state for microstructures of convex side wall; and a maximum FE state at the intermediate composite states for microstructures of

convex side wall. The results provide a framework for thinking about designing microstructured surfaces with superhydrophobic properties.

References

(1) Nishimoto, S.; Bhushan, B. *Rsc Advances* **2013,** *3*, 671-690.

(2) Zhao, H.; Law, K. Y.; Sambhy, V. *Langmuir* **2011,** *27*, 5927-35.

(3) Onda, T.; Shibuichi, S.; Satoh, N.; Tsujii, K. *Langmuir* **1996,** *12*, 2125-2127.

(4) Shibuichi, S.; Onda, T.; Satoh, N.; Tsujii, K. *J. Phys. Chem.* **1996,** *100*, 19512-19517.

(5) Cassie, A. B. D.; Baxter, S. *Trans. Faraday Soc.* **1944,** *40*, 546-551.

(6) Wenzel, R. N. *J. Ind. Eng. Chem.* **1936,** *28*, 988-994.

(7) Milne, A. J. B.; Amirfazli, A. *Adv. Colloid Interface Sci.* **2012,** *170*, 48-55.

(8) Bico, J.; Thiele, U.; Quere, D. *Colloids Surf., A* **2002,** *206*, 41-46.

(9) Nishino, T.; Meguro, M.; Nakamae, K.; Matsushita, M.; Ueda, Y. *Langmuir* **1999,** *15*, 4321-4323.

(10) Liu, J.-L.; Feng, X.-Q.; Wang, G.; Yu, S.-W. *J. Phys. Condens. Matter* **2007,** *19*, 356002/1-356002/12.

(11) Ma, Y.; Cao, X.; Feng, X.; Ma, Y.; Zou, H. *Polymer* **2007,** *48*, 7455-7460.

(12) Karlsson, M.; Forsberg, P.; Nikolajeff, F. *Langmuir* **2009**.

(13) Wang, J. D.; Liu, F. B.; Chen, H. S.; Chen, D. R. *Appl. Phys. Lett.* **2009,** *95*, 084104.

(14) Ahuja, A.; Taylor, J. A.; Lifton, V.; Sidorenko, A. A.; Salamon, T. R.; Lobaton, E. J.; Kolodner, P.; Krupenkin, T. N. *Langmuir* **2008,** *24*, 9-14.

(15) Marmur, A. *Langmuir* **2008,** *24*, 7573-7579.

(16) Tuteja, A.; Choi, W.; McKinley, G. H.; Cohen, R. E.; Rubner, M. F. *MRS Bull.* **2008,** *33*, 752-758.

(17) Li, W.; Amirfazli, A. *Adv. Colloid Interface Sci.* **2007,** *132*, 51-68.

(18) Patankar, N. A. *Langmuir* **2003,** *19*, 1249-1253.

(19) Patankar, N. A. *Langmuir* **2004,** *20*, 7097-7102.

(20) Marmur, A. *Langmuir* **2003,** *19*, 8343-8348.

(21) Marmur, A. *Langmuir* **2004,** *20*, 3517-3519.

(22) Barbieri, L.; Wagner, E.; Hoffmann, P. *Langmuir* **2007,** *23*, 1723-1734.

(23) Whyman, G.; Bormashenko, E. *Langmuir* **2011,** *27*, 8171-6.

(24) Bormashenko, E.; Musin, A.; Whyman, G.; Zinigrad, M. *Langmuir* **2012,** *28*, 3460-3464.

(25) Chen, Y.; He, B.; Lee, J.; Patankar, N. A. *J. Colloid Interface Sci.* **2005,** *281*, 458-464.

(26) Jansen, H. P.; Bliznyuk, O.; Kooij, E. S.; Poelsema, B.; Zandvliet, H. J. W. *Langmuir* **2011**.

(27) Bormashenko, E.; Bormashenko, Y.; Stein, T.; Whyman, G.; Bormashenko, E. *J. Colloid Interface Sci.* **2007,** *311*, 212-216.

(28) Choi, W.; Tuteja, A.; Chhatre, S.; Mabry, J. M.; Cohen, R. E.; McKinley, G. H. *Adv. Mater.* **2009,** *21*, 2190-2195.

(29) Koch, K.; Bhushan, B.; Barthlott, W. *Prog. Mater. Sci.* **2009,** *54*, 137-178.

(30) Dorrer, C.; Ruhe, J. *Langmuir* **2007,** *23*, 3820-3824.

(31) Krupenkin, T. N.; Taylor, J. A.; Wang, E. N.; Kolodner, P.; Hodes, M.; Salamon, T. R. *Langmuir* **2007,** *23*, 9128-9133.

(32) Boreyko, J. B.; Chen, C. H. *Phys. Rev. Lett.* **2009,** *103*.

(33) Dorrer, C.; Ruehe, J. *Soft Matter* **2009,** *5*, 51-61.

(34) Koishi, T.; Yasuoka, K.; Fujikawa, S.; Ebisuzaki, T.; Zeng, X. C. *Proc. Natl. Acad. Sci. U. S. A.* **2009,** *106*, 8435-8440.

(35) Verho, T.; Korhonen, J. T.; Sainiemi, L.; Jokinen, V.; Bower, C.; Franze, K.; Franssila, S.; Andrew, P.; Ikkala, O.; Ras, R. H. A. *Proc. Natl. Acad. Sci. U. S. A.* **2012,** *109*, 10210-10213.

(36) Decker, E. L.; Frank, B.; Suo, Y.; Garoff, S. *Colloid Surface. A* **1999,** *156*, 177-189.

(37) Kong, B.; Yang, X. *Langmuir* **2006,** *22*, 2065-2073.

Chapter 4 - Understanding the Anti-icing Behavior of Superhydrophobic Surfaces[3]

4.1 Introduction

Icing (frosting or water drop freezing) at cold surfaces can cause many problems for aircrafts[1] or wind turbines,[2] telecommunication equipment,[3] high-voltage power transmission,[4] etc. Most efforts proposed for solving the icing problems are active techniques (i.e., require external supply of thermal or mechanical energy) having high costs.[5] Inspired by nature,[6] novel materials, such as superhydrophobic surfaces (SHS), are suggested for their promise to have either passive anti-icing properties, or to reduce energy needed for active de-icing systems.[7-10] With a combination of surface chemical and roughness modifications, a water drop on SHS shows a large contact angle (CA), and a small contact angle hysteresis (CAH), i.e. <15 °. Thus, SHS are well-known for their excellent water-shedding and self-cleaning properties. However, the anti-icing properties of the superhydrophobic materials (including delayed frosting,[11-14] ice-adhesion reduction,[7, 15] snow-adhesion reduction[16, 17] and delayed water drop freezing[8, 12, 18, 19]) are more complex to understand, due to various factors involved, e.g., surface chemistry, roughness and environmental condition (Figure 4-1). Attempts to

[3] This work has been accepted by *Surface Innovations* (DOI: 10.1680/si.13.00046)

understand the anti-icing properties of SHS to date are done on a one factor a time basis, which undermines possibility of controlling for other aforementioned factors. Therefore, the mechanisms behind the phenomena are still unclear and contradictory results can be found; though such new material seems very promising in anti-icing fields.

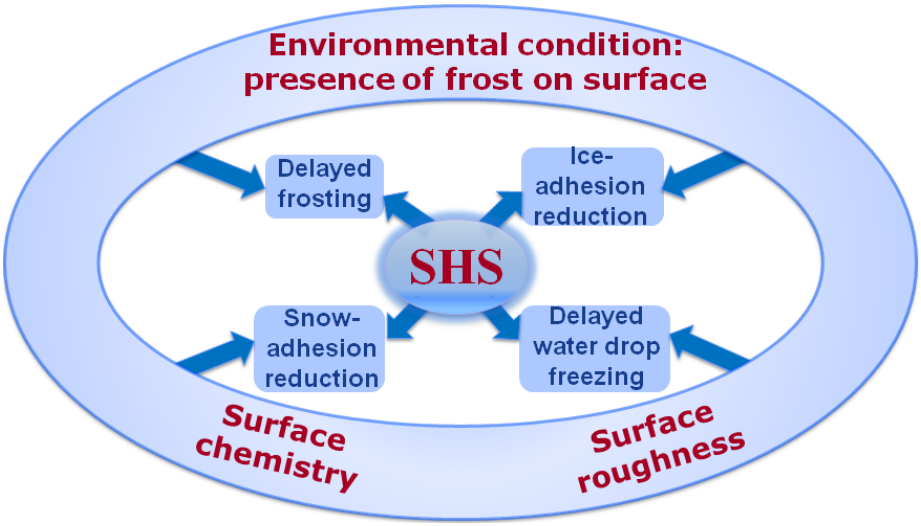

Figure 4-1. A diagram to show the factors affecting the anti-icing property of SHS.

Few studies were done systematically to ascertain the effectiveness of the SHS for the reported delayed frosting or water drop freezing, or ice adhesion, etc. For example, for delayed frosting, Liu et al.[12, 13] reported a retardation of frost formation on SHS compared to that on bare copper surface. However, due to the differences of both surface chemistry and roughness between SHS (roughened Si substrate coated by a hydrophobic film: CA = ~120 °) and bare copper surface (smooth hydrophilic surface: CA = 72 °), it is difficult to understand the mechanism responsible for the delayed frosting. As suggested by Liu et al.[20] and

Na et al.[21], frost formation can also be delayed on smooth hydrophobic surface compared to that on smooth hydrophilic surface. Therefore, the role of surface roughness cannot be separated from that of surface chemistry in the study of Liu et al..[12, 13] For the ice-adhesion reduction, Kulinich et al.[7, 15] indicated reduced ice adhesion strength on SHS with small CAH. However, they have not mentioned the relative humidity and thus disregarded the effect of frosting, as frosting condition is dependent on the environmental condition (e.g., relative humidity, air and surface temperatures).[20-22] Recently, Kulinich et al.[23, 24] and Varanasi et al.[9] demonstrated an increase of ice adhesion strength on SHS, if frost was formed on the tested surface. Regarding the drop freezing delay, Liu et al.[12] and Tourkine et al.[18] observed a delayed water drop freezing on SHS (rough surface with hydrophobic coating) compared to that on bare copper surface (smooth and hydrophilic surface). Similar to the problems mentioned above, the comparison made is not warranted as the effects of surface chemistry and roughness are mingled, disallowing a valid comparison. Moreover, the effect of frosting (i.e., environmental condition) on drop freezing was also ignored. Recently, Singh et al.[25] also observed a delayed freezing of water drop on SHS under a more controlled experimental condition, avoiding frost during the experiment. In particular, the delayed freezing of water drop on SHS was compared to that on smooth surface covered with the same material (i.e. the same surface chemistry). However, it is worth noting that both Tourkine et al.[18] and Singh et al.[25] have used tap water instead of deionized water. The effect of impurities from the tap water

may cover the effect of surface properties per se, and dramatically changes the freezing time and freezing temperature needed for water drops on the sample surfaces.

Additionally, a method to quantitatively characterize the water freezing points on different surfaces is missing. This is important for understanding the observed drop freezing delay on SHS, because it is not clear that whether the water drop freezing is delayed by depressing the freezing point or extending the freezing time due to the thermal insulation of air sub-layers.[18, 25] Wilson et al.[26] measured the freezing temperatures for water drops on hydrophilic, hydrophobic and superhydrophobic surfaces, using an automatic lag time apparatus (ALTA, the freezing was detected optically). Their results show that water drop freezing temperature on superhydrophobic surfaces have not been depressed as much as that on hydrophilic and hydrophobic surfaces. Moreover, the effect of surface heterogeneity, resulting from surface fabrication methods, is unclear as how it affects the observed delay of water drop freezing on SHS.

Differential scanning calorimetry (DSC) method has been widely applied to study the freezing and melting behaviors of water.[27-32] In this study, DSC technique was first used to accurately measure the freezing points of water on surfaces with different wettabilities, including superhydrophilic, hydrophilic, hydrophobic and superhydrophobic surfaces. Hence, the roles of surface chemistry and roughness on freezing delay can be determined. To understand the role that frost plays in drop freezing on cold surfaces, freezing of water drops on

various surfaces were also studied on a thermoelectric cooler under humid atmosphere.

4.2 Experimental Section

4.2.1 Preparation of Surfaces

The untreated aluminum sample vessels for DSC (pure aluminum >99%, TA Instruments – Waters L.L.C., see Appendix D. Figure D-1), cleaned thoroughly by ethanol and acetone, were hydrophilic. The roughened aluminum sample vessels were prepared by an acid etching method:[33] the aluminum vessels were etched in a 36% solution of hydrochloric acid in deionized water. The vessels were then removed from the acid after 3.5 minutes and quenched in a beaker of DI water. After rinsing in DI water and drying by a nitrogen stream, the rough vessels showed superhydrophilic behavior (observation of complete water drop spreading). In order to keep the same thermal contact property in tests, the outside surfaces of the vessels were protected by a thin polyolefin film (Parafilm M®). Furthermore, to obtain vessels with hydrophobic and superhydrophobic surfaces, the untreated and roughened aluminum vessels have been immersed into Teflon solution (15:1 v/v FC-75 (3-M)/Teflon AF (Dupont)) overnight. After drying in an oven (80℃) for at least 2 hours, the vessels showed hydrophobic and superhydrophobic (noted as SHS-Dip) behaviors, respectively. Also, superhydrophobic vessels can be obtained by spraying Teflon solution (5:1 v/v FC-75 (3-M)/Teflon AF (Dupont)) onto the roughened vessel surfaces with an

internal mixing air brush (noted as SHS-Spray). Different from the homogeneous coating of SHS-Dip, the coating of SHS-Spray is somewhat heterogeneous as evidenced by higher CAH (see the discussion in the main text). It should be noted that hydrophilic and superhydrophilic DSC sample vessels are both made of pure aluminum (>99%) with passivation layer of alumina on the exposed surface.

Similarly, for freezing tests on thermoelectric cooler, superhydrophilic, hydrophilic, hydrophobic, SHS-Dip and SHS-Spray surfaces were also fabricated on aluminum sheets ($2\times2cm^2$, 6061-T6, Aircraft Spruce and Specialty Co., Corona, CA) with the same procedure and precautions as DSC vessels.

4.2.2 Surface Characterization Methods

Water CAs were measured on a custom-built apparatus. DI water was added onto or removed from the sample surface by a clean syringe mounted on top of the surface. The syringe was driven by a motor at a rate of 0.5 μL/s. To calculate contact angles, drop images were analyzed by an image processing method.[34] Note that it is difficult to measure the CAs in the small DSC sample vessels. Therefore, CA values measured on the metal sheet have been used to characterize the wettability of different surfaces; this should be satisfactory as preparation methods were the same.

The microtexture of different sample surfaces was observed by a scanning electron microscope (SEM, LEO 1430); see Appendix D. Figures. D-2 and D-3. The roughness (R_a and R_q) was measured by a light confocal microscope (Axio

CSM 700, Carl Zeiss, Inc.). Additionally, the thickness of the dip-coated Teflon film was measured by a surface profiler (Alpha-Step IQ, KLA-Tencor, Inc.), which was ~71 ±7nm.

4.2.3 Experimental Procedure and Apparatus

DSC Q1000 (TA Instruments Co., temperature accuracy: 0.1 ℃) has been used to measure the freezing and melting points of water drop (6μL) in the sample vessels of different wettabilities. To the best of our knowledge, it is the first time that a DSC technique is applied to measure the freezing points of water drops on superhydrophobic surfaces. The temperature was set to drop from 10 ℃ to –30 ℃ at a very slow rate of 1 ℃/min, to minimize the thermal inertia. Then a constant temperature was held at –30 ℃ for 5 min, followed by a temperature increase 1 ℃/min to 10 ℃. The heat flow and temperature were recorded as a function of time. Typical DSC heating and cooling curves are given in Appendix D. Figure D-1b. The freezing and melting points were read from the exothermic peak and endothermic “dip”, respectively.

Freezing tests were also done using thermoelectric cooler in the laboratory condition (relative humidity: 40%; air temperature: 22 ℃). The surface temperature was decreased from 22 ℃ to –2.3 ℃, see Appendix D. Figure D-4b. The freezing processes were recorded by a digital camera (Nikon D3000).

4.3 Results and Discussion

4.3.1 Freezing Point Measurement by DSC

The surface wettabilities for different surfaces (i.e., superhydrophilic, hydrophilic, hydrophobic, SHS-Dip and SHS-Spray) were determined by measuring contact angle values, as shown in Table 4-1. It is worth noting that the freezing point measurement was conducted in a sealed vessel with small space (volume: ~20μL). When the temperature is constant, water condensation and evaporation will be in a dynamic equilibrium. As the temperature is decreased (in the freezing point measurement), the rate of water condensation exceeds the rate of evaporation. Water vapor in the closed space changes from vapor phase to liquid phase (above the freezing temperature of water) or to solid phase (below the freezing temperature of water). The surface of water drop can play a role as the nucleation site with very small Gibbs energy barrier (needed for the phase transition).[35] Thus, most of the water molecules in the vapor will condense onto the surface of water drop while only a small part of water molecules in the vapor will likely condense and freeze on the solid surface. As there are limited water molecules in the vapor within the small closed space, the freezing point measurements took place in a relatively dry environment.

On the other hand, capillary condensation may take place and influence the frosting and water drop freezing on certain textured surfaces even under a low relative humidity. Two phenomena are known to relate to this theory.[36-38] For

hydrophilic porous medium (the intrinsic contact angle of the material, θ_Y, < 90 °), fluid in the gas phase would condense into a liquid phase even the liquid phase is unstable on the flat surface (i.e., the vapor pressure is below the saturation vapor pressure of the liquid of the flat surface). For hydrophobic porous medium (θ_Y > 90 °), fluid in the liquid phase would transit to gas phase even if the gas phase is unstable on the flat surface (i.e., vapor pressure is above the saturation vapor pressure of the liquid of the flat surface). The latter case is also known as the "capillary evaporation". As a result, surfaces would tend to keep dry for textured surfaces covered with homogeneous hydrophobic coating (i.e., hydrophobic porous medium, e.g., SHS-Dip). However, for superhydrophilic and SHS-Spray surfaces (both own hydrophilic defects/pores, see the discussion in Section 3.1.3), capillary condensation may promote the formation of frost over the hydrophilic porous surface and then influence the water drop freezing behavior. It is noted that for freezing point measurement, water drops were pre-placed in the small sample pans. Since water drop will spread over superhydrophilic surfaces and fill the hydrophilic pores, capillary condensation is not involved for freezing point measurement on superhydrophilic surfaces. Thus, the only surface could be affected by capillary condensation in freezing point measurement is SHS-Spray (further discussion is given below).

Table 4-1. Contact angle for surfaces of different wettabilities. SD denotes the measurement standard deviation. Note that θ_{ad} and θ_{re} cannot be obtained for superhydrophilic surface, as water spreads on the surface to form a liquid film.

Surface type	θ_{ad} (°)	SD - θ_{ad}	θ_{re} (°)	SD - θ_{re}	CAH	SD - θ_{CAH}
Superhydrophilic	~0	–	~0	–	–	–
Hydrophilic	93.1	1.2	33.4	1.8	59.7	3
Hydrophobic	121.9	1.6	108.5	2.0	13.4	3.6
SHS-Dip	151.5	1.0	148.1	1.2	3.4	2.2
SHS-Spray	151.4	1.2	138.3	2.4	13.1	3.6

The freezing and melting points obtained by DSC are shown in Figure 4-2; the numerical values are given in Appendix D. Table D-1. Since the thermal diffusivity of air ($1.9 \times 10^{-5}\,m^2/s$) is in the same order of magnitude for aluminum ($8.4 \times 10^{-5}\,m^2/s$), there is a very rapid equilibration in the system compared to the slow heat exchange rate set by the 1 ℃/min temperature change. The maximum temperature difference between inside and outside of the sample pan caused by the thermal contact resistance during tests was determined through our analysis to be 0.14 ℃ (for the worst case: SHS-Dip with Teflon coating of rough surface). This is much smaller than the standard deviation of the freezing point measurement (see Appendix D. Table D-1). Therefore, the freezing temperature measurement has not been affected by the thermal contact resistance.

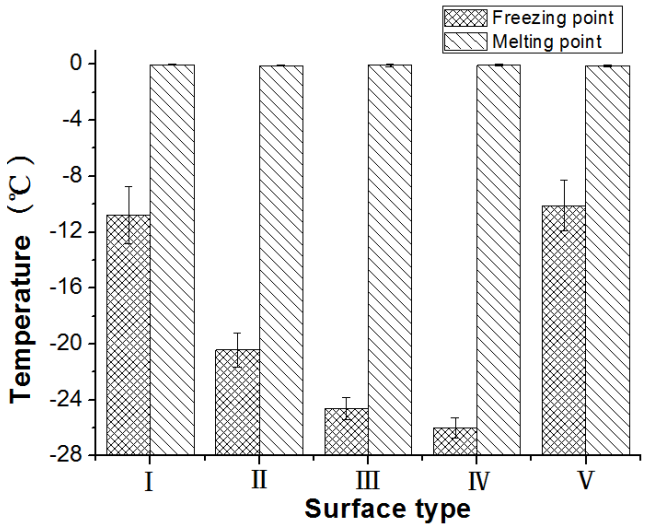

Figure 4-2. Freezing and melting points for different surfaces. I, Superhydrophilic surface; II, Hydrophilic surface; III, Hydrophobic surface; IV, SHS-Dip surface; V, SHS-Spray surface. The error bars indicate standard deviations based on five measurements from five sample surfaces. The numerical values for freezing and melting points are given in Appendix D. Table D-1.

From Figure 4-2, one can see that the melting points for different surfaces are all 0 ℃. However, the freezing points of water drop on different surfaces vary from –8 ℃ to –27 ℃. Normally, pure water freezes at the temperature of 0 ℃ (i.e., the so-called equilibrium freezing point), but it can also be supercooled to a point below 0 ℃, which is known as "kinetic freezing point" or "supercooling point".[32] The kinetic freezing point is the temperature at which spontaneous nucleation (i.e., homogeneous and heterogeneous ice nucleation) occurs. Note that the "freezing point" stated below refers to kinetic freezing point. A homogeneous ice nucleation process is hardly observed even under a controlled laboratory condition (the freezing point is believed to be lower than –39 ℃).[39] As water is usually in contact with an external surface that serves as nucleation site, heterogeneous ice

nucleation is more common and energetically favored. Considering the range of freezing points obtained by DSC, the mechanism for heterogeneous ice nucleation should be considered to explain the results.

4.3.1.1 Effect of Surface Chemistry

Because the thickness of the coated Teflon film is small (71±7nm), no significant difference of roughness was observed between hydrophilic and hydrophobic surfaces, as well as between superhydrophilic and SHS-Dip surfaces, see Table 4-2. Note that all the differences reported in this study have been statistically confirmed by student's t-test. Thus, the difference of water drop freezing points between hydrophilic and hydrophobic surfaces (also between superhydrophilic and SHS-Dip surfaces) can be attributed to the difference of surface chemistry. As shown in Figure 4-2, the freezing point of water drop on hydrophobic surface (–24.6 ℃ ± 0.8 ℃) is lower than that on hydrophilic surface (–20.4 ℃ ± 1.2 ℃), and the freezing point of water drop on SHS-Dip surface (–26.0 ℃ ± 0.7 ℃) is notably lower than that on the superhydrophilic surface (–10.8 ℃ ± 2.1 ℃). Hence, for the same surface roughness, a low energy surface (e.g., hydrophobic surface) can delay freezing compared to a high energy surface (e.g., hydrophilic surface). This is due to the Gibbs free-energy barrier required for the formation of critical ice nucleus (for heterogeneous nucleation) on a hydrophobic surface would be greater than that on a hydrophilic surface.[32]

Table 4-2. The profile roughness parameters for DSC sample vessels of different wettabilities. Note that SD represents the standard deviation for measurements.

	Ra (micrometer)	SD-*Ra*	*Rq* (micrometer)	SD-*Rq*
Superhydrophilic	5.79	0.21	7.34	0.24
Hydrophilic	0.31	0.08	0.70	0.28
Hydrophobic	0.31	0.07	0.63	0.10
SHS-Dip	5.64	0.19	7.07	0.20
SHS-Spray	5.98	0.29	7.54	0.46

Moreover, it is noted that the effect of surface energy on water drop freezing delay for surfaces of high roughness (the water drop freezing point difference between SHS-Dip and superhydrophilic surfaces, $\Delta T = 15.2\,℃ \pm 2.8\,℃$) is more significant than that for surfaces of low roughness (the water drop freezing point difference between hydrophobic and hydrophilic surfaces, $\Delta T = 4.2\,℃ \pm 2.0\,℃$). This shows the combined effect of surface roughness and surface chemistry. Further discussion of the effect of roughness on freezing delay is given next.

4.3.1.2 Effect of Surface Roughness

Similarly, the difference of water drop freezing points between hydrophilic and superhydrophilic surfaces (also between hydrophobic and SHS-Dip surfaces) can be attributed to the difference of surface roughness, since surfaces have the same chemistry. Comparison of water drop freezing points between hydrophilic ($-20.4\,℃ \pm 1.2\,℃$) and superhydrophilic ($-10.8\,℃ \pm 2.1\,℃$) surfaces shows that

roughness (see Table 4-2) can greatly increase the freezing point of water drop. As a result, on hydrophilic material, low roughness is preferred for extending the freezing delay of water drop. This is compatible with a former study,[40] showing delayed freezing under a constant temperature, but not depressed freezing temperature as shown here. However, comparison of water drop freezing points between hydrophobic (–24.6 ℃ ± 0.8 ℃) and SHS-Dip (–26.0 ℃ ± 0.7 ℃) surfaces (both were coated by Teflon) shows that roughness can decrease the freezing point of water drop on hydrophobic material, which was not reported till now. The above results can be attributed to the change of contact area between water drop and solid. For hydrophilic material, roughness can increase the contact area (water drop penetrates into the roughness, i.e., the so-called Wenzel state); while for hydrophobic material, roughness can decrease the contact area (water drop sits on top of the microstructures, i.e., the so-called Cassie state). Larger contact area between liquid and solid may increase the probability for heterogeneous nucleation. Nevertheless, further study is needed to obtain a full knowledge of the effect of roughness on water drop freezing depression. For example, a series of dip-coated SHS with various roughness/solid-liquid area portions are needed to put into tests, in order to provide an instruction on the design of SHS for freezing-depression applications.

Also, it is noted that the effect of roughness on water drop freezing delay for surfaces of high wettability (the water drop freezing point difference between hydrophilic and superhydrophilic surfaces, ΔT = 9.6 ℃ ± 3.3 ℃) is more

significant than that for surfaces of low wettability (the water drop freezing point difference between hydrophobic and SHS-Dip surfaces, $\Delta T = 1.4\,℃ \pm 1.5\,℃$). As a result, the freezing point difference is always a combined effect of surface roughness and chemistry.

4.3.1.3 Effect of Heterogeneity of Surface Coating

The freezing point of water drops on SHS-Spray ($-10.1\,℃ \pm 1.8\,℃$) is much higher than that on SHS-Dip ($-26.0\,℃ \pm 0.7\,℃$), and is close to that on superhydrophilic ($-10.8\,℃ \pm 2.1\,℃$) surface. Note that there is no significant difference of roughness between SHS-Spray and SHS-Dip surfaces (see Table 4-2). Thus, the difference of freezing point between SHS-Spray and SHS-Dip can be related to the surface heterogeneity (see Appendix D. Figures. D-2 and D-3 for the SEM images of sample surfaces). This implies that there must be exposed rough hydrophilic defects/pores (i.e., rough aluminum parts without Teflon coating) on the surface of SHS-Spray. In particular, the increase of CAH for SHS-Spray ($13.1° \pm 3.6°$) compared to that for SHS-Dip ($3.4° \pm 2.2°$) also supports the idea of increased surface heterogeneity.[41] As a result, capillary condensation may cause water filling in the hydrophilic pores, making it be similar to drop freezing case on superhydrophilic surface (i.e., water also fills all the hydrophilic pores for superhydrophilic surface). Thus, the freezing point of water drop on SHS-Spray is close to that on superhydrophilic surface. In addition, because the inner of the

sample pan cannot be observed directly during tests, the significance of capillary condensation in freezing point measurement for SHS-Spray requires further study.

The results show that the preparation methods for SHS can significantly affect its anti-icing property. The anti-freezing property of SHS will be greatly compromised, if there are hydrophilic defects existing. This may provide an explanation for why different researchers have reported different anti-icing properties for SHS, which has resulted in a debate of the usefulness of SHS in anti-icing fields.[9, 23, 24, 40]

It is worth pointing out that results from our DSC tests have shown that the depression of freezing point for water drop on SHS-Dip is larger than that for hydrophilic/hydrophobic surfaces. This is different from the results of Wilson *et al.*,[26] who showed that no higher depression of freezing point shown for SHS. There might be several reasons. First, as mentioned by Wilson *et al.*,[26] their repeated freezing/thawing methods for water drop on one sample surface may lead to irreversible Cassie to Wenzel transition even in the first few thermal cycles, leading to the loss of superhydrophobicity. Second, though aluminum DSC pans have been used as sample vessels, the technique they used for detecting the freezing is by monitoring the light transmission, which is different from DSC method (i.e., calorimetric method). Thus, unlike to our consistent surface treatment on both sample pan and sample cover (both are made of aluminum and treated to be superhydrophobic, see the Experimental Section), they have to use cover slip to allow light to transmit through. It could be easy for water drop to

contact the cover slip with hydrophilic wettability if large water volume is applied, since water drop will show spherical shape on superhydrophobic surface. In fact, the drop height for drop volume of 10 μl (the drop volume used by Wilson *et al.*[26]) can be calculated to be 2.50 mm if the contact angle is 150 °(which is typical for SHS), while the height of the DSC sample pan is 2.57mm measured by us. This is the reason that drop volume of 6 μl is used in our experiments. In addition, the contact angles and roughness of different surfaces have not been given in their study,[26] which is important for characterizing the sample surfaces.

4.3.2 Freezing Tests on Thermoelectric Cooler

Another compounding factor is frosting, to understand this, freezing of water drops (6 μl) on various surfaces placed on a thermoelectric cooler in laboratory condition was studied (see Appendix D. Figure D-4; air temperature: 22 ℃; relative humidity: 40%). Different from the freezing tests using DSC, the relative humidity and air temperature far away from the cold surface remains unchanged (i.e., unlimited water molecules were provided for condensation). As a result, dew and frost would continuously form on cold surfaces, if the temperature is cooled below the dew point of air (i.e., 8.5 ℃ in case of this study). Since water spreads on the superhydrophilic surface to form a thin liquid film, drop freezing experiments are not possible. Drop freezing tests were done on hydrophilic, hydrophobic, SHS-Dip and SHS-Spray surfaces obtained by the same treatment for DSC vessels, see Figure 4-3. Similar to the cases shown in Table 4-2,

roughness of hydrophilic and hydrophobic surfaces, as well as roughness of SHS-Dip and SHS-Spray surfaces, is statistically the same (see Appendix D. Table D-2). Note that under dry environment, water drops on cold surfaces should be supercooled and would not freeze, if the temperature is above the freezing point. Since the lowest temperature on thermoelectric cooler (–2.3 ℃, see Appendix D. Figure D-4b) was set to be higher than the highest water drop freezing point observed in DSC measurements (–8 ℃), ice nucleation in water drop should not happen spontaneously. However, under humid atmosphere, frosting on cold surfaces will significantly change the drop freezing behavior, as will be shown below.

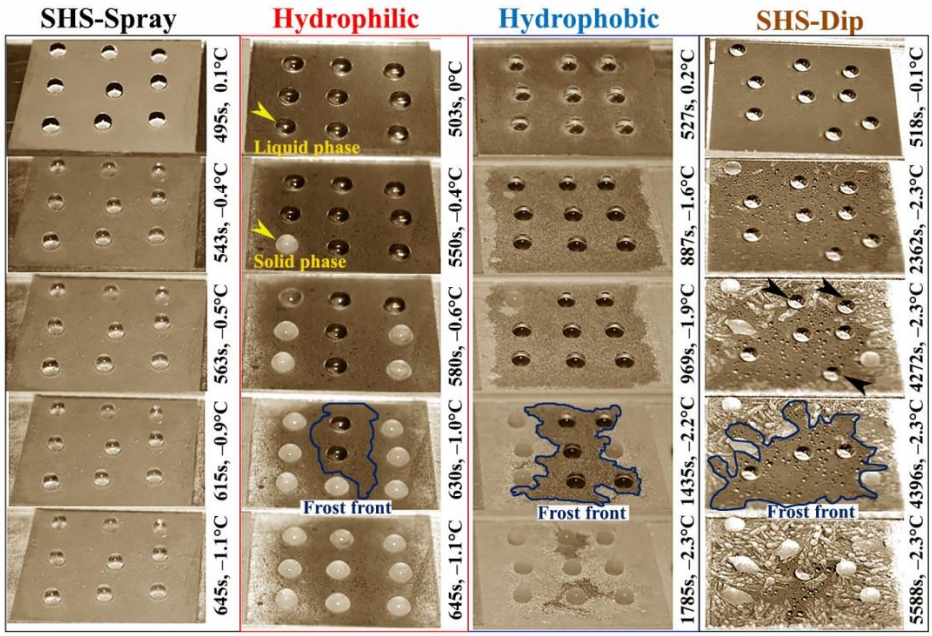

Figure 4-3. Typical stages during drop freezing tests for surfaces of various wettabilites on a thermoelectric cooler, under laboratory condition. The arrows on images of SHS-Dip indicate drops slipping onto the area covered by frost. Note that the size of sample surfaces is $2 \times 2 cm^2$.

4.3.2.1 Effect of Frosting on Water Drop Freezing

As seen in Figure 4-3, on hydrophilic surface, water drops would first be supercooled even for temperatures below 0 ℃. However, a thin film of frost would form and grow from outside of the sample (or the sample edge contacting the surface of the thermoelectric cooler), where nucleation sites with lower phase transition energy barrier may exist. As the frost grows and propagates towards the center of the sample surface, it would reach the supercooled water drops and act as ice nucleus for the phase transition (see Figure 4-3). However, on SHS-Spray surface, all the supercooled water drops change from liquid to solid almost at the same time in the temperature range –0.1 ℃ ~ –0.4 ℃. This is because water first condenses to rough hydrophilic defects/pores (due to the effect of capillary condensation) and then frost forms over the entire surface. Therefore, frost crystals would be generated over the whole surface and quickly grow to contact the supercooled water drops, causing phase transition for all the drops simultaneously.

Similar to the freezing phenomenon on hydrophilic surface, water drops on cold hydrophobic and SHS-Dip surfaces would be first supercooled and remain in liquid phase stably even for temperatures well below 0 ℃. As the frost crystals grow from the edge of the surface, it will touch the supercooled drops and prompt the phase transition (see Figure 4-3). The clear evidence provided here, gives material support to stipulations made earlier that small ice crystals on the cold surface could act as nuclei initiating drop freezing.[42] Interestingly, owing to the

low CAH on SHS-Dip, some supercooled drops would slip onto the area covered by frost (i.e., area with higher wettability) at the moment that frost crystals touch them (see the drops indicated by arrows in Figure 4-3), leaving no liquid residue on the sites. This implies that SHS-Dip still keeps superhydrophobic under a low temperature even below 0 ℃.

Moreover, speed of frost formation and growth is different on various surfaces, see Figure 4-4. On hydrophobic surface, frost propagation is faster than that on hydrophilic surface; SHS-Dip surface combined with low surface energy coating and high roughness shows the slowest frosting speed. Boreyko et al.[43] indicated that the jumping-drop effect on SHS (homogeneously coated) would allow the subcooled condensate to continuously jump off the surface before heterogeneous ice nucleation and minimize the success of ice bridging, leading to the lowest frosting speed. Since supercooled drops would not experience the phase transition unless the frost crystals touch the drops, we have shown that delay in freezing of drops is determined by the speed of frost propagation. As such the mechanism behind the freezing delay, when it is under humid atmosphere and temperature above the (kinetic) freezing point, is irrelevant to the freezing point depression as shown in the DSC measurements with dry environment. To our knowledge, the two different mechanisms responsible for the drop freezing delay on SHS have not been understood in previous studies, which often have led to confusion in freezing delay for SHS.

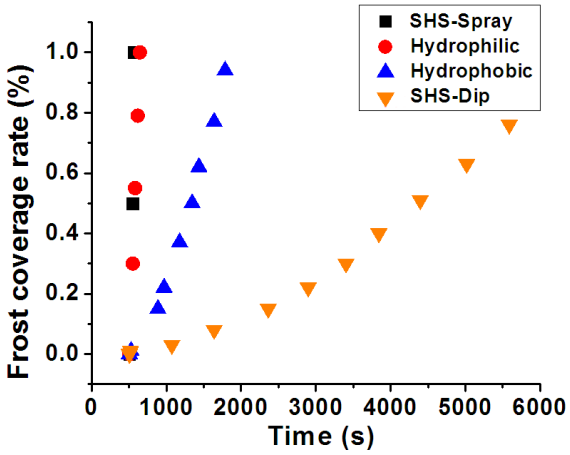

Figure 4-4. Frost coverage rate for drop freezing tests on various surfaces, under laboratory condition.

4.3.2.2 Frost Structure and Self-restoring Ability of Superhydrophobicity

A further important difference between hydrophilic, hydrophobic and superhydrophobic surfaces is the shape and consistency of ice growing from the edge of samples. Frost crystals become finer and more compact on cold surfaces with higher wettability, as seen in Figure 4-3 for superhydrophobic, hydrophobic and hydrophilic surfaces, respectively. To compare liquid-shedding abilities of different surfaces, the four surfaces were tilted by ~ 2° and the surface temperature was let to rise just above 0 ℃ at the end of freezing tests, as shown in Figure 4-5. Both frost and frozen water drops transform to liquid phase gradually as the temperature rises. The melted water drops on SHS-Spray and hydrophobic surfaces remained as individual water drops and stuck on the surfaces. The melted water drops on hydrophilic surface merged and formed a liquid film spreading on the surface. In contrast, due to the low CAH, the melting ice (i.e., a mixture of ice

and water) on SHS-Dip easily slipped off the surface when the temperature was just rise to 0 ℃. The results indicate SHS-Dip will keep superhydrophobic under a low temperature, even after the surface has experienced a freezing/thawing cycle and water vapor condenses onto the cold surface.

As stated by previous references,[44, 45] the surface wettability especially for SHS is strongly affected by the water condensation (at low temperature which is below the dew point), leading to an intrusion of micro-drops into the microstructures and a loss of superhydrophobicity. However, He et al.[46] found that their prepared SHS will keep superhydrophobic to condensed micro-drops at low temperature, showing effective resistance to the solidification of the condensed drops (i.e., frosting). The different results from references mentioned above indicate that the stability of superhydrophobicity is strongly dependent on the types of superhydrophobic surfaces prepared. This is consistent to our results; that is, SHS-Dip which could remain the superhydrophobicity under a low temperature is more effective for the frosting delay as compared to that for SHS-Spray, which would lose the superhydrophobicity.

In addition, the results show that ice can be easily removed from SHS if the surface is heated to be just above the melting point, avoiding a large consumption of energy for electrothermal or mechanical de-icing system.

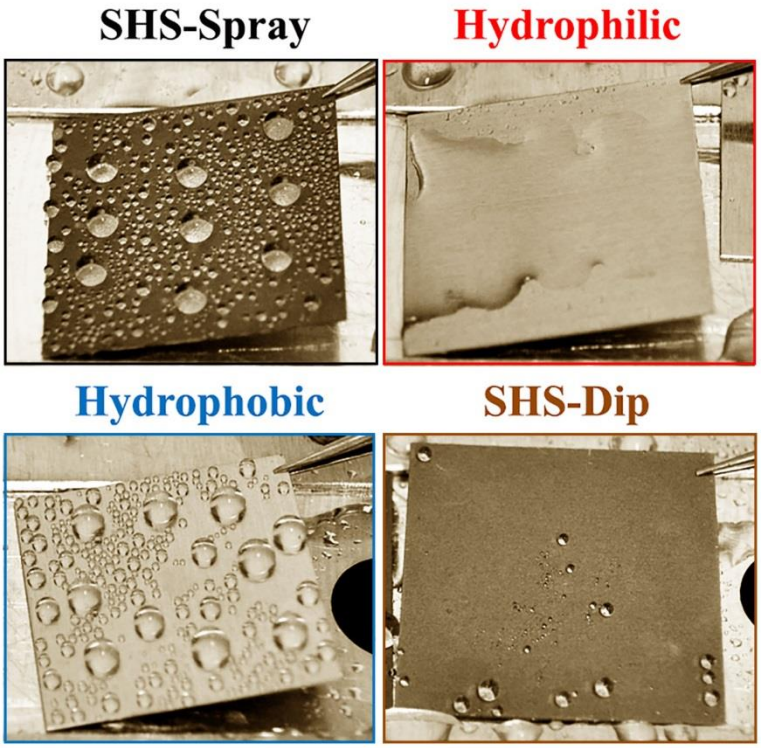

Figure 4-5. The ability for different surfaces to shed liquid after the temperature rises above 0 ℃ from freezing state. Note that the surfaces were tilted by ~2 °. Note that the size of sample surfaces is 2 ×2cm^2.

4.4 Conclusions

The present study was aimed at understanding the factors (i.e., surface chemistry, roughness and environmental condition) affecting the anti-icing behavior for SHS. Majority of work in literature discussing the effectiveness of superhydrophobic surface in anti-freezing has been clouded by confluence of different factors. To clear the confusion, first, DSC technique was used to measure the freezing points of water drops on different surfaces, in the condition that frost formation was limited (relatively dry environment). It was demonstrated

that for surfaces with the same roughness, surface chemical modification with low energy coating can promote the freezing delay and thus decrease the freezing point of water drop. For surfaces with the same wettability, roughness can significantly increase the water drop freezing point for hydrophilic material and mildly decrease the water drop freezing point for hydrophobic material. Though SHS-Dip shows the lowest freezing point of water drop, chemical heterogeneity (e.g., SHS-Spray) can greatly compromise the anti-freezing property for SHS. Second, freezing tests on thermoelectric cooler suggest that the drop freezing delay (humid atmosphere) is completely dependent on the presence and speed of frost formation and growth. If the temperature is below 0℃ and above the freezing point measured by DSC, water drops can be supercooled. Unless the frost contacts the water drops, they will remain in liquid phase. SHS (homogeneously coated) with low surface energy coating and high roughness will significantly lower the speed of frost growth; however, chemical heterogeneity on SHS will fail the delay of frost growth as well as the drop freezing delay.

This study provides new insights into the interplay of surface chemistry, surface roughness and environmental condition (air temperature, surface temperature, and relative humidity) on drop freezing behavior. The findings should have significant importance for the future design of anti-icing materials/systems. In particular, the recovery ability/robustness of superhydrophobicity is important for the anti-icing property. A design of superhydrophobic surfaces with high transition energy barrier from composite to

noncomposite states and low transition energy barrier from noncomposite to composite states (see Chapter 3) would benefit the application of superhydrophobic surfaces in low-temperature environment.

References

(1) Gent, R. W.; Dart, N. P.; Cansdale, J. T. *Philos. Trans. R. Soc. A-Math. Phys. Eng. Sci.* **2000,** *358*, 2873-2911.

(2) Homola, M. C.; Virk, M. S.; Nicklasson, P. J.; Sundsbo, P. A. *Wind Energy* **2012,** *15*, 379-389.

(3) Saito, H.; Takai, K.; Yamauchi, G. *JOCCA-Surf. Coat. Int.* **1997,** *80*, 168.

(4) Szilder, K.; Lozowski, E. P.; Reuter, G. *J. Offshore Mech. Arct. Eng. Trans. ASME* **2002,** *124*, 162-168.

(5) Laforte, J. L.; Allaire, M. A.; Laflamme, J. *Atmos. Res.* **1998,** *46*, 143-158.

(6) Koch, K.; Barthlott, W. Philos. Trans. R. Soc. A-Math. Phys. Eng. Sci. **2009,** 367, 1487-1509.

(7) Kulinich, S. A.; Farzaneh, M. *Langmuir* **2009,** *25*, 8854-8856.

(8) Cao, L.; Jones, A. K.; Sikka, V. K.; Wu, J.; Gao, D. *Langmuir* **2009,** *25*, 12444-12448.

(9) Varanasi, K. K.; Deng, T.; Smith, J. D.; Hsu, M.; Bhate, N. *Appl. Phys. Lett.* **2010,** *97*.

(10) Antonini, C.; Innocenti, M.; Horn, T.; Marengo, M.; Amirfazli, A. *Cold Reg. Sci. Tech.* **2011,** *67*, 58-67.

(11) Wang, H.; Tang, L. M.; Wu, X. M.; Dai, W. T.; Qiu, Y. P. *Appl. Surf. Sci.* **2007,** *253*, 8818-8824.

(12) Liu, Z.; Gou, Y.; Wang, J.; Cheng, S. *Int. J. Heat Mass Transfer* **2008,** *51*, 5975-5982.

(13) Gou, Y.; Liu, Z.; Wang, J.; Cheng, S. *Heat Transfer - Asian Res.* **2008,** *37*, 412-420.

(14) He, M.; Wang, J.; Li, H.; Jin, X.; Wang, J.; Liu, B.; Song, Y. *Soft Matter* **2010,** *6*, 2396-2399.

(15) Kulinich, S. A.; Farzaneh, M. *Appl. Surf. Sci.* **2009,** *255*, 8153-8157.

(16) Nakajima, A.; Hashimoto, K.; Watanabe, T. *Monatsh. Chem.* **2001,** *132*, 31-41.

(17) Kako, T.; Nakajima, A.; Irie, H.; Kato, Z.; Uematsu, K.; Watanabe, T.; Hashimoto, K. *J. Mater. Sci.* **2004,** *39*, 547-555.

(18) Tourkine, P.; Le Merrer, M.; Quere, D. *Langmuir* **2009,** *25*, 7214-7216.

(19) Mishchenko, L.; Hatton, B.; Bahadur, V.; Taylor, J. A.; Krupenkin, T.; Aizenberg, J. *ACS Nano* **2010,** *4*, 7699-7707.

(20) Liu, Z. L.; Zhang, X. H.; Wang, H. Y.; Meng, S.; Cheng, S. Y. *Exp. Therm. Fluid Sci.* **2007,** *31*, 789-794.

(21) Na, B.; Webb, R. L. *Int. J. Heat Mass Transfer* **2003,** *46*, 3797-3808.

(22) Wu, X. M.; Dal, W. T.; Xu, W. F.; Tang, L. M. *Exp. Therm. Fluid Sci.* **2007,** *31*, 1043-1048.

(23) Kulinich, S. A.; Farhadi, S.; Nose, K.; Du, X. W. *Langmuir* **2010,** *27*, 25-29.

(24) Farhadi, S.; Farzaneh, M.; Kulinich, S. A. *Appl. Surf. Sci.* **2011,** *257*, 6264-6269.

(25) Singh, D. P.; Singh, J. P. *Appl. Phys. Lett.* **2013,** *102*.

(26) Wilson, P. W.; Lu, W.; Xu, H.; Kim, P.; Kreder, M. J.; Alvarenga, J.; Aizenberg, J. *Physical Chemistry Chemical Physics* **2013,** *15*, 581-585.

(27) Jahnert, S.; Chavez, F. V.; Schaumann, G. E.; Schreiber, A.; Schonhoff, M.; Findenegg, G. H. *Phys. Chem. Chem. Phys.* **2008,** *10*, 6039-6051.

(28) Swiderski, A.; Wojtal, A.; Muras, P.; Mikulko, A.; Wrobel, S.; Koloczek, H. *J. Therm. Anal. Calorim.* **2006,** *83*, 631-636.

(29) Landry, M. R. *Thermochim. Acta* **2005,** *433*, 27-50.

(30) Schreiber, A.; Ketelsen, I.; Findenegg, G. H. *Phys. Chem. Chem. Phys.* **2001,** *3*, 1185-1195.

(31) Wilson, P. W.; Arthur, J. W.; Haymet, A. D. J. *Biophys. J.* **1999,** *77*, 2850-2855.

(32) Wilson, P. W.; Heneghan, A. F.; Haymet, A. D. J. *Cryobiology* **2003,** *46*, 88-98.

(33) Milne, A. J. B.; Amirfazli, A. *Langmuir* **2009,** *25*, 14155-14164.

(34) Chini, S. F.; Amirfazli, A. *Colloid Surf. A-Physicochem. Eng. Asp.* **2011,** *388*, 29-37.

(35) Beysens, D. *C. R. Phys.* **2006,** *7*, 1082-1100.

(36) Roth, R.; Kroll, K. M. *Journal of Physics-Condensed Matter* **2006,** *18*, 6517-6530.

(37) Saugey, A.; Bocquet, L.; Barrat, J. L. *J. Phys. Chem. B* **2005,** *109*, 6520-6526.

(38) Ball, P. *Nature* **2003,** *423*, 25-26.

(39) Franks, F.; Darlington, J.; Schenz, T.; Mathias, S. F.; Slade, L.; Levine, H. *Nature (London)* **1986,** *325*, 146-147.

(40) Jung, S.; Dorrestijn, M.; Raps, D.; Das, A.; Megaridis, C. M.; Poulikakos, D. *Langmuir* **2011,** *27*, 3059-3066.

(41) Li, D.; Neumann, A. W. *Colloid Polym. Sci.* **1992,** *270*, 498-504.

(42) Jung, S.; Tiwari, M. K.; Doan, N. V.; Poulikakos, D. *Nat. Commun.* **2012,** *3*, 615.

(43) Boreyko, J. B.; Collier, C. P. *ACS Nano* **2013,** *7*, 1618-1627.

(44) Cheng, Y.-T.; Rodak, D. E. *Appl. Phys. Lett.* **2005,** *86*, N.PAG.

(45) Wier, K. A.; McCarthy, T. J. *Langmuir* **2006,** *22*, 2433-2436.

(46) He, M.; Wang, J.; Li, H.; Song, Y. *Soft Matter* **2011,** *7*, 3993-4000.

Chapter 5 – Conclusions and Future Work

5.1 Conclusions

A systematic study has been carried out on understanding the role of surface microgeometries on wetting, aiming at providing instructions for designing robust superhydrophobic surfaces and its application in low-temperature environment. The main conclusions of this work are summarized as follows.

1. Four wetting cases for a drop on a single pillar with different edge angles have been determined by understanding the characteristics of FE plots. That is: case 1, a stable drop state on top of the pillar without risking the drop collapse onto the pillar sidewall; case 2, a metastable drop state on top of the pillar, which may experience a complete drop collapse and split if the FEB is overcome with the help of external FE provided from extra sources; case 3, an immediate drop collapse by spilling over the edge completely and split into two parts; case 4, a drop collapse by spilling over the edge while the TPCL can stay steadily at the position of sidewall.

2. A wetting map describing the four wetting cases for a drop on a single pillar can be obtained in terms of edge angle and intrinsic contact angle. An energetic framework to describe the functioning of the so-called “re-entrant” structures has been given. Results expanded the current understanding of Gibbs’ inequality condition.

3. For drop wetting on patterned surfaces with arrays of pillars (from upright frustum to inverted frustum geometries), two transition energy barriers $FEB_{com\text{-}non}$ and $FEB_{non\text{-}com}$ have been found to be responsible for transitions from composite to noncomposite states and from noncomposite to composite states, respectively.

4. Effects of various surface parameters, such as intrinsic contact angle, edge angle and length scale factor have been revealed. For example, the increase of intrinsic CA could lead to the increase of $FEB_{com\text{-}non}$ and the decrease of $FEB_{non\text{-}com}$; the decrease of edge angle could lead to the increase of both $FEB_{com\text{-}non}$ and $FEB_{non\text{-}com}$.

5. A wetting map for designing microstructures for holding drops in superhydrophobic surfaces is given in terms of edge angle and intrinsic CA.

6. FE analysis for arrays of two typical re-entrant structures (microstructures of convex and concave side wall) has revealed special FE configurations for drop penetration process. That is, a minimum FE state at one intermediate composite state for microstructures of convex side wall and a maximum FE state at one intermediate composite states for microstructures of convex side wall have been shown.

7. For application of superhydrophobic surfaces in low-temperature-condition field, it is shown that under relatively dry environment, the freezing delay

on cold surfaces is attributed to the water freezing point depression, which is determined by the combined effect of surface chemistry and roughness.

8. Also, drop freezing tests using a thermoelectric cooler under humid atmosphere showed that the freezing delay is dependent on the frosting, as well. Frost crystals growing on the cold surface will act as nucleus initiating drop freezing.

9. The recovery ability/robustness of superhydrophobicity is important for the anti-icing property. A design of superhydrophobic surfaces with high transition energy barrier from composite to noncomposite states and low transition energy barrier from noncomposite to composite states would benefit the application of superhydrophobic surfaces in low-temperature environment.

5.2 Future Work

Based on the work presented in this dissertation, a number projects can be taken up to extend the current research. For example, hierarchical structures were frequently observed from natural SHS,[1-3] and were successfully fabricated.[4-8] However, few studies have tried to understand the effect of secondary roughness on the transition FE barriers from the thermodynamic view. Thus, the following work could be done in the future.

5.2.1 Disordered secondary roughness

1. 3D thermodynamic modeling method could be applied to analyze the drop FE states on the dual roughness structures shown in Figure 5-1. Wenzel's roughness and Cassie's fraction factors would be used in the model for describing the secondary roughness, in order to avoid the complexity of the detailed configurations of the secondary roughness.

2. It is expected that different parts of the secondary roughness could play different roles in transition FE barriers. For example, the secondary roughness on the top of the microstructures will lift up FE curve, leading to an increase of FE states (as well as contact angle) for composite states; the secondary roughness at the sidewall of the microstructures may dramatically increase the transition FE barrier from composite to noncomposite; the secondary roughness at the bottom of the microstructures may dramatically decrease the transition FE barrier from noncomposite to composite;

3. The results may be applied to explain the different strategies in nature for distributing roughness at different levels on SHS,[9] leading to various wetting behavior. For instance, for lotus[10] and roses,[11] surfaces are both consisted by micro-scale bumps. However, drops are willing to roll off lotus but sticky on roses, while both keep large static contact angles. Microscopic images show that secondary nanoroughness exists at the bottom of first level microstructures on lotus, but not on roses; meanwhile, secondary nanoroughness exists on both tops of the first level microstructures for lotus and roses. The theory proposed above may explain this.

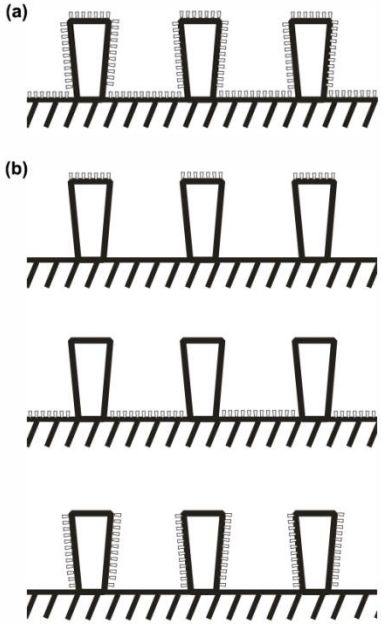

Figure 5-1. A schematic illustration for textured surfaces with disordered secondary roughness: (a) a microtextured surface fully covered by secondary roughness; (b) microtextured surfaces partially covered by secondary roughness.

5.2.2 Ordered secondary roughness

1. 3D thermodynamic modeling method could be applied to analyze the drop FE states on the two kinds of patterned pillars with ordered secondary roughness, see Figure 5-2. FE states for drops at all possible wetting states on the given microtextured surfaces could be obtained. Detailed transition FE barriers (from composite to noncomposite or noncomposite to composite) could be provided.

2. Pillars with various re-entrant structures on the side wall (Figure 5-2a) is considered, which is similar to the experimentally obtained structures.[12, 13] Such secondary structure is expected to initiate various meta-stable intermediate composite states. TPCL beneath the drop may be locked on the sidewall of the pillar, preventing further penetration. However, the transition FE barriers from noncomposite to composite states may also be large, preventing the drop from rebounding back to composite states.

3. Patterned pillars with parallel grooves on the side wall (Figure 5-2b) will be considered, which is expected to show no meta-stable intermediate composite states; meanwhile, the groove structures on the side wall may have increased the transition energy barrier (from composite to noncomposite states). Thus, drop rebound from intermediate to initial composite states should be easy. This might be the reason that grooved

structures at the secondary roughness are preferred for some robust SHS (e.g., mimic structures from water strider leg[14]).

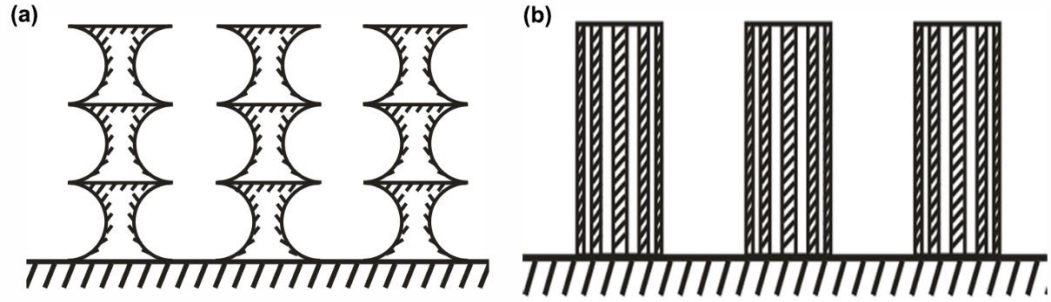

Figure 5-2. A schematic illustration for textured surfaces with ordered secondary roughness: (a) patterned pillars with various re-entrant structures on the side wall, initiating various meta-stable intermediate states; (b) patterned pillars with parallel grooves on the side wall, where exists no meta-stable intermediate states.

References

(1) Bhushan, B. *Philos. Trans. R. Soc. London, A* **2009**, 1445-1486.

(2) Koch, K.; Barthlott, W. Philos. Trans. R. Soc. A-Math. Phys. Eng. Sci. **2009,** 367, 1487-1509.

(3) Bixler, G. D.; Bhushan, B. Philosophical Transactions of the Royal Society a-Mathematical Physical and Engineering Sciences **2012,** 370, 2381-2417.

(4) Jung, Y. C.; Bhushan, B. *Langmuir* **2009,** *25*, 9208-9218.

(5) Gao, X.; Yao, X.; Jiang, L. *Langmuir* **2007,** *23*, 4886-4891.

(6) Liu, K.; Yao, X.; Jiang, L. *Chem. Soc. Rev.* **2010,** *39*, 3240-3255.

(7) Boreyko, J. B.; Baker, C. H.; Poley, C. R.; Chen, C.-H. *Langmuir* **2011**, null-null.

(8) Bhushan, B.; Nosonovsky, M. Philosophical Transactions of the Royal Society a-Mathematical Physical and Engineering Sciences **2010,** 368, 4713-4728.

(9) Koch, K.; Bohn, H. F.; Barthlott, W. *Langmuir* **2009,** *25*, 14116-20.

(10) Barthlott, W.; Neinhuis, C. *Planta* **1997,** *202*, 1-8.

(11) Bhushan, B.; Her, E. K. *Langmuir* **2010**.

(12) Zhao, H.; Law, K.-Y.; Sambhy, V. *Langmuir* **2011**, null-null.

(13) Ahuja, A.; Taylor, J. A.; Lifton, V.; Sidorenko, A. A.; Salamon, T. R.; Lobaton, E. J.; Kolodner, P.; Krupenkin, T. N. *Langmuir* **2008,** *24*, 9-14.

(14) Yao, X.; Chen, Q. W.; Xu, L.; Li, Q. K.; Song, Y. L.; Gao, X. F.; Quere, D.; Jiang, L. *Advanced Functional Materials* **2010,** *20,* 656-662.

Appendices

Appendix A[4]

A.1 Introduction

The wetting behavior of surfaces, the result of the interplay between liquid and surface chemistry and roughness, is such an influential area that much research has been devoted to in the past decades.[1, 2] Understanding and controlling the wetting phenomena are significant in both fundamental research and industrial applications. As is well known, the modification of surface chemistry is one of the most effective ways to control the wetting behavior of surfaces.[3, 4] However, such surface chemistry modification can have some limitations, e.g., the choice of chemical species and their biochemical compatibility.[5] The effect of surface roughness or its microgeometry on wetting has received much attention over the past.[6-13] Particularly, the advantage of flexible manipulation of surface microgeometries allows nature to develop various special wetting properties, e.g., the self-cleaning property[14, 15] of some plant's leaves[16-19] and animal's wings,[20, 21] the super-floating ability of water-strider,[22-24] the anti-fogging property of mosquito compound eyes,[25] the water-collection ability of spider silk[26] and desert beetles,[27-29] etc. Moreover, with the development of micro/nanofabrication

[4] This work has been submitted to *Interfacial Phenomena and Heat Transfer* （2014）

technologies, various surface microgeometries preparations have been proposed to control the surface wettability.[30, 31]

The apparent contact angle (CA, the angle at which a liquid/vapor interface meets a solid surface) on rough surfaces correlated with roughness (r) or solid-liquid contact area fraction (f_a) was well formulated more than 60 years ago,[32, 33] i.e., the classical Wenzel and Cassie equations. It has been widely used to characterize the surface drop repellency,[34] especially for superhydrophobic surfaces (SHS) studied in recent years.[14, 15] However, these equations maybe inadequate to comprehend another important SHS property, i.e., the drop mobility[34] related to contact angle hysteresis (CAH, the difference between advancing or maximum and receding or minimum contact angles), since r or f_a represents a composite measure of all surface texture parameters and the apparent CA obtained from Wenzel or Cassie equation only represents the equilibrium or minimum-energy state.[35-37] Thus it is insufficient to gain a complete understanding on the superhydrophobic wetting behavior. On different microtextured surfaces, even for the same r and f_a values, completely different drop mobility can be observed.[38, 39] Also, the validity of the Wenzel and Cassie equations has been intensively debated.[40-43] Different microgeometry distributions may affect the definition of r and f_a, resulting in a misuse of the Wenzel and Cassie equations to calculate the CA values.[44] Therefore, the role of surface microgeometry in wetting cannot be fully understood by r and f_a, and it is necessary to investigate the effect of other microgeometrical parameters that can

affect the wetting results.

One of the most important effects of microgeometries is the sharp-edge effect,[45-49] which is believed to be one of the main factors for affecting the contact angle hysteresis. Such effect can be responsible for the pinning of the drop contact line (DCL, along the drop perimeter) at an edge of a surface microstructure. Gibbs[50] first proposed the inequality condition for a liquid DCL at a sharp solid edge based on a geometrical treatment. Later, wetting behaviors related to pinning of DCL have been widely explained by Gibbs' principle.[51-54] In particular, recent researches[45, 55-59] demonstrated that by employing the re-entrant edge shapes, liquid could be inhibited from spilling over the edge and drops can be suspended on top of the microstructures. The result indicates that superhydrophobicity/superoleophobicity could be realized even for liquid with low surface tension. Nevertheless, the pinning of DCL at the edge of surface microgeometries for SHS is still not fully understood. For example, advancing and receding DCL may have a different pinning behavior at the edge, leading to different advancing and receding CAs as well as drop mobility. Further study of the pinning of DCL at a microgeometrical edge is required.

In addition to the edge effect, the different microgeometrical shape and length scale (i.e., different microgeometrical size) may also influence the wetting behavior particularly for SHS. Oner and McCarthy[38] studied the hydrophobicity of microtextured surfaces with posts of different sizes, shapes and separations. They claimed that the increase of post distance and the change of post shapes

(from square to indented square) may decrease the contact length and increase the tortuosity of DCL. This causes the increase of receding contact angles. However, they failed to keep the other surface parameters (e.g., the roughness or the Cassie's fraction) constant while the post shapes were changed, leading to a confusion of effects for different factors. Youngblood *et al.*[60] and Yoshimitsu *et al.*[61] have pointed out that size scale and microgeometrical shapes could seriously contort the shape of DCL on SHS, leading to different drop motion ability. Later, Dorrer *et al.*[39, 62] also discussed the influence of the distribution of the square posts on the DCL shape and then the contact angles. Though the above studies have attributed the effects of microgeometrical shape and length scale to the change the shape of the DCL, there is still a lack of clear explanations and systematical study.

In this report, patterned surfaces with different microgeometries, i.e., square, triangle and circle post arrays, have been fabricated by microfabrication techniques. With controlling the solid area fraction and microgeometrical length scale, various surface wetting behaviors have been investigated. Several important surface microgeometrical effects, e.g., length scale effect, edge and corner pinning effect, geometrical shape effect, direction-dependent effect, will be discussed. By applying some simplified models, mechanisms responsible for those effects can be understood.

A.2 Theoretical Basis

A.2.1 Equilibrium CAs

The thermodynamic equilibrium CA of a liquid drop on an ideal smooth solid surface can be predicted by Young's equation:

$$\gamma^{la}\cos\theta_Y = \gamma^{sa} - \gamma^{ls} \qquad \text{(A-1)}$$

where γ^{la} , γ^{sa} and γ^{ls} are interfacial tension at liquid-air, solid-air and liquid-solid interfaces, respectively. Classically, two wetting states may occur if a drop is deposited on a rough surface: the noncomposite, i.e., complete liquid penetration into the troughs of a rough surface; and the composite, i.e., entrapment of air in the troughs of a rough surface. The apparent equilibrium CA of the noncomposite is given by Wenzel's equation:

$$\cos\theta_W = r\cos\theta_Y \qquad \text{(A-2)}$$

where r is the roughness factor as the ratio between the actual surface area and the projected area for a wetted surface. On the other hand, the apparent equilibrium CA of the composite, θ_C , can be calculated using the Cassie's equation:

$$\cos\theta_C = f_1\cos\theta_1 + f_2\cos\theta_2 \qquad \text{(A-3)}$$

where f_1 and f_2 are the fractions of the solid-liquid and liquid-air interfaces with equilibrium contact angles θ_1 and θ_2, respectively. The contact angle of

liquid on solid-liquid contact part, θ_1 is equal to the Young's CA (θ_Y) and liquid-air contact part, θ_2 is equal to 180 ° (the CA for liquid with entrapped air), as such one has:

$$\cos\theta_C = f\cos\theta_Y - (1-f) \qquad \text{(A-4)}$$

where f is the solid-liquid contact fraction of the substrate.

Based on the debate of the validity of the Wenzel's and Cassie's equations,[40-43] McHale[41] and Nosonovsky[42] indicated that the Cassie equation can be generalized as:

$$\cos\theta_C = f_1(x,y)\cos\theta_1 + f_2(x,y)\cos\theta_2 \qquad \text{(A-5)}$$

The local Cassie's fractions, $f_1(x,y)$ and $f_2(x,y)$, of the two components that compose the heterogeneous surface should be taken as the functions of x and y in the region[42] (or neighborhood[41]) of the DCL.

Although very high roughness factor in Eq. (A-2) can induce a high apparent contact angle and thus high drop repellency, low drop mobility or high contact angle hysteresis has been observed and demonstrated for Wenzel's or noncomposite state. As a result, current superhydrophobic state is commonly referred to Cassie's or composite state, which will be the main subject discussed in this report.

A.2.2 Advancing and Receding CAs for Composite State

Drops on SHS may be prevented from reaching the free energy minimum

states described by Eqs. (A-2) and (A-4) by multiple free energy barriers generated by the roughness.[36] Consequently, contact angle hysteresis or advancing and receding CAs arises. Up to now, a quantitative prediction of advancing and receding CAs for composite state still keeps confusing.[37]

The basis of the Cassie equation is the surface energy minimization principle. From a different perspective, nonetheless, the apparent equilibrium CA from Cassie equation Eq. (A-3) may also be viewed as the result of averaging the local equilibrium contact angle at the drop contact line by its length.[42] Similarly, the apparent receding and advancing CAs can also be considered to be the result of averaging the local receding and advancing CAs along the drop contact line, which is given in a form analogous to Eq. (A-3) as:

$$\cos\theta_r = f_{real}\cos\theta_{s,rec} + (1 - f_{real})\cos\theta_{air} \qquad \text{(A-6)}$$

$$\cos\theta_a = f_{real}\cos\theta_{s,adv} + (1 - f_{real})\cos\theta_{air} \qquad \text{(A-7)}$$

where θ_r and θ_a is the apparent receding and advancing CAs, respectively; $\theta_{s,rec}$ and $\theta_{s,adv}$ is the local receding and advancing CAs at the solid-liquid contact part, respectively; θ_{air} is the local contact angle of the free surface between air and liquid (receding and advancing CAs equal to $180°$ in air); f_{real} is the real local solid-liquid contact fraction in the region of DCL. Eqs. (A-6) and (A-7) are very similar to the formulas proposed in Extrand's paper,[63] but $\cos\theta$ is applied rather than θ when interfacial energies is considered. In order to figure out the values of f_{real}, $\theta_{s,rec}$ and $\theta_{s,adv}$, we take the regularly patterned surface with square post

arrays for example. Schematic top views of DCL for a drop resting on the patterned surface are illustrated in Figure A-1. The post width and spacing are noted to be *a* and *b*, respectively.

For the real local solid-liquid contact fraction f_{real} in the region of DCL, there are two statements. The most common expression of the local contact fraction is considered as a local solid-liquid contact area fraction (we call it solid area fraction f_a) of the contact line.[41, 43] Note that for a uniformly patterned surface, the global solid area fraction equals to the local solid area fraction in the region of DCL. Taking the square post arrays for example, the solid-liquid area fraction equals to:

$$f_a = a^2/(a^2 + b^2) \qquad \text{(A-8)}$$

where *a* and *b* are corresponding to the parameters shown in Figure A-1. On the other hand, as discussed by Extrand,[63, 64] the local contact fraction is treated as a local linear fraction of the contact line (we call it solid linear fraction f_l), which equals to:

$$f_l = a/(a + b) \qquad \text{(A-9)}$$

However, f_a is valid only when the length scale of *a* and *b* should be comparable to the thickness of the liquid-air interface (on the order of molecular dimensions, 10^{-9}~10^{-8}m)[42] and thus DCL can cover the total area of a repetitive cell unit, see Figure A-1a; f_l is valid only when the contact line of the drop is assumed to be straight and local curvatures of the contact line can be ignored (in

fact, the contact line between posts is really not a line but is liquid-air interface[62] which can cover the repetitive cell unit partly). As a result, for the length scale in micrometer (the length scale discussed in this report), the real local solid-liquid contact fraction f_{real} can be underestimated if the solid area fraction f_a is used; on the contrary, the real solid-liquid contact fraction f_{real} can also be overestimated if the solid linear fraction f_l is used. As experimentally demonstrated in Section A.4, f_{real} shows a value between f_a and f_l. In particular, it shows that by decreasing the length scale of the microstructures while keeping f_a and f_l constant, f_{real} is first close to f_l and then decreases and approaches to f_a (see Section A.4). This indicates the DCL may sense more in the solid-liquid area fraction than solid-liquid linear fraction for microstructures with smaller length scale, see Figure A-1b.

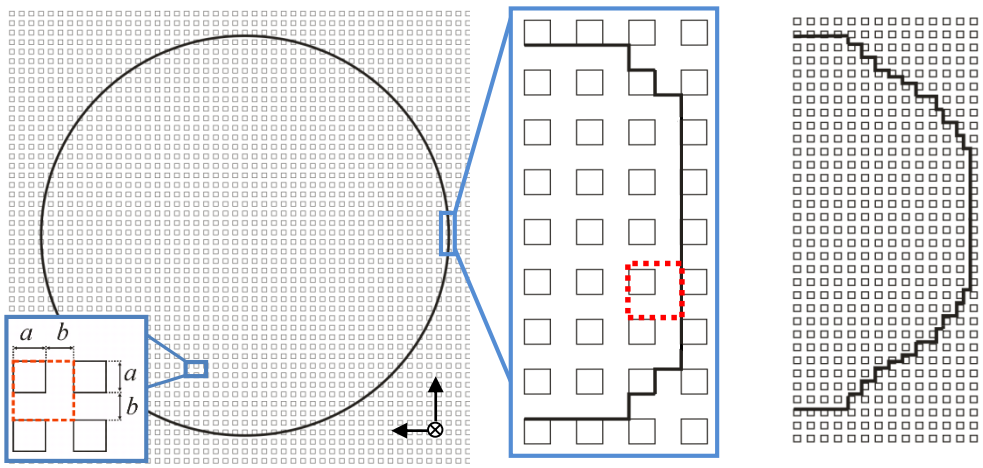

Figure A-1. Schematic top views of drop DCL for the drop on a patterned surface with square post arrays. (a) The inset shows the DCL shape on a large length scale microgeometrical surface. (b) DCL shape on a small length scale microgeometrical surface. Note that the dashed cells refer to the repetitive units.

To determine the value of local receding CA at the solid-liquid contact part ($\theta_{s,rec}$) in Eq. (A-6), a model of contact line retreating behavior is introduced in Figure A-2, similar to the models illustrated by Extrand[63] and Dorrer et al..[39] One can see that the drop exhibits a local receding CA equal to that on a smooth surface (θ_{r0}) when the contact line crosses the flat top of the post. As the drop volume is decreasing, the drop contact line retreats to the post edge, and then is pinned. Theoretically, the contact line cannot move until the same local receding CA (θ_{r0}) on the side wall of the post is established. Extrand[63] has ignored such pinning for composite states, and treated $\theta_{s,rec}$ as a value equal to θ_{r0}.

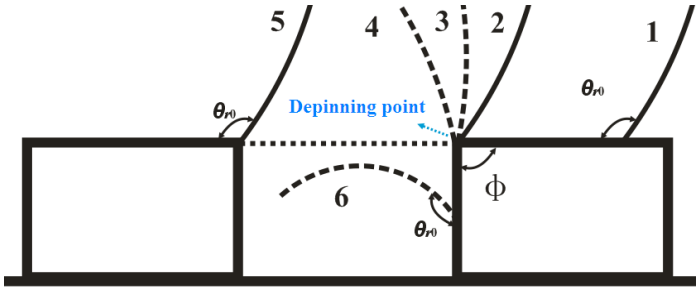

Figure A-2. An enlarged side view near the receding contact line of a drop suspended on the posts: 1-2 the drop contact line is retreating on the flat post top with a local receding CA equal to that exhibited on the smooth surface (θ_{r0}); 3-4 the contact line is pinned on the edge; 5 a new contact point is formed on the nearest post after depinning happens at 4; 6 theoretical contact line movement with local receding CA (θ_{r0}) on the side of the post, which will unlikely happen on a hydrophobic post with the solid edge angle Φ=90 °.

To determine the value of local advancing CA at the solid-liquid contact part $\theta_{s,adv}$ in Eq. (A-7), a model of the contact line advancing motion is shown in Figure A-3, which is also similar to the models illustrated by Extrand[63] and Dorrer

et al..[39] One can see that a drop exhibits a local advancing CA equal to that on a smooth surface (θ_{a0}) when the contact line crosses the flat top of the post. As the drop volume is increasing, the contact line continues to spread and finally reaches the post edge. Then, the contact line will be pinned on the post edge. Theoretically, until a CA of 180 ° is reached,[39] the meniscus near the contact point could then touch the next post and form a new contact point. As a result, the local advancing CA at the solid-liquid contact part appears to be $\theta_{s,adv}$ = 180 °, and so the apparent advancing CA (θ_a) from Eq. (A-7), no matter what f is, can be calculated to be 180 °. Based on the above analysis, Dorrer et al.[39] claimed that the advancing contact angles remain unaffected (θ_a ~180 °) as the microgeometrical parameters (f_a and S) varies. However, this may not be the truth because the meniscus will fluctuate about its equilibrium position, depending on the external energy transferred from the environment, e.g., mechanical vibrations.[65-67] The drop may sense the nearest post and form a new contact point before $\theta_{s,adv}$ reaches 180 °. Therefore, with certain external energy provided by the environment, the drops on surfaces with small post spacing can sense the nearest posts more easily than those on surfaces with large post spacing (for the same post width), indicating a smaller $\theta_{s,adv}$. However, $\theta_{s,adv}$ cannot be theoretically determined, since the external energy from the environment is unknown. The above speculations will be demonstrated based on experimental results in Section A.4.

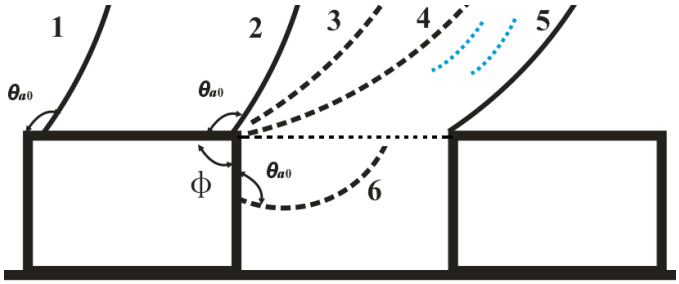

Figure A-3. An enlarged side view near the advancing contact line of a drop suspended on the posts: 1-2 the drop contact line is propagating on the flat post top with an advancing CA equal to that exhibited on the smooth surface (θ_{a0}); 3-4 the contact line is pinned on the corner; 5 a new contact point is formed on the nearest post when the meniscus of 4 is oscillating around its equilibrium position; 6 theoretical contact line movement with advancing CA (θ_{a0}) on the side of the post, which will unlikely happen on a hydrophobic post with solid edge angle Φ=90°.

A.3 Experimental Methods

A.3.1 Experimental Design

Patterned surfaces with different post shapes, i.e., square, triangle, and circle, were designed. Figure A-4 shows schematic depiction of repetitive unit cells for patterned surfaces with different microgeometries. Because the composite states are mainly investigated here, the solid area fraction f_a is selected to be the controlled geometrical parameter rather than the roughness r. f_a is defined as $a_1^2/(a_1+b_1)^2$, $0.43a_2^2/(a_2+b_2)^2$ and $0.79a_3^2/(a_3+b_3)^2$ for square, triangle and circle post arrays, respectively. To reflect the microgeometrical length scale (noted as S) for various microgeometrical shapes, the top surface area of individual post is used as the indication. As a result, S is defined as a_1^2, $0.43a_2^2$ and $0.79a_3^2$ for

square, triangle and circle post arrays, respectively. To indicate the difference between different geometrical shapes, edge length density P, characterized by the edge length per unit area, is defined as $4a_1/(a_1+b_1)^2$, $3a_2/(a_2+b_2)^2$ and $3.14a_3/(a_3+b_3)^2$ for square, triangle and circle post arrays, respectively. Microgeometrical effects on wetting behavior can be understood through the comparisons of surface wettability when the above geometrical parameters are precisely controlled.

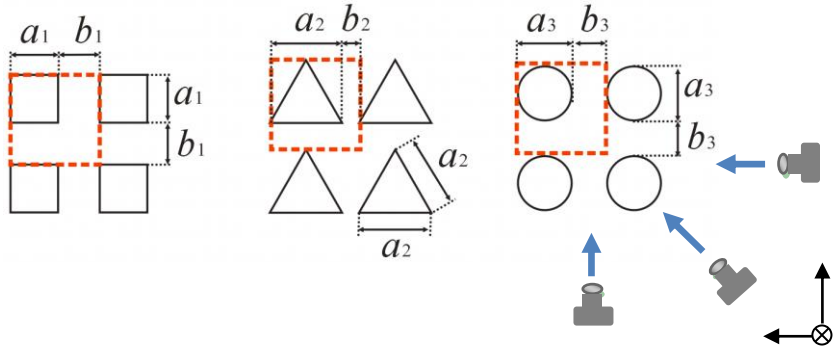

Figure A-4. Schematic depiction of top views for patterned surfaces with different microgeometries. The dashed cells refer to the repetitive units. Images of drops sitting on the post arrays were taken from azimuthal angle of (a) 0 °, (b) 45 °and (c) 90 °relative to x axis.

In order to investigate microgeometrical effects on wetting behavior, the size of surface microgeometrical parameters are carefully designed, which have been given in Tables A-1, A-2 and A-3. For features in each table, f_a and S for different microgeometries are kept constant. As a result, geometrical shape effect, e.g., the effect of P, could be shown by comparing wettability between different surfaces. Comparing features of Table A-2 to features of Table A-1, S is decreased by

halving the post width (a) and spacing (b) for different pattern shapes while f_a is kept constant, so length scale effect (S) could be shown by the wettability comparison between them. Comparing features of Table A-3 to features of Table A-1, the post widths for different pattern shapes are all halved while the cell area $(a+b)^2$ are kept constant, so the post size effect could be shown by the wettability comparison between Table A-1 and Table A-3. In addition, comparing features of Table A-3 to features of Table A-2, f_a is decreased while S is kept constant, so post density effect could be shown by the wettability comparison between Table A-2 and Table A-3. Note that two post heights 20 and 30 μm have been set, which are sufficient for drops to stay in composite state as shown in Section A.4.

Table A-1. Theoretical settings for microgeometries (f_a =0.28, S=256μm^2). a, b and h represent the post width, spacing and height, respectively; f_a, r_w represent the solid area fraction and Wenzel's roughness, respectively; θ_C and θ_w represent the CAs from Cassie's and Wenzel's equations, respectively; P and S represent the edge length density and length scale, respectively; θ_Y is 111 ° which is assumed to be the average of advancing and receding CAs on smooth surface.

Pattern	a (μm)	b (μm)	h (μm)	f_a [θ_C (°)]	r_w[θ_w (°)]	P(μm^{-1})	S(μm^2)
Square	16	14	30	0.28(144.4)	3.13(180)	0.071	256
			20	0.28(144.4)	2.42(145.9)	0.071	256
Triangle	24.3	5.7	30	0.28(144.4)	3.43(180)	0.081	256
			20	0.28(144.4)	2.62(153.7)	0.081	256
Circle	18	12	30	0.28(144.4)	2.89(171.4)	0.063	256
			20	0.28(144.4)	2.26(140.6)	0.063	256

Table A-2. Theoretical settings for microgeometries with smaller length scale (f_a =0.28, S=64μm^2)

Pattern	a (μm)	b (μm)	h (μm)	f_a [θ_C (°)]	r_w[θ_w (°)]	P(μm^{-1})	S(μm^2)
Square	8	7	30	0.28(144.4)	5.27(180)	0.14	64
			20	0.28(144.4)	3.84(180)	0.14	64
Triangle	12.2	2.8	30	0.28(144.4)	5.86(180)	0.16	64
			20	0.28(144.4)	4.24(180)	0.16	64
Circle	9	6	30	0.28(144.4)	4.78(180)	0.13	64
			20	0.28(144.4)	3.52(180)	0.13	64

Table A-3. Theoretical settings for microgeometries smaller f_a (f_a=0.071, S=64μm^2)

Pattern	a (μm)	b (μm)	h (μm)	f_a [θ_C (°)]	r_w[θ_w (°)]	P(μm^{-1})	S(μm^2)
Square	8	22	30	0.071(162.4)	2.07(135)	0.036	64
			20	0.071(162.4)	1.71(125.8)	0.036	64
Triangle	12.2	17.8	30	0.071(162.4)	2.22(139.3)	0.041	64
			20	0.071(162.4)	1.81(128.3)	0.041	64
Circle	9	21	30	0.071(162.4)	1.95(131.7)	0.031	64
			20	0.071(162.4)	1.63(123.9)	0.031	64

A.3.2 Preparation of Patterned Silicon Substrates

All surface microgeometries described above are fabricated by lithography and reactive ion etching (RIE) techniques on pure silicon wafers covered by a 500nm thick silicon dioxide layer, which is schematically shown in Figure A-5. Firstly, patterns of designed shapes were transferred from a photomask (NanoFab,

University of Alberta) to a silicon dioxide layer on 4 in. (100)-orientaion silicon wafers (P/B-doped, resistivity from 1 to 35 ohm-cm, thichkness 525±25 μm, Silicon Valley Microelectronics, Inc.) by contact lithographic techniques (HPR 504 photoresist, ABM Mask Aligners) and reactive ion etching process (STS-RIE). The patterned silicon dioxide acted as a masking layer in the following Cryo process (Oxford ICP-RIE Cryo Etch), which produced an anisotropic etch in silicon. Etching depth or post height can be precisely controlled by etching time. When etching process was complete, holes were drilled in the center of each pattern (1.5cm×1.5cm) by diamond micro-drills (MCDU30, diameter 0.762 mm, UKAM) to allow for mounting of a syringe below the surface to create a drop on top of the surface, see Figure A-6. Then, the wafers were cleaned in deionized water, iso-propanol, and acetone in sequence. In order to ensure chemical homogeneity of surfaces, the patterned silicon wafers were kept in thermal oxidation tube at 900 ℃ for 10 min to grow a 70nm thick silicon dioxide layers on the newly exposed silicon surfaces.

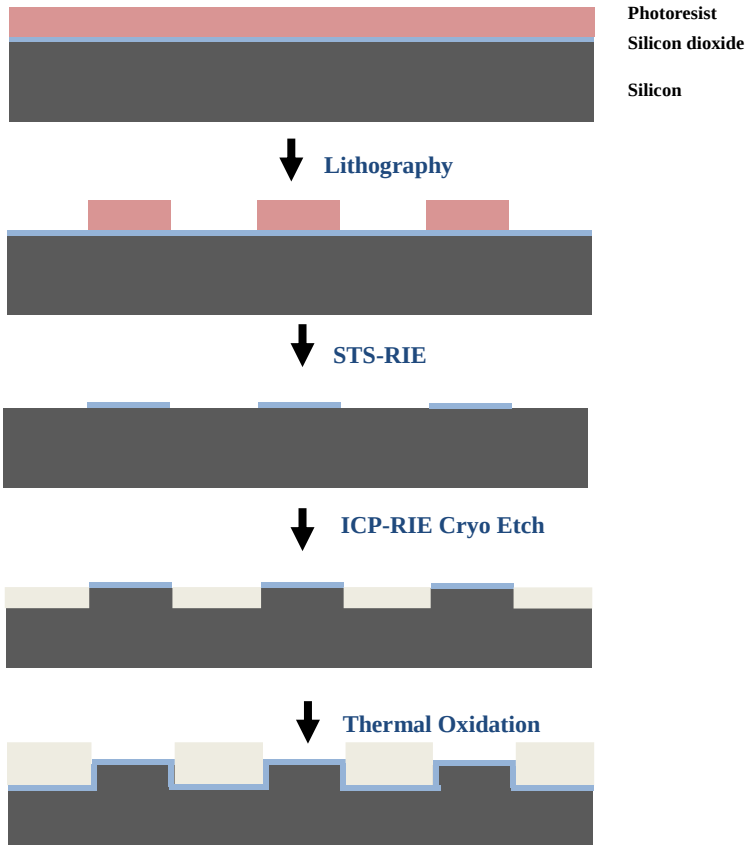

Figure A-5. A schematic illustration for the micromachining procedure on silicon wafers. The thermal oxidation process is to ensure the chemical homogeneity.

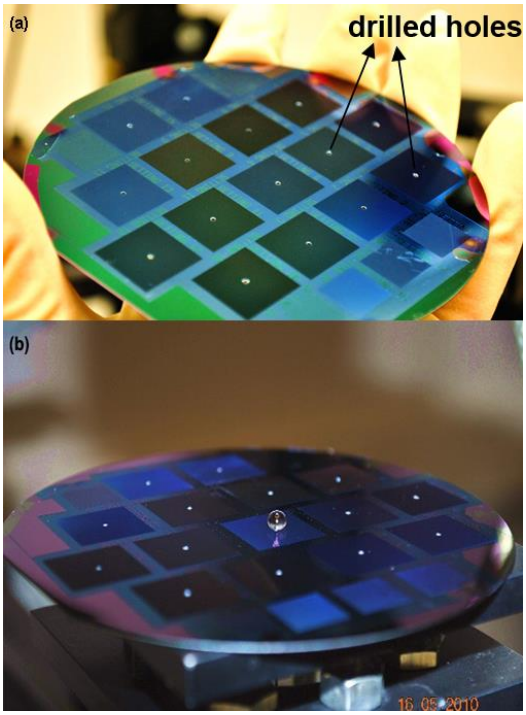

Figure A-6. (a) A patterned silicon substrate by lithography and RIE techniques with drilled holes on. (b) A patterned silicon substrate mounted on the stage of a contact angle measurement system with syringe below to create a drop on top of the surface.

A.3.3 Surface Modification

The deposition cycle part of the Bosch process (Oxford Plasmalab ICP-RIE) was used to modify surface chemical property. Using C_4F_8 source gas, a chemically inert passivation layer (a substance similar to Teflon) was homogeneously coated on the patterned silicon surface. When the deposition time is set to be 90 sec., a 60 nm thick polymer film can be detected.

A.3.4 Surface Characterization

Scanning Electron Microscope (SEM-LEO 1430) and White Light Confocal Microscopy (LCM-CSM 700) were applied to check the dimensions of the microgeometries. Feature sizes within 5% deviation from the ideal sizes shown in Tables A-1, A-2 and A-3 are accepted, since there is 7% system error during the micromachining and even in the dimensional measurement. The thickness of C_4F_8 passivation layer and silicon dioxide layer can be detected by a contact profilometer (Alphastep 200) and Filmetrics Resist and Dielectric Thickness Mapping System, respectively.

A.3.5 Contact Angle Measurements

A custom-built apparatus[34, 68] was used for measuring advancing and receding CAs for the quasi-static advancing and receding contact line. A clean syringe filled with the deionized water was mounted under the silicon wafer, with the tip position just underneath the top of the hole, see Figure A-6b. The syringe was driven by a motor at a rate of 0.5 μL/s for the advancing and receding CAs measurements by adding and removing the water from the drop, which is low enough that inertial effects are minor. Side (from various azimuthal angles, see Figure A-4) and top images of drops were recorded by two cameras. Drop image analysis programs were developed to determine the contact angles. Side images from azimuthal angles 0 ° to 170 ° were used to generate the DCL shape. Note that

it is impossible to capture the DCL from the top view when the contact angle is larger than 90 °.

A.4 Results and Discussion

The advancing (θ_a) and receding (θ_r) contact angles as well as contact angle hysteresis (CAH) for water on smooth silicon wafers are given in Table A-4. There are four kinds of surfaces for smooth silicon wafer, i.e., surfaces untreated (SWU), treated (SWT) by thermal oxidation, and modified by C_4F_8 passivation (SWU + C_4F_8 and SWT + C_4F_8). Note that the Young's CA can be approximated to be the average of advancing and receding CAs. Figure A-7 shows the water drop images sitting on smooth SWT before and after surface modification. One can see that a hydrophilic surface can be modified to be hydrophobic effectively by C_4F_8 passivation treatment.

Table A-4. CA measurement on smooth silicon wafers. Silicon wafers untreated (SWU); silicon wafers treated (SWT) in 900 ℃ (10min), SiO_2 thickness: 70nm; SWU + C_4F_8 passivation (90sec.), polymer thickness: 60nm; SWT + C4F8 passivation (90sec.), polymer thickness: 60nm. Note that SD is the standard deviation for measurements.

	θ_a (°) ± SD	θ_r (°) ± SD	CAH (°) ± SD
SWU	48.5 ±1.29	23.7 ±1.28	24.8 ±0.28
SWT	57.1 ±0.84	11.6 ±0.11	45.0 ±0.32
SWU + C_4F_8	123.4 ±0.06	99.3 ±1.05	23.8 ±0.61
SWT + C_4F_8	123.5 ±0.10	99.6 ±0.19	23.8 ±0.23

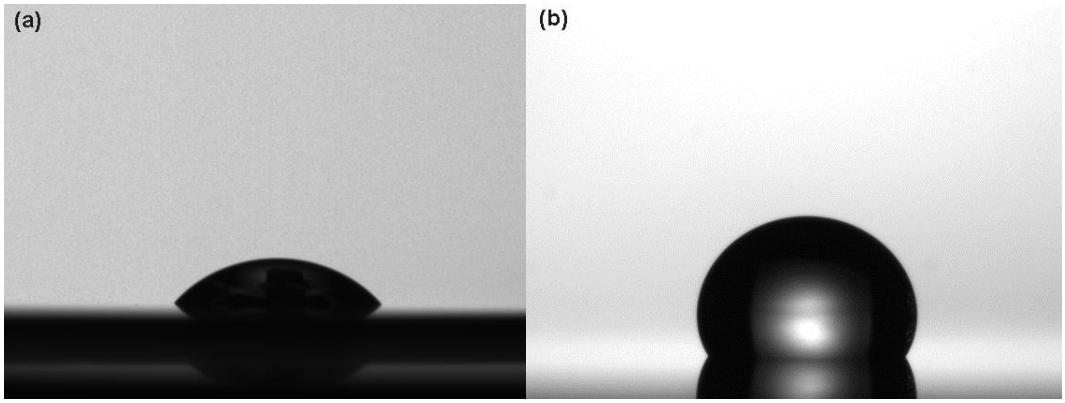

Figure A-7. Images of water drops sitting on (a) smooth SWT surface; (b) smooth SWT surface treated by C_4F_8 passivation.

Figure A-8 shows the SEM images of surfaces patterned with square, triangle and circle post arrays. The dimensions of post width, spacing and height are measured by SEM and LCM. The results show that the designed microgeometrical structures with required dimensions described in Tables A-1, A-2 and A-3 have been successfully realized by the lithography and RIE technologies.

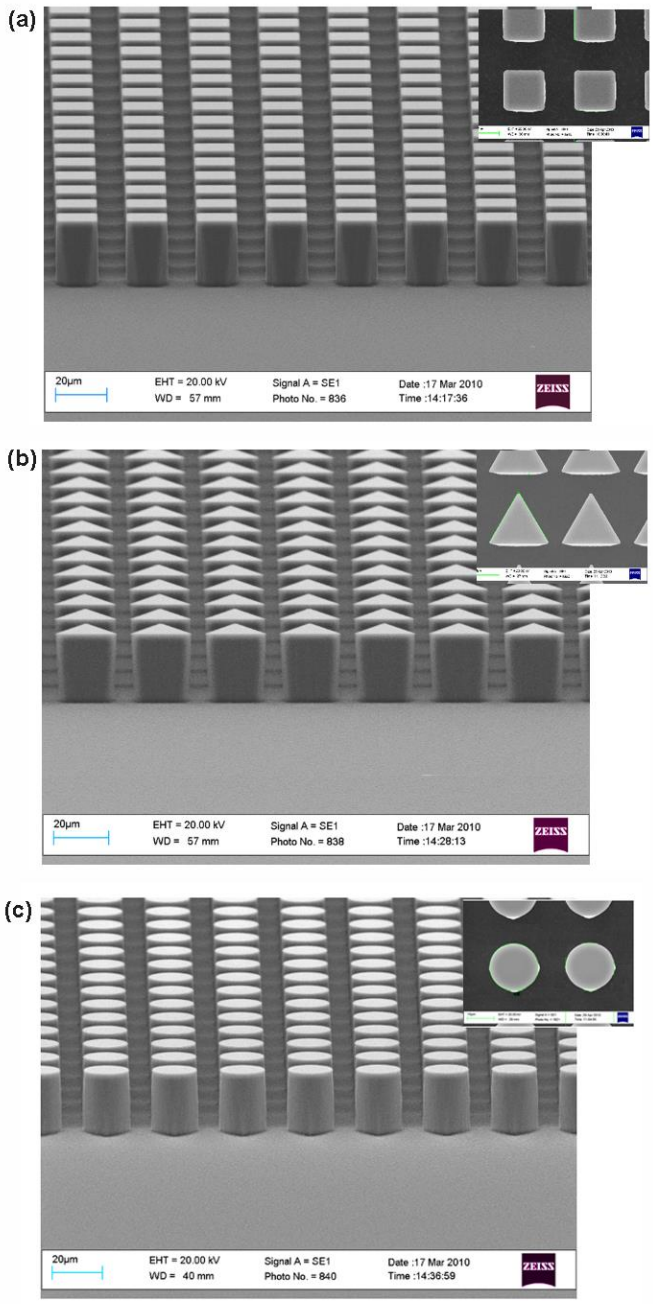

Figure A-8. SEM images of the surfaces patterned with (a) square posts, (b) triangle posts and (c) circle posts for microstructures illustrated in Table A-1 (post height = 30 µm). The insets show the top views of the microstructures with different post shapes.

A.4.1 Wetting on Hydrophilic Patterned Surfaces

Wetting behavior on patterned surfaces before surface modification has been tested. Figure A-9a shows the side views of a water drop spreading on the square post arrays (Table A-1, post height=20 μm) from azimuthal angle of 0 °. It is clear from the images that a liquid film inside the surface microstructures propagates faster than the drop (liquid is added by the syringe at a rate of 0.5μL/s). Attempts to measure the contact angles failed because the water drop would penetrate into the microstructures to form a liquid film and CA would decreases to 0 degree. Bico *et al.*[69] derived a criterion for such wetting phenomenon (they called it an intermediate between the ones for spreading and for imbibition),

$$\theta_Y < \theta_{Critical,}\ \cos\theta_{Critical} = (1-f)/(r-f) \qquad \text{(A-10)}$$

In our case, the Young's CA (θ_Y equals to 34.3 °, the average of advancing and receding CAs on smooth surface) is smaller than the critical CA ($\theta_{Critical}$ equals to 70.3 °) (from Table A-1, f_a=0.28, r=2.42), and so the condition shown in Eq. (A-10) is satisfied. In particular, a rectangular spreading shape has been observed from the top views (Figure A-9b). Interestingly, the same rectangular spreading pattern has been seen on the other microgeometrical surfaces, regardless of the microgeometrical shapes, i.e., square, triangle and circle post arrays (Tables A-1, A-2 and A-3 with post heights 20 and 30 μm). The results reveal that the spreading speed of liquid film on patterned surfaces with tetragonally arrayed posts along x and y axis are slower than that along the diagonal directions

regardless of what post shape it is. Dorrer and Ruehe[70] have also observed a similar wetting phenomenon on hydrophilic square post arrays.

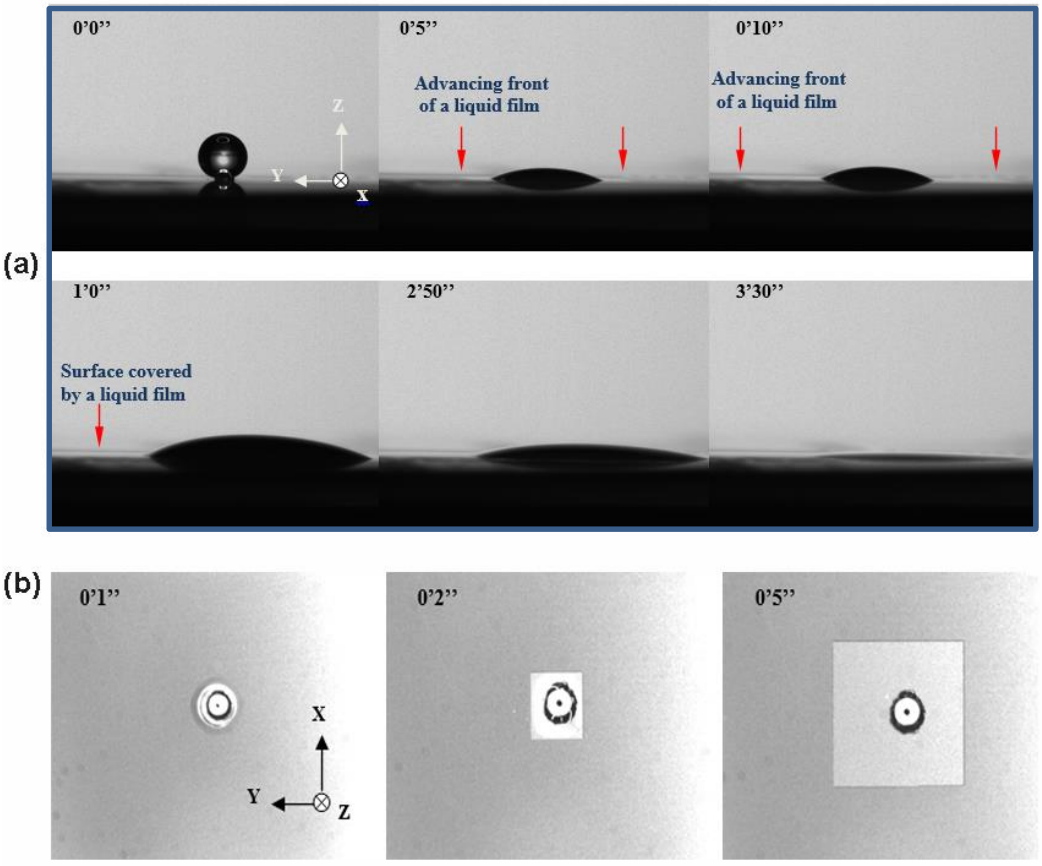

Figure A-9. (a) Side and (b) top views for water drop on the square post arrays before surface modification. Note that the syringe is underneath the drop through the hole. The insets show the time sequence.

A.4.2 Wetting on Hydrophobic Patterned Surfaces

Figure A-10 shows that water drop can sit on top of posts for the patterned surface after surface modification. Light can penetrate through the post spacing underneath the drop, indicating air entrapment and composite wetting state.

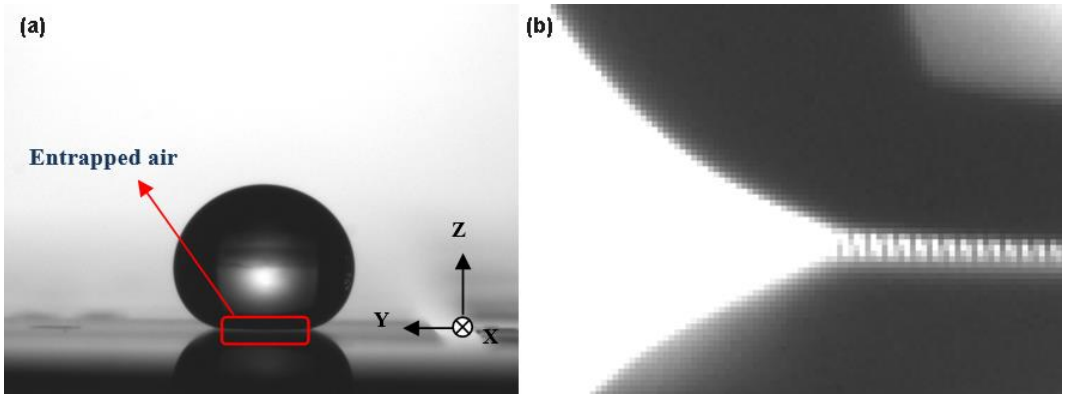

Figure A-10. (a) Water drop sitting on the chemically modified patterned surface. (b) A partial enlargement at the three phase contact point. Note that light can penetrate through the post spacing.

A.4.2.1 CAs from Azimuthal Angle of Zero Degree

Comparison of variations of apparent drop advancing and receding CAs with respect to pattern types and geometrical parameters are shown in Figure A-11, measured from 0 degree azimuthal angle. Student's t-test has been applied for the comparison of CA values discussed below. One can see that despite some errors generated by the light penetration mentioned above, for different post heights (Figure A-11a and b), contact angles almost show the same trend. As a result, only the CA data for microgeometries with post height 20 μm has been applied for analysis below.

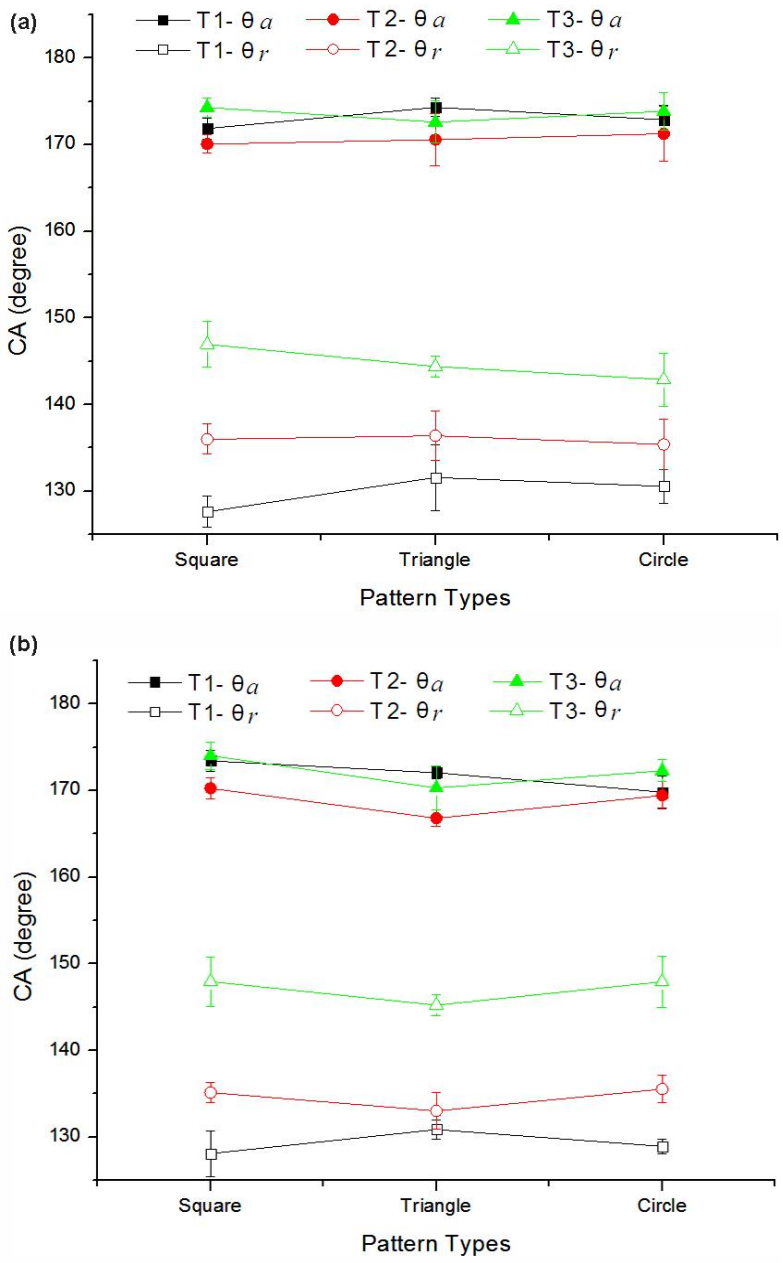

Figure A-11. Variations of advancing (θ_a) and receding (θ_r) contact angles with respect to pattern types and geometrical parameters corresponding to Tables A-1 (T1: f_a =0.28, S=256μm^2), A-2 (T2: f_a =0.28, S=64μm^2) and A-3 (T3: f_a=0.071, S=64μm^2) (a) for post height 20 μm and (b) post height 30 μm. Note that the CAs were measured from azimuthal angle of 0 degree.

A.4.2.1.1 Receding CA Analysis

Comparing the apparent receding CAs on patterned surfaces with microgeometrical parameters given in Tables A-1 (f_a =0.28, S=256μm^2) and A-2 (f_a =0.28, S=64μm^2), a quite different wetting behavior can be observed though f_a has been fixed, see Figure A-11a. Taking the square post arrays for example, the apparent receding CA (θ_r) for the microtexture of Table A-1 (θ_r=127.6°, f_{real}=0.47, f_l=0.53, f_a=0.28, S=256μm^2) is much smaller than that for the microtexture of Table A-2 (θ_r=136.0°, f_{real}=0.34, f_l =0.53, f_a =0.28, S=64μm^2), showing a strong dependence on the length scale S; note that f_{real} is calculated by substituting θ_r in Eq. (A-6), and the local solid linear fraction f_l for square post arrays is obtained from Eq. (A-9). The same phenomenon can be observed in Dorrer's data:[39] for the patterned surfaces with the same f_l and f_a, the apparent receding CA will increase (so the real local contact fraction f_{real} will decrease) dramatically when the length scale S decreases. In particular, it is found that the value of f_{real} is always between f_l and f_a. When S decreases, f_{real} decreases from a value close to f_l to a value close to f_a. In order to better understand the dependence of f_{real} on S, it is useful to establish theoretical relationship between them. Based on the experimental data of apparent receding CAs from ours and Dorrer's,[39] we propose a phenomenological correlation as:

$$f_{real} = f_l(1-e^{-S/A}) + f_a e^{-S/A} \qquad \text{(A-11)}$$

where S is the length scale and A (μm^2) is a fitting parameter. Combining Eqs. (A-6) and (A-11), a theoretical relationship between the apparent receding CA (θ_r) and length scale (S) can be established. Figure A-12 shows the comparison between the experimental apparent receding CA data and theoretically predicted apparent receding CAs. As seen, the predicted apparent receding CAs are quite consistent with the experimental data. Therefore, a quantitative correlation between apparent receding CA and length scale has been successfully established. It is worth pointing out that from Eq. (A-11), a maximum receding CA can be reached when S approaches 0 (f_{real} approaches f_a), i.e., a small S is favored for water-repellent rough surfaces. This may be one of the reasons that needle-like structure[71] is usually preferred for constructing superhydrophobic surfaces.

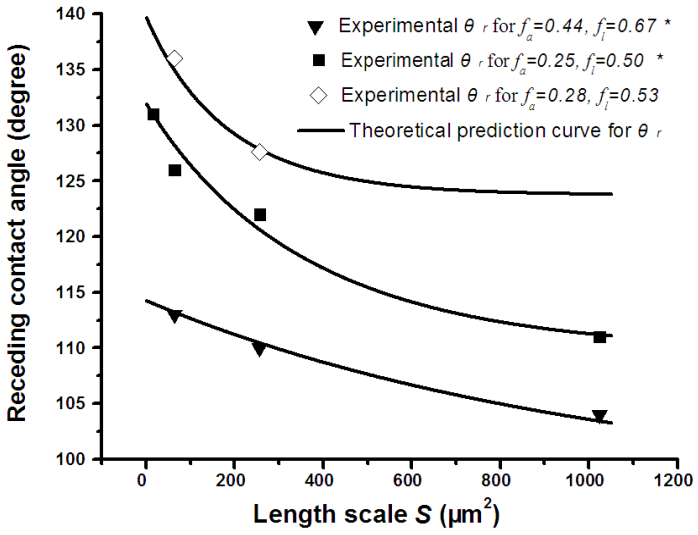

Figure A-12. The comparison between the experimental apparent receding CA data and theoretically predicted apparent receding CAs for square post arrays. Note that the experimental data noted by symbol * is from Dorrer's experiment.[39]

In addition, for surfaces with different microgeometrial shapes (i.e., square, triangle and circle) but the same f_a and S values, minor differences have been shown for the receding CAs. From Eq. (A-11), we can attribute the minor difference to the different solid linear fraction f_l for varied post shapes. For drops on triangle and circle post arrays, determination of the value of f_l needs further information of a detailed DCL profile.

A.4.2.1.2 Advancing CA Analysis

Unlike the apparent receding CA, the apparent advancing CA is difficult to be predicted by Eqs. (A-7) and (A-11), since the local advancing CA ($\theta_{s,adv}$) in Eq. (A-7) at the solid-liquid contact part cannot be theoretically determined as discussed in Section A.2.2. However, based on the experimental apparent advancing CA results, $\theta_{s,adv}$ can be calculated by Eq. (A-7) for all the patterned surfaces. Note that f_{real} in Eq. (A-7) at the advancing DCL is assumed to be equal to that at the receding DCL for axisymmetric post shapes. By comparing $\theta_{s,adv}$ between patterned surfaces with various microgeometrical parameters, the edge pinning effect for the advancing contact line at the microgeometrical edge can be revealed. For example, comparing $\theta_{s,adv}$ for square post arrays of Table A-2 ($\theta_{s,adv}$=162.8°, a=8 μm, b=7 μm, h=20 μm) and Table A-3 ($\theta_{s,adv}$=167°, a=8 μm, b=22 μm, h=20 μm), it can be seen that $\theta_{s,adv}$ shows a smaller value for the one with small post spacing (surface of Table A-2) than that with large post spacing (surface of Table A-3). This is consistent to the speculations for the pinning property of advancing contact line discussed in Section A.2.2; i.e., for the same

post width, small post spacing can induce a smaller $\theta_{s,adv}$. Interestingly, the same trend can be found for triangle and circle post arrays, respectively.

Figure A-13 shows variations of CAH with respect to microgeometrical shapes and geometrical parameters corresponding to Tables A-1, A-2 and A-3. Because CAH is the result of the difference of θ_a and θ_r, there is a direct relation between the variations of CAH and variations of θ_a and θ_r. Due to the much less pronounced variation of θ_a than variation of θ_r, CAH shows a very similar trend to θ_r.

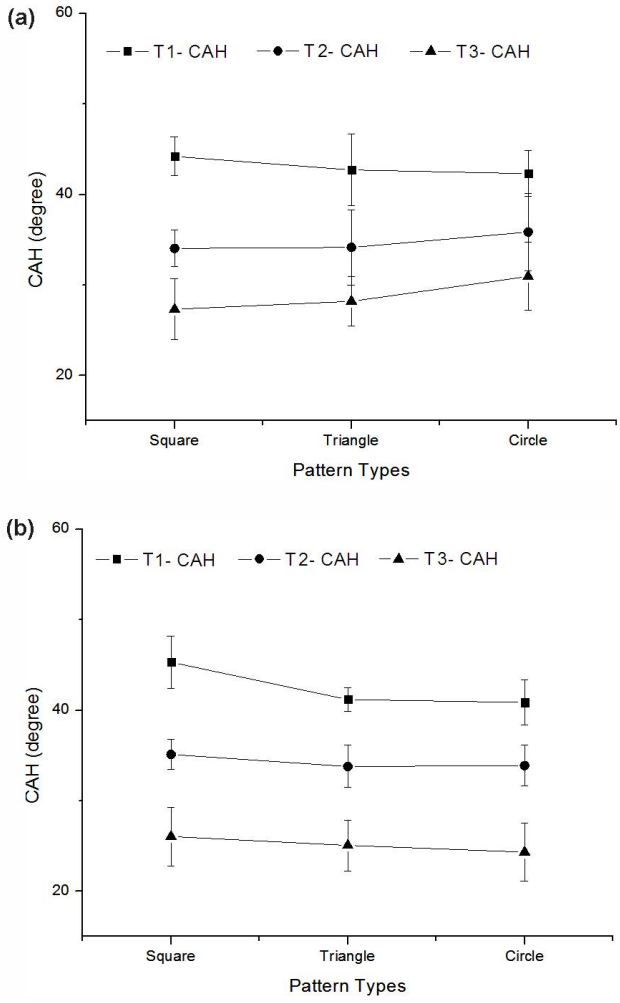

Figure A-13. Variations of CAH with respect to pattern types and geometrical parameters corresponding to Tables A-1 (T1: f_a =0.28, S=256μm^2), A-2 (T2: f_a =0.28, S=64μm^2) and A-3 (T3: f_a=0.071, S=64μm^2) (a) for post height 20 μm and (b) post height 30 μm. Note that the CAs were measured from azimuthal angle of 0 degree.

A.4.2.2 CAs from other Azimuthal Angles

It is noted that even on the same patterned surface, the wettability is different from different azimuthal angles (see Figure A-4). For square and circle post arrays, the same post and plane symmetries can be seen from azimuthal angles 0 ° and 90 °,

respectively; different post and plane symmetries can be seen from azimuthal angles 0° and 45° for square; the same post symmetry but different plane symmetry can be seen from azimuthal angles 0° and 45° for circle post arrays. Accordingly, CAs are measured from azimuthal angles 0° and 45° for square and circle post arrays, respectively. For triangle post arrays, the post and plane conditions become asymmetric and extremely complex from azimuthal angles 45°, which will not be investigated. Though post and plane are still asymmetric from azimuthal angle of 90°, some interesting wetting phenomena could be observed from this direction (see below). Therefore, CAs are measured from 0° and 90° for triangle post arrays.

To make our explanation easily understandable, schematic illustrations of two columns of square post arrays as well as the DCL pinned at the rear post edge from the two azimuthal angles are shown in Figure A-14. Similar to the analysis in Section A.4.2.1, the apparent receding CA can be determined by the real local solid-liquid contact fraction f_{real} which is related to f_a, f_l and S (Eq. (A-6) and Eq. (A-11). For square post arrays observed from 0° and 45°, they have the same f_a and S which is independent on the azimuthal angles. However, by a simple geometrical analysis in Figure A-14, f_l (as well as f_{real}) at the receding DCL from azimuthal angle 45° will be smaller than that from azimuthal angle 0°, leading to a larger receding CA from azimuthal angle 45° than that from azimuthal angle 0°. This is demonstrated by the experimental results in Table A-5, which shows the CA results measured from various azimuthal angles. One can see that for square

post arrays, there is a large increase of receding CAs when the azimuthal angle changes from 0° to 45°. In addition, the local advancing CA in the solid-liquid contact part ($\theta_{s,adv}$) can be calculated from Eq. (A-7) based on the measured advancing and receding CAs, see Table A-5. One can see that $\theta_{s,adv}$ for square post array observed from 45° ($\theta_{s,adv}$ = 166.0°) is smaller than that from 0° ($\theta_{s,adv}$ = 168.1°), due to the smaller column spacing observed from angle 45°(=0 μm) than that from 0° (=14 μm), which is consistent with the advancing CA analysis in Section A.4.2.1.

Table A-5. CA Measurement on Patterned Surfaces from Various Azimuthal angles (For Microgeometries of Table A-1, Post height=20 μm); note that SD is the standard deviation for measurements.

	θa(°)	SD-θa	θr(°)	SD-θr	CAH(°)	SD-CAH	$f$real from θr	$\theta s,adv$(°)
Square-0°	171.9	1.19	127.6	1.79	44.2	2.15	0.47	168.1
Square-45°	171.6	1.84	134.3	1.91	37.3	2.66	0.36	166.0
Circle-0°	172.9	1.62	130.6	1.95	42.3	2.53	0.42	169.0
Circle-45°	170.4	1.52	134.6	1.17	35.8	1.92	0.36	163.9
Triangle-0°	174.3	1.08	131.6	3.81	42.7	3.96	0.40	171.0
Triangle-90°- right	175.4	1.84	130.6	2.30	44.9	2.95	0.42	172.9
Triangle-90°- left	172.6	1.81	131.9	1.32	40.8	2.24	0.40	168.3

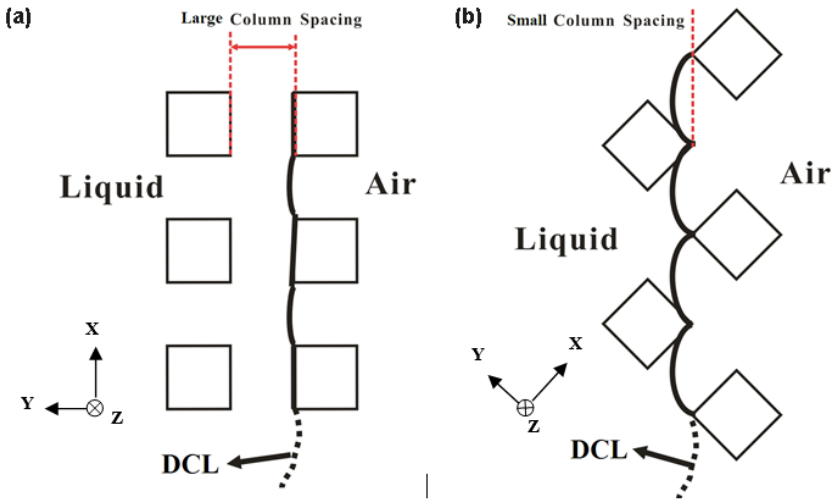

Figure A-14. Schematic top views of two square post columns from azimuthal angles (a) 0 degree and (b) 45 degree. Note that the shapes of contact line are shown when the DCLs reach the post edges.

Schematic top views of two circle post columns from azimuthal angles 0 ° and 45 ° have been shown in Figure A-15. Receding CA is estimated to be larger from azimuthal angle 45 ° than that from 0 °, attributing to the decreased f_l and f_{real} (similar to the above analysis for square post arrays). This is also demonstrated by the experimental results in Table A-5, which shows that the receding CA from azimuthal angle 45 ° is larger than that from 0 °. In addition, the local advancing CA $\theta_{s,adv}$ for circle post arrays observed from 45 ° ($\theta_{s,adv}$ = 163.9 °) is calculated to be smaller than that from 0 ° ($\theta_{s,adv}$ = 169.0 °), based on the measured advancing and receding CAs. The reason is that there is a smaller column spacing observed from azimuthal angle 45 ° (=3.21 μm) than that from 0 ° (=12 μm).

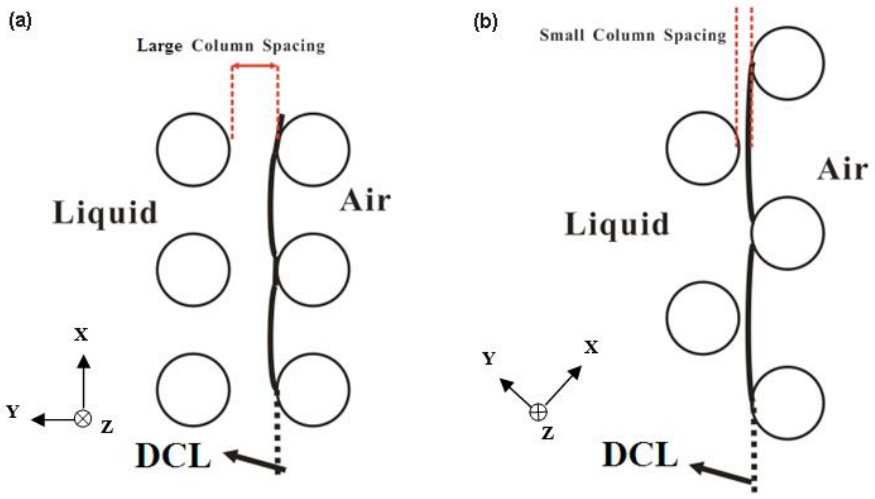

Figure A-15. Schematic top views of two circle post columns from azimuthal angles (a) 0 degree and (b) 45 degree. Note that the shapes of contact line are shown when the drop DCLs reach the post edges.

The wetting behavior becomes more complex for triangle post arrays when it is observed from 90°. Since the drop DCL of the left side and right side have different wetting conditions (Figure A-16), the advancing and receding CAs should be measured separately for the two sides. From Table A-5, it is noted that the receding CA for the left side is larger than that for the right side when it is observed from 90°. This happens because f_l and f_{real} (similar to the above analysis for square post arrays) at the receding DCL for the left side ($L4$) is smaller than that for the right side ($L1$). For the local advancing CA, $\theta_{s,adv}$ can be calculated based on the measured advancing and receding CAs. One can see that $\theta_{s,adv}$ (172.9°) on the right side is larger than that on the left side (168.3°). This may be

attributed to a weaker depinning point for the advancing DCL on the right side (*L*3) than that on the left side (*L*6), see Figure A-16.

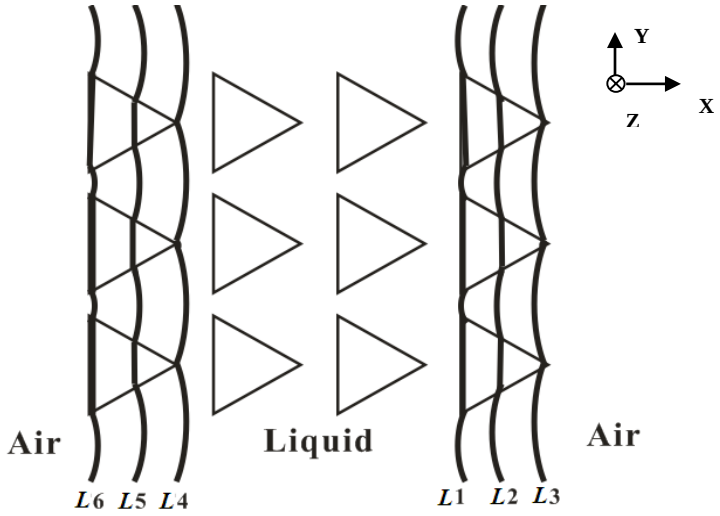

Figure A-16. Schematic top view of triangle post arrays from azimuthal angle of 90 degree. *L*1, *L*2 and *L*3 represent the DCL at the right side of the drop; *L*4, *L*5 and *L*6 represent DCL at the left side of the drop.

A.5 Conclusions

In this study, patterned surfaces with three microgeometry arrays (square, triangle and circle) have been obtained by micro/nanofabrication techniques. Wetting behavior of water drops on those surfaces has been systematically investigated. An intermediate wetting state between spreading and imbibition has been observed on microstructured hydrophilic silicon surfaces. After surface modification by C_4F_8 passivation, water drops can sit on top of the microgeometrical posts and show superhydrophobicity. Several important effects of microgeometries on the wetting behavior have been discussed, i.e., length scale

effect, edge and corner pinning effect, geometrical shape effect, direction-dependent effect, etc. In particular, it is found that the receding CA is between the CAs calculated by solid area fraction and solid linear fraction, depending on the microgeometrical length scale. In addition, CA results from different azimuthal angles reveal that wettability has a strong dependence on the orientation. For one patterned surface, the difference of edge/corner pinning effect in different directions can influence the receding CAs greatly. Furthermore, drop can even exhibit anisotropic wetting property from one azimuthal angle, depending on the microgeometrical shape, e.g., triangle post arrays. By designing the microgeometries on the patterned surfaces, a tunable wettability or a controlled drop wetting behavior can be achieved.

References

(1) Herminghaus, S.; Brinkmann, M.; Seemann, R. *Ann. Rev. Mater. Res.* **2008,** *38*, 101-121.

(2) Bonn, D.; Eggers, J.; Indekeu, J.; Meunier, J.; Rolley, E. *Rev. Mod. Phys.* **2009,** *81*, 67.

(3) Genzer, J.; Bhat, R. R. *Langmuir* **2008,** *24*, 2294-2317.

(4) Morgenthaler, S.; Zink, C.; Spencer, N. D. *Soft Matter* **2008,** *4*, 419-434.

(5) Hong, X.; Gao, X.; Jiang, L. *J. Am. Chem. Soc.* **2007,** *129*, 1478-1479.

(6) Zhao, Y.; Lu, Q.; Li, M.; Li, X. *Langmuir* **2007,** *23*, 6212-6217.

(7) Chen, Y.; He, B.; Lee, J.; Patankar, N. A. *J. Colloid Interface Sci.* **2005,** *281*, 458-464.

(8) Sandre, O.; Gorre-Talini, L.; Ajdari, A.; Prost, J.; Silberzan, P. *Phys. Rev. E* **1999,** *60*, 2964-2972.

(9) Zhu, L.; Feng, Y.; Ye, X.; Zhou, Z. *Sens. Actuators, A* **2006,** *A130-A131*, 595-600.

(10) Shastry, A.; Case, M. J.; Boehringer, K. F. *Langmuir* **2006,** *22*, 6161-6167.

(11) Su, Y.; Ji, B.; Zhang, K.; Gao, H.; Huang, Y.; Hwang, K. *Langmuir* **2010,** *26*, 4984-4989.

(12) Cheng, Z.; Gao, J.; Jiang, L. *Langmuir* **2010**.

(13) Lai, Y. K.; Gao, X. F.; Zhuang, H. F.; Huang, J. Y.; Lin, C. J.; Jiang, L. *Adv. Mater.* **2009,** *21*, 3799-3803.

(14) Barthlott, W.; Neinhuis, C. *Planta* **1997,** *202*, 1-8.

(15) Neinhuis, C.; Barthlott, W. *Ann. Bot.* **1997,** *79*, 667-677.

(16) Koch, K.; Bhushan, B.; Jung, Y. C.; Barthlott, W. *Soft Matter* **2009,** *5*, 1386-1393.

(17) Koch, K.; Bhushan, B.; Barthlott, W. *Prog. Mater. Sci.* **2009,** *54*, 137-178.

(18) Bohn, H. F.; Barthlott, W. *Langmuir* **2009**.

(19) Koch, K.; Bhushan, B.; Barthlott, W. *Soft Matter* **2008,** *4*, 1943-1963.

(20) Zheng, Y.; Gao, X.; Jiang, L. *Soft Matter* **2007,** *3*, 178-182.

(21) Lee, W.; Jin, M. K.; Yoo, W. C.; Lee, J. K. *Langmuir* **2004,** *20*, 7665-7669.

(22) Gao, X.; Jiang, L. *Nature* **2004,** *432*, 36.

(23) Hu, D. L.; Chan, B.; Bush, J. W. M. *Nature* **2003,** *424*, 663-666.

(24) Feng, X.-Q.; Gao, X.; Wu, Z.; Jiang, L.; Zheng, Q.-S. *Langmuir* **2007,** *23*, 4892-6.

(25) Gao, X.; Yan, X.; Yao, X.; Xu, L.; Zhang, K.; Zhang, J.; Yang, B.; Jiang, L. *Adv. Mater. (Weinheim, Ger.)* **2007,** *19*, 2213-2217.

(26) Zheng, Y.; Bai, H.; Huang, Z.; Tian, X.; Nie, F.-Q.; Zhao, Y.; Zhai, J.; Jiang, L. *Nature* **2010,** *463*, 640-643.

(27) Garrod, R. P.; Harris, L. G.; Schofield, W. C. E.; McGettrick, J.; Ward, L. J.; Teare, D. O. H.; Badyal, J. P. S. *Langmuir* **2007,** *23*, 689-693.

(28) Zhai, L.; Berg, M. C.; Cebeci, F. C.; Kim, Y.; Milwid, J. M.; Rubner, M. F.; Cohen, R. E. *Nano Letters* **2006,** *6*, 1213-1217.

(29) Parker, A. R.; Lawrence, C. R. *Nature* **2001,** *414*, 33-34.

(30) Zhang, X.; Shi, F.; Niu, J.; Jiang, Y.; Wang, Z. *J. Mater. Chem.* **2008,** *18*, 621-633.

(31) Roach, P.; Shirtcliffe, N. J.; Newton, M. I. *Soft Matter* **2008,** *4*, 224-240.

(32) Wenzel, R. N. *J. Ind. Eng. Chem.* **1936,** *28*, 988-994.

(33) Cassie, A. B. D.; Baxter, S. *Trans. Faraday Soc.* **1944,** *40*, 546-551.

(34) Pierce, E.; Carmona, F. J.; Amirfazli, A. *Colloids Surfaces, A* **2008,** *323*, 73-82.

(35) Johnson, R. E., Jr.; Dettre, R. H. *Adv. Chem. Ser.* **1964,** *43*, 112-135.

(36) Li, W.; Amirfazli, A. *J. Colloid Interface Sci.* **2005,** *292*, 195-201.

(37) Dorrer, C.; Ruehe, J. *Soft Matter* **2009,** *5*, 51-61.

(38) Oner, D.; McCarthy, T. J. *Langmuir* **2000,** *16*, 7777-7782.

(39) Dorrer, C.; Ruehe, J. *Langmuir* **2006,** *22*, 7652-7657.

(40) Gao, L.; McCarthy, T. J. *Langmuir* **2007,** *23*, 3762-3765.

(41) McHale, G. *Langmuir* **2007,** *23*, 8200-8205.

(42) Nosonovsky, M. *Langmuir* **2007,** *23*, 9919-9920.

(43) Panchagnula, M. V.; Vedantam, S. *Langmuir* **2007,** *23*, 13242.

(44) Milne, A. J. B.; Amirfazli, A. *Adv. Colloid Interface Sci.* **2012,** *170*, 48-55.

(45) Fang, G.; Amirfazli, A. *Langmuir* **2012,** *28*, 9421-9430.

(46) Oliver, J. F.; Huh, C.; Mason, S. G. *J. Colloid Interface Sci.* **1977,** *59*, 568-81.

(47) Berthier, J.; Loe-Mie, F.; Tran, V. M.; Schoumacker, S.; Mittler, F.; Marchand, G.; Sarrut, N. *J. Colloid Interface Sci.* **2009,** *338*, 296-303.

(48) Kalinin, Y. V.; Berejnov, V.; Thorne, R. E. *Langmuir* **2009,** *25*, 5391-5397.

(49) Sheng, X.; Zhang, J.; Jiang, L. *Langmuir* **2009,** *25*, 9903-9907.

(50) Gibbs, J. W. *"Scientific Papers"* **1906**, 326.

(51) Wang, J.; Chen, D. *Langmuir* **2008,** *24*, 10174-10180.

(52) Kurogi, K.; Yan, H.; Tsujii, K. *Colloids Surfaces, A* **2008,** *317*, 592-597.

(53) Ondarcuhu, T.; Piednoir, A. *Nano Lett.* **2005,** *5*, 1744-1750.

(54) Extrand, C. W.; Moon, S. I. *Langmuir* **2008,** *24*, 9470-9473.

(55) Cao, L.; Hu, H.-H.; Gao, D. *Langmuir* **2007,** *23*, 4310-4314.

(56) Tuteja, A.; Choi, W.; Ma, M.; Mabry, J. M.; Mazzella, S. A.; Rutledge, G. C.; McKinley, G. H.; Cohen, R. E. *Science* **2007,** *318*, 1618-1622.

(57) Ahuja, A.; Taylor, J. A.; Lifton, V.; Sidorenko, A. A.; Salamon, T. R.; Lobaton, E. J.; Kolodner, P.; Krupenkin, T. N. *Langmuir* **2008,** *24*, 9-14.

(58) Marmur, A. *Langmuir* **2008,** *24*, 7573-7579.

(59) Wang, J. D.; Liu, F. B.; Chen, H. S.; Chen, D. R. *Appl. Phys. Lett.* **2009,** *95*, 3.

(60) Youngblood, J. P.; McCarthy, T. J. *Macromolecules* **1999,** *32*, 6800-6806.

(61) Yoshimitsu, Z.; Nakajima, A.; Watanabe, T.; Hashimoto, K. *Langmuir* **2002,** *18*, 5818-5822.

(62) Dorrer, C.; Ruehe, J. *Langmuir* **2007,** *23*, 3179-3183.

(63) Extrand, C. W. *Langmuir* **2002,** *18*, 7991-7999.

(64) Extrand, C. W. *Langmuir* **2006,** *22*, 1711-1714.

(65) Decker, E. L.; Frank, B.; Suo, Y.; Garoff, S. *Colloids Surf., A* **1999,** *156*, 177-189.

(66) Meiron, T. S.; Marmur, A.; Saguy, I. S. *J. Colloid Interface Sci.* **2004,** *274*, 637-644.

(67) Li, W.; Amirfazli, A. *Adv. Colloid Interface Sci.* **2007,** *132*, 51-68.

(68) Antonini, C.; Carmona, F. J.; Pierce, E.; Marengo, M.; Amirfazli, A. *Langmuir* **2009,** *25*, 6143-6154.

(69) Bico, J.; Thiele, U.; Quere, D. *Colloids Surf., A* **2002,** *206*, 41-46.

(70) Dorrer, C.; Ruhe, J. *Langmuir* **2008,** *24*, 1959-1964.

(71) Li, W.; Amirfazli, A. *Soft Matter* **2008,** *4*, 462-466.

Appendix B

To compare and show how our results will also encompass findings of previous studies, FE curves illustrating wetting case A, case B and case C mentioned in the paper of Oliver et al. (Oliver, J. F.; Huh, C.; Mason, S. G. J. Colloid Interface Sci. 1977, 59, 568-81.) are discussed.

Figure B-1a shows the FE curves for a drop with increasing drop volume sitting on a single pillar (θ_Y=80 °, L_A=0.001m) with edge angle Φ = 60 °(< θ_Y = 80 °) which satisfies the condition of case A ($\Phi \leq \theta_Y$, see Section 2.2.1 in the main text). When the drop volume is small (FE curve 1), the minimum FE state is on the dotted line part (the drop FE states for drop at positions B), indicating that the drop three phase contact line (TPCL) is still away from the pillar's edge and thus similar to a drop spreading behavior on an ideally smooth surface showing an equilibrium CA (= θ_Y = 80 °) (see Figure B-1b). Note that the solid line part (the drop FE states at positions C) is not available for FE curve 1 because the criterion given by eq 2-8 is violated. If the drop volume increases to a critical value (FE curve 2), the minimum FE state will be at the reference position A (i.e. the pillar's edge), indicating that the most stable TPCL has reached the pillar's edge. Moreover, the minimum FE state will remain at the reference position A with further increase of drop volume (FE curve 3 to curve 8), indicating that the most stable drop TPCL will be pinned at the pillar's edge while the drop equilibrium CA approaches but never reaches θ_C (>=180 °). The result is consistent with the

drop spreading behavior of case A described by Oliver et al.[1] (see Section 2.2.1 in the main text)

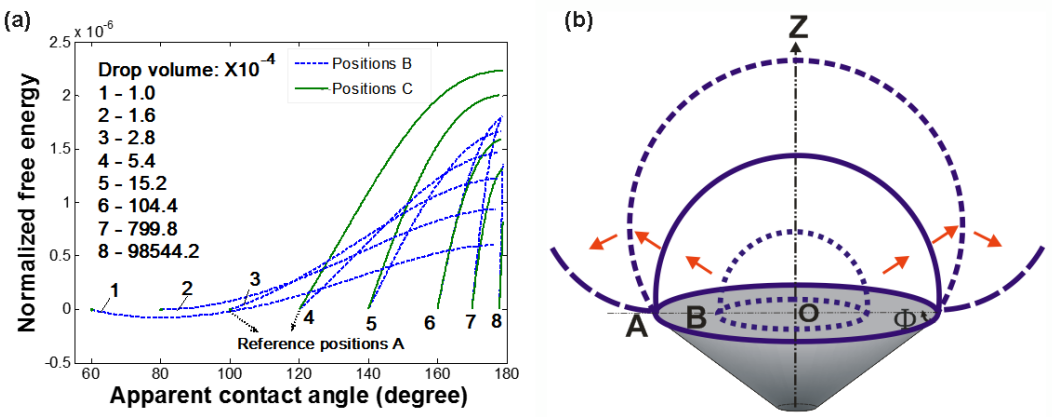

Figure B-1. (a) Comparison of variations of normalized FE with apparent CA for various drop volumes (θ_Y=80 °, L_A=0.001m, θ_A=60-160 °, Φ=60 °). (b) Schematic showing the drop spreading behavior in wetting case A.

Figure B-2a shows the FE curves for drop with increasing drop volume sitting on a single pillar (θ_Y=80 °, L_A=0.001m) with edge angle Φ = 120 ° which satisfies the condition of case B ($\Phi > \theta_Y$ & $\Phi > \theta_Y + 2\text{atan}(0.5\cot\theta_Y)$). Here, we do not repeat the statement for the FE curves 1 and 2 because they are similar to the cases in Figure B-1. As the TPCL reaches the pillar's edge, the minimum FE state will remain at the reference position A with further increase of drop volume (FE curve 3 to curve 5), indicating that the most stable drop TPCL will be pinned at the pillar's edge while the equilibrium CA approaches θ_C (= θ_Y + (180 ° - Φ) =140 °). After the drop equilibrium CA reaches θ_C (=140 °), the minimum FE state will move to the solid line part (FE state for drop at positions C) and the apparent CA energetically favorable will remain constant at θ_C (=140 °) with further

increase of drop volume; i.e., a drop collapse will take place and the TPCL will move steadily over the edge onto the sidewall. The result is consistent with the drop spreading behavior of case B described by Oliver et al.[1] (see Section 2.2.1 in the main text)

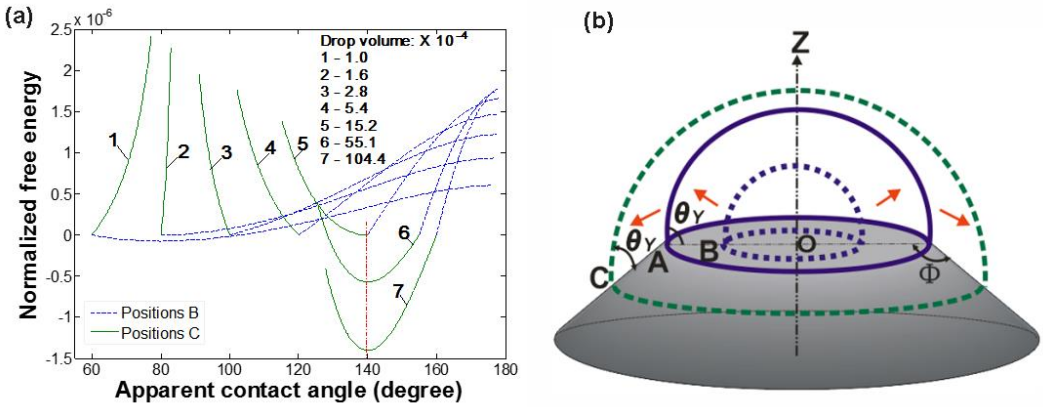

Figure B-2. (a) Comparison of variations of normalized FE with apparent CA for various drop volumes (θ_Y=80°, L_A=0.001m, θ_A=40-160°, Φ=120°). (b) Schematic showing the drop spreading behavior in wetting case B.

Figure B-3a shows the FE curves for drop with increasing drop volume sitting on a single pillar (θ_Y=80°, L_A=0.001m) with edge angle Φ = 85° which satisfies the condition of case C ($\theta_Y < \Phi < \theta_Y + 2\text{atan}(0.5\cot \theta_Y)$). As the TPCL reaches the pillar's edge, the minimum FE state will be staying at the reference position A with further increase of drop volume (FE curve 3 to curve 8), indicating that the most stable drop TPCL will be pinned at the pillar's edge while the apparent energetically favorable CA approaches θ_C (= θ_Y + (180° - Φ) =175°). It is noted that the FE curve for the solid line part becomes a convex shape after curve 7, indicating a FE barrier existing (see the enlargement). It also shows that

the increase of the drop volume will decrease the FE barrier. Thus, the drop may collapse, if the FE barrier is overcome with the help of external energy from extra sources such as mechanical vibration. After the equilibrium CA reaches θ_C (=175 °), there is no longer a minimum FE state existing, resulting in an immediate drop collapse. However, unlike case B, the TPCL cannot move steadily over the edge, since the pillar's edge will touch the drop cap and then split into two parts (one part is staying on top of the pillar while the other part is on the pillar sidewall), see Figure B-3b. The result is consistent with the drop spreading behavior of case C described by Oliver et al.[1] (see Section 2.2.1 in the main text)

In conclusion, results from our thermodynamic model are consistent with the former work done by Oliver et al.[1] Nevertheless, a full physical picture can be understood by the FE and FEB information obtained. This has expanded current understanding in Gibbs' in equality condition.

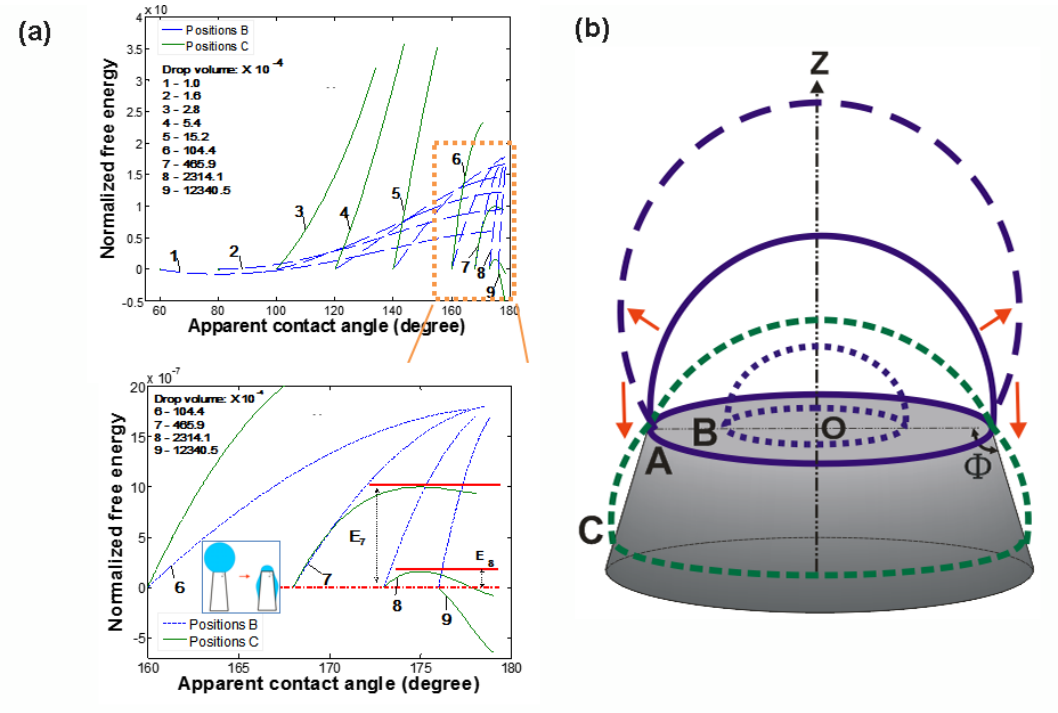

Figure B-3. (a) Comparison of variations of normalized FE with apparent CA for various drop volumes (θ_Y=80 °, L_A=0.001m, θ_A=40-160 °, Φ=85 °). The enlarged view of the box is also given. (b) Schematic showing the drop spreading behavior in wetting case C, and also drop splitting (dashed line).

Appendix C

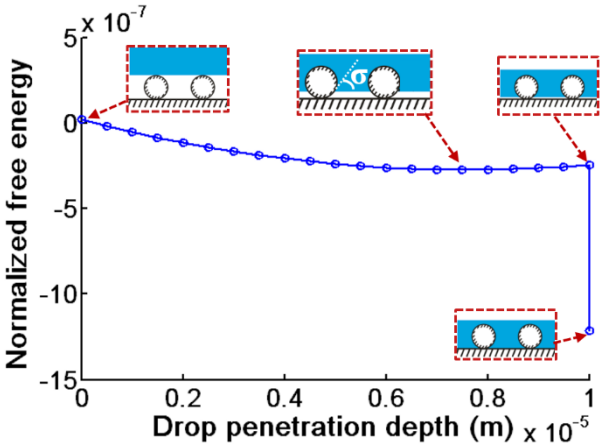

Figure C-1. Normalized FE curves as a function of the drop penetration depth for the microstructures of convex side wall (θ_Y = 60 °). The microscopic CA (σ) for the drop at metastable state is 60 °, which equals to the intrinsic CA θ_Y=60 °. Note that $a = b = 10\times10^{-6}$m, $2r = 10\times10^{-6}$m, drop volume = 9.7×10^{-9}m^3. Solid lines are to guide the eyes.

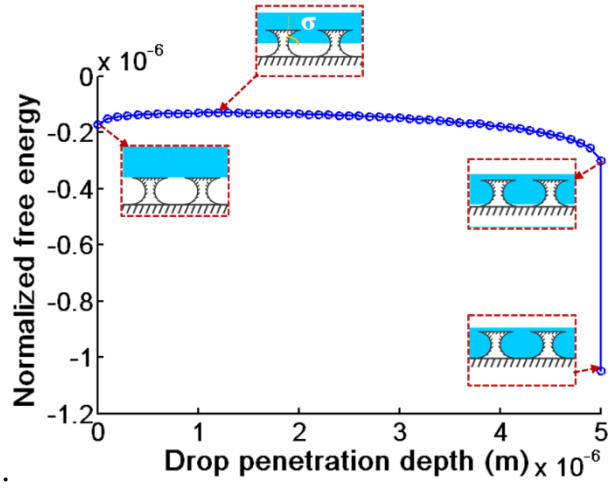

Figure C-2. Normalized FE curve as a function of the drop penetration depth for the microstructures of concave side wall (θ_Y = 60 °). The microscopic CA (σ) for the drop at maximum FE state is 60 °, which equals to the intrinsic CA θ_Y=60 °. Note that $a = b = 10\times10^{-6}$m, $2r = 5\times10^{-6}$m, drop volume = 9.7×10^{-9}m^3. Solid lines are to guide the eyes.

Appendix D

Table D-1. Freezing and melting points for different surfaces. SD denotes the Measurement standard deviation.

Surface type	T - Freezing (℃)	SD-Freezing	T - Melting (℃)	SD-Melting
Superhydrophilic	-10.8	2.1	0.0	0.0
Hydrophilic	-20.4	1.2	-0.1	0.1
Hydrophobic	-24.6	0.8	-0.1	0.1
SHS-Dip	-26.0	0.7	-0.1	0.1
SHS-Spray	-10.1	1.8	-0.1	0.1

Table D-2. The profile roughness parameters for aluminum sheet of different wettabilities. Note that SD denotes the standard deviation for measurements.

	Ra (micrometer)	SD-*Ra*	*Rq* (micrometer)	SD-*Rq*
Hydrophilic	0.48	0.10	0.89	0.19
Hydrophobic	0.45	0.15	0.87	0.34
SHS-Dip	4.59	0.36	5.49	0.44
SHS-Spray	5.08	0.19	6.15	0.28

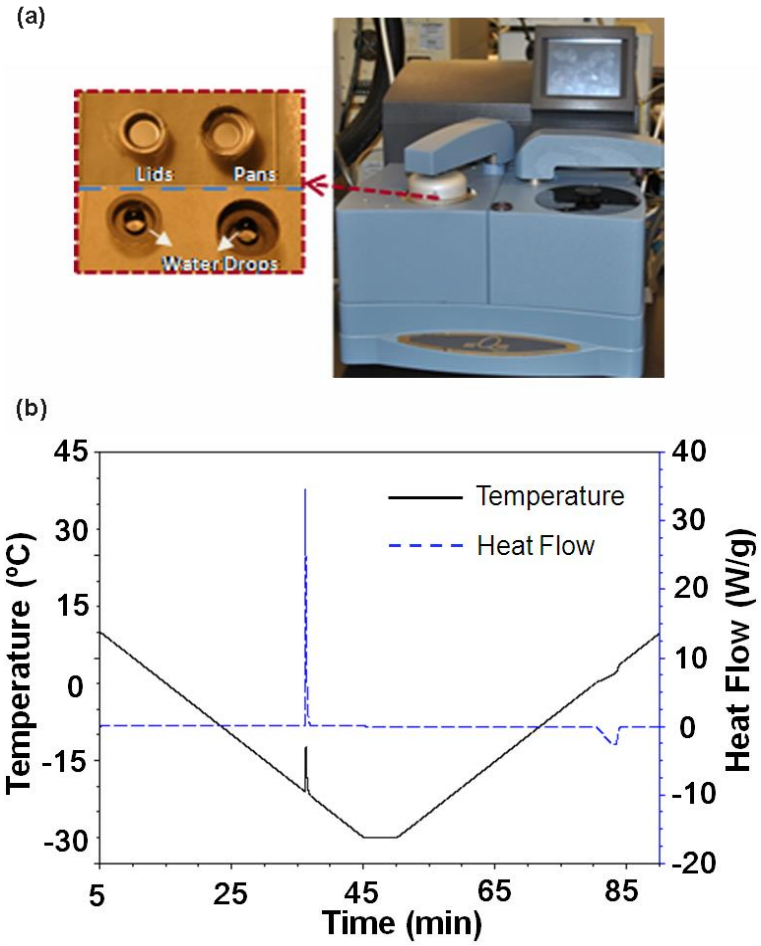

Figure D-1. Freezing and melting points measurement in DSC. a, Smooth and rough sample vessels and the DSC Q1000 instrument. b, Typical DSC heating and cooling curves (solid line for temperature curve and dashed line for heat flow curve) of 6 μl DI water drop in an untreated sample vessel. Both endotherms and exotherms are shown. Temperature ramp is 1 ℃/min. An exothermic peak can be observed with an initial temperature of –20.7 ℃, which is taken as the freezing point of water drop in the tested vessel. Similarly, an endothermic "dip" can be observed with an initial temperature –0.08 ℃, indicating the melting point of the water drop.

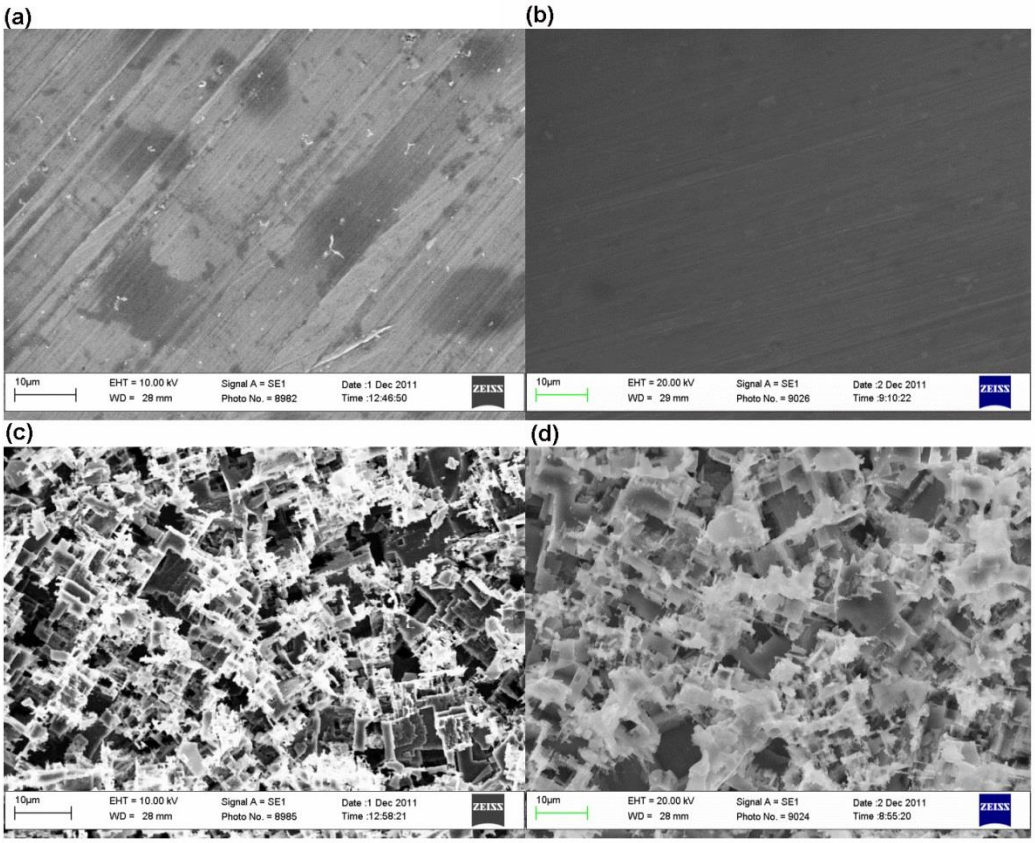

Figure D-2. SEM images for DSC sample vessels. a, Hydrophilic surface. b, Hydrophobic surface. c, Superhydrophilic surface. d, SHS-Dip surface. Due to the electric insulation of the Teflon film, the SEM images for the hydrophobic and SHS-Dip surfaces appear darker compared to the hydrophilic and superhydrophilic surfaces, respectively.

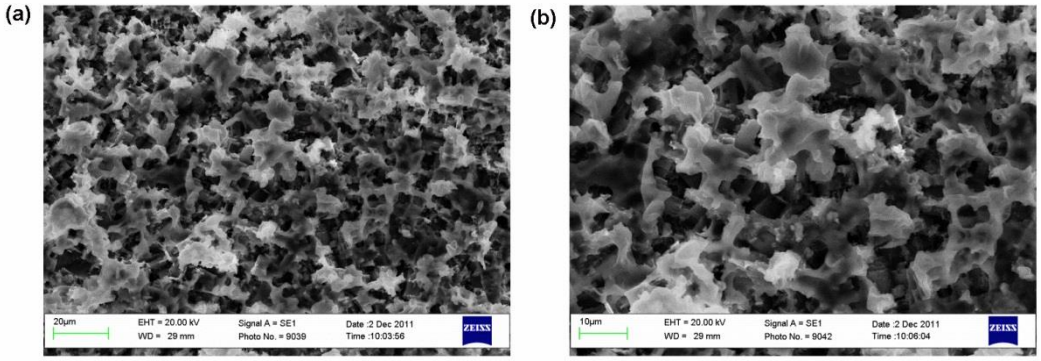

Figure D-3. SEM images for DSC sample vessels of SHS-Spray.

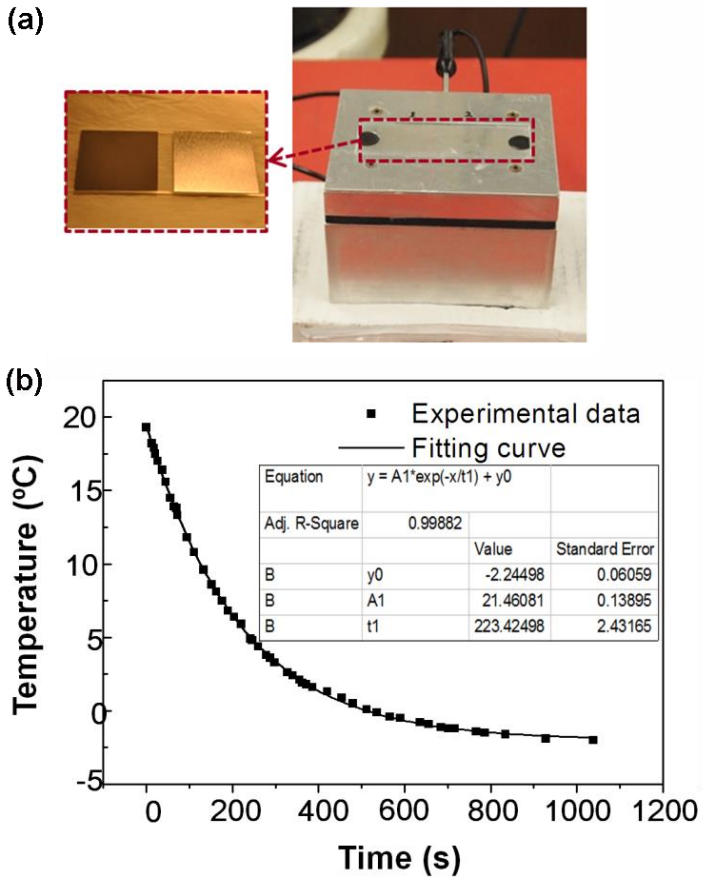

Figure D-4. Drop freezing tests on thermoelectric cooler. a, Smooth and rough sample sheets and the thermoelectric cooler. b, Temperature change curve on the thermoelectric cooler.